Mechanisms of DNA double strand break-mediated neurotoxicity in neurodegenerative disease

by

Gwyneth M. Welch
BSc., University of New Hampshire, 2016

Submitted to the Department of Brain and Cognitive Sciences
in Partial Fulfillment of the Requirements for the Degree of
Doctor of Philosophy

at the

MASSACHUSETTS INSTITUTE OF TECHNOLOGY

September 2022

Author .....
Department of Brain and Cognitive Sciences
July 22, 2022

Certified by.....
Li-Huei Tsai, Ph.D.
Professor and Director — Picower Institute for Learning and Memory
Thesis Supervisor

Accepted by .....
Mark Harnett, Ph.D.
Graduate Officer, Department of Brain and Cognitive Sciences

Mechanisms of DNA double strand break-mediated neurotoxicity in neurodegenerative disease

by Gwyneth M. Welch

Submitted to the Department of Brain and Cognitive Sciences on July 22, 2022, in Partial Fulfillment of the Requirements for the Degree of Doctor of Philosophy in Neuroscience

Abstract

Neurons are highly susceptible to DNA damage accumulation due to their large energy requirements, elevated transcriptional activity and long lifespan. DNA double strand breaks (DSBs) are also linked to neurodegeneration and senescence. However, it is not clear how DSB-bearing neurons influence processes of neuroinflammation and neurodegeneration. Here, we characterize DSB-bearing neurons from the CK-p25 mouse model of neurodegeneration using single-nucleus, bulk, and spatial transcriptomic techniques. DSB-bearing neurons enter a late-stage DNA damage response marked by NFκB-activated senescent and antiviral immune pathways. In humans, Alzheimer's disease pathology is significantly associated with immune activation in excitatory neurons. Spatial transcriptomics reveal that regions of CK-p25 brain tissue dense with DSB-bearing neurons harbor signatures of inflammatory microglia, which is ameliorated by NFκB knock down in neurons. Inhibition of NFκB in DSB-bearing neurons also reduces microglia activation in organotypic mouse brain slice culture. In conclusion, DSBs activate immune pathways in neurons, which in turn adopt a senescence-associated secretory phenotype to elicit microglia activation. These findings highlight a novel role for neurons in the mechanism of disease-associated neuroinflammation.

Thesis Supervisor: Li-Huei Tsai, Ph.D.
Title: Professor and Director — Picower Institute for Learning and Memory

Acknowledgments

Thank you Li-Huei for your mentorship, advocacy, creativity, and inspiration. I learned so much from you over these past 6 years, and I could not have imagined a better lab in which to earn my PhD.

Thank you to my post-doc mentors, especially Jemmie, PaoPao, and Mat, for their knowledge and guidance in both science and life.

Thank you to my committee members Gloria, Myriam, and Bruce, for their scientific guidance and advocacy.

Infinite gratitude to Ying and Erica, and fellow grad students Ryan, Mitch, Leyla and Djuna, for their support, comradery, and friendship.

Conor, I am forever grateful to you for your unconditional love and endless encouragement. Thank you to Kate, Eli, and Mariana for their humor and hearts of gold.

Ultimate blessings to my wonderful Mom and Dad, and my fantastic siblings, Lauryn, Will, and Storm.

Contributions

Gwyneth Welch designed and performed all experiments unless otherwise indicated.

Li-Huei Tsai advised on the design, performance, and interpretation of all experiments.

Jemmie Cheng sorted Stage 1 and Stage 2 neurons for bulk RNA-seq.

Qiao Su performed transcript alignment, quantification, and differential analysis for Stage 1 and Stage 2 bulk RNA-seq.

Carles Boix aligned and analyzed the Stage 1 & 2 snRNA-seq dataset.

José Davila-Velderrain assessed Stage 2 signature enrichment in snRNA-seq data from Mathys et al., 2019. He also performed transcript alignment, quantification, and differential analysis for bulk RNA-seq from postmortem human brain.

Matheus Victor performed p65 and γH2AX immunoflourescent microscopy and analysis from Alzheimer's disease cortical tissue. He also advised on the design of the mir30-shRNA construct.

Eloi Schmauch aligned and analyzed the Visium spatial transcriptomics dataset.

Lorenzo Bozzelli generated the acute slice cultures from *Cx3cr1*-gfp mice.

Noelle Leary quantified amyloid-beta and phospho-tau intensity in p65kd vs. scramble CK-p25 mice.

Audrey Lee quantified microglia size and number in p65kd vs. scramble CK-p25 mice.

All sequencing was performed with the assistance of the MIT BioMicro Center. All sorting was performed at the Swanson Biotechnology Center Flow Cytometry Facility. Visium imaging was performed with the assistance of the MIT Hope Babette Tang (1983) Histology Core Facility and J. the MIT Microscopy Core Facility. AAV generation was performed by the Janelia Viral Tools Facility.

Table of Contents

List of Figures

List of Tables

Chapter 1

Introduction

Post-mitotic neurons are the basic cellular unit of the nervous system. Their function controls primary aspects of human physiology, including movement, breathing, and heart rate, as well as higher order processes such as memory and attentional control. However, as a largely non-renewable resource, neurons must perform these essential tasks while also maintaining their cellular and genomic integrity over many decades of life. To survive the inexorable passage of time, neurons are equipped with accurate and efficient DNA damage response (DDR) pathways. Defective DDR pathways can result in toxic genomic rearrangements, transcriptional dysregulation, and the accumulation of unrepaired lesions(1–5). These insults ultimately push cellular fate towards apoptosis, senescence, or uncontrolled cell division, all of which are hallmarks of age-associated disease(1–5). We can appreciate the value of neuron viability in particular through the devastating effects of neurodegenerative diseases, which strip individuals of their memories, motor control, and autonomy. As of 2017, neurologic diseases are the third leading cause of death in the United States and the fifth leading cause of death world-wide(6,7).

A well-established link exists between DNA damage and neurodegenerative diseases. In many cases, DNA damage seems to be one of the earliest indicators of neuropathology, suggesting it may be an initiating lesion of toxicity(5,8–10). Recently, numerous findings have helped clarify the mechanisms by which DNA damage may mediate neuronal dysfunction. Broadly, these are lessons learned through both DNA damage repair disorders and models of age-associated neurodegenerative diseases. Additionally, through the advancement of sequencing techniques to map DNA lesions, rearrangements, and mutations,

we are just beginning to appreciate the significance of a lesion's genomic location in relation to its effect on neuronal activity, and ultimately, degeneration(11–17). Finally, while both neuroinflammation and DNA damage are considered hallmarks and mediators of neurodegeneration, the mechanistic relationship between the two has yet to be fully realized. To this end, concepts from senescence cell biology are helping us inform how one might feed into the other(18–22). In this introduction, we will cover the recent advances made in each of these subgenres of disease research, and how they enhance our understanding of neuronal function and degeneration.

1.1 The DNA Damage Response (DDR)

Our genome continually incurs damage via exogenous agents and endogenous metabolic byproducts. In response to the constant onslaught of genomic lesions, mammalian cells have developed a myriad of DNA damage response (DDR) pathways, each specializing in the detection and correction of a different type of lesion. Although each pathway recruits different proteins and repair enzymes, the basic DDR format remains the same. Lesions are first detected, then they are processed and/or excised by a nuclease. Lastly, a polymerase synthesizes new DNA to replace the missing nucleotides, and a ligase seals the resulting nick together. The following section briefly summarizes DNA lesions and their corresponding DDR pathway.

1.1.1 Single Strand Breaks (SSBs)

While many different types of genomic injuries can occur, the majority ultimately manifest in the form of single-strand breaks (SSBs). This is largely by virtue of reactive oxygen species (ROS), which attack DNA to form oxidized bases and abasic sites(2,3,23). ROS-mediated DNA damage is greatest in the nervous system(24), likely because neurons exhibit substantial mitochondrial respiration, consuming approximately 20% of the body's available oxygen(25). ROS can generate SSBs directly through attacking the DNA backbone or indirectly through the generation of other DNA modifications whose

repair require transient break formation. One of the most abundant ROS-mediated DNA modifications is 8-oxo-7,8-dihydroguanine (8oxoG), a non-bulky lesion whose presence can dysregulate gene transcription and whose erroneous repair results in mutagenesis, a major contributor to aging and disease.

Non-bulky base modifications such as 8oxoG are resolved through base excision repair (BER), wherein a base-specific glycosylase detects and removes the damaged base, and the backbone is removed by apurinic/apyrimidinic endonuclease 1 (APE1) to generate an intermediate SSB. From here, the SSB can be resolved either through short-patch SSB repair (sp-SSBR) or long-patch SSBR (lp-SSBR). In short patch SSBR, polymerase β (POLβ) fills in the missing nucleotide and ligase III (LIG3) seals the nick. The alternative lp-SSBR replaces larger stretches of DNA (2-13 nucleotides), utilizing flap endonuclease 1 (FEN1), proliferating cell nuclear antigen (PCNA), and polymerase δ/ε (POL δ/ε) to open and replace the broken DNA strand. Ligase I (LIGI) then seals the nick.

In contrast to smaller base lesions, helix-distorting bulky lesions (which are most commonly caused by UV exposure) are detected by their steric distortion rather than their specific chemical structure. For example, bulky lesions are detected during transcription when their presence stalls RNA polymerase II, which with the help of proteins CSA and CSB (also known as ERCC6 and ERCC8, respectively) initiates transcription-coupled nucleotide excision repair (TC-NER). In non-transcribed or inactive regions of the genome, bulky lesions are detected by the XPC-RAD23B-CEN2 complex, which initiates global genomic NER (GG-NER). Beyond the mechanism of their initial detection, TC-NER and GG-NER share the same pathway. The transcription factor complex TFIIH is recruited to the lesion and opens up the DNA, further recruiting other NER repair factors to form a pre-incision complex. The damaged nucleotide is removed by ERCC1-XPF and XPG, generating an SSB. New DNA is synthesized by POLβ/δ/ε, then sealed by LIG1 or LIG3.

Apart from ROS, direct SSBs can also be generated by aborted topoisomerase I (TOP1) activity,

which occurs when TOP1-initated breaks meant to relax supercoiled DNA are not resolved. These persisting breaks are termed TOP1 DNA cleavage complexes (Top1cc)(26). Top1cc accumulation pose a significant threat to the nervous system. First, oxidative DNA damage has been shown to impede Top1cc resolution(27), making neurons particularly sensitized to aborted TOP1 activity. Second, individuals with defunct Tyrosyl-DNA Phosphodiesterase 1 (TDP1), the SSB repair enzyme responsible for resolving Top1ccs, develop spinocerebellar ataxia with axonal neuropathy (SCAN1). This genetic disease is primarily defined by nervous system deficits such as ataxia, neuropathy, and cerebellar atrophy(26,28).

1.1.2 Double Strand Breaks (DSBs)

While SSBs are the more common form of DNA damage, double strand breaks (DSBs) have the higher potential for toxicity. Indeed, it is popularly cited that just one DSB can induce cell cycle arrest and subsequent apoptosis(29). However, despite their toxicity, DSBs have also been shown to play important roles in cell physiology. For example, DSBs are required for T-cell receptor and antibody diversity, chromosomal recombination during meiosis, and in the case of neurons, assist in the expression of immediate early genes (Figure 1-1)(30–32).

While replication is likely the primary cause of DSBs in cycling cells, postmitotic neurons presumably incur the majority of their DSBs through transcriptional activity. SSBs may form DSBs through their collision with the transcriptional machinery and replication forks, or through their close proximity to another SSB. DSBs are also directly generated by transcription(33), whereby topoisomerase II (TOP2) induces transient DSBs to relieve torsional stress and facilitate gene expression. These Top2 cleavage complexes (Top2ccs) are usually resolved immediately by Tyrosyl-DNA Phosphodiesterase 2 (TDP2). Similar to TDP1, mutations in TDP2 result in a rare neurological disease termed spinocerebellar ataxia autosomal recessive 23 (SCAR23), further underscoring the potential toxicity of topoisomerase-induced DNA damage in the nervous system(34–36).

There are two methods of DSB repair: non-homologous end joining (NHEJ) and homologous recombination (HR). HR is considered an error-free method of DSB repair by which resected DNA strands utilize their sister chromatid as a template for DNA synthesis. First, the MRN (MRE11, RAD50, NBS1) complex binds to either side of the DSB to facilitate end resection by nucleases and helicases, including C-terminal binding protein-interacting protein (CtIP), Exonuclease 1 (EXO1), DNA replication helicase/nuclease 2 (DNA2), Werner syndrome helicase (WRN), and Bloom syndrome helicase (BLM). The resulting ssDNAs are coated by replication protein A (RPA) and RAD51, forming nucleoprotein filaments that invade the sister chromatid to look for sequence homologies. New DNA is then synthesized by a polymerase and ligated with LIG1 or LIG3.

Because HR requires sister chromatids, this pathway can only occur in cycling cells during or following S phase. In contrast, NHEJ operates in all phases of the cell cycle, and thus is the only DSB repair pathway available to post-mitotic cells. In canonical NHEJ, DSBs are first bound on either end by KU70/80 and DNA-dependent protein kinase (DNA-PK), then directly ligated back together with Ligase IV (LIG4), X-Ray Repair Cross Complementing 4 (XRCC4), and XRCC4-like factor (XLF). In an alternate form of NHEJ (alt-NHEJ), the broken strands are resected with the same nucleases and helicases used for HR (CtIP, EXO1, DNA2, BLM, WRN), resulting in single-strand overhangs at either side of the break site. These overhangs then anneal at microhomologies, which are small stretches of complementary DNA, usually 5-20 bp long. Polymerase θ (POLθ) synthesizes new DNA which is then ligated by LIG3. Yet another alternative DSB repair pathway, termed single strand annealing (SSA), searches for even larger homologies (>25bp). RAD52 mediates the annealing of resected DNA at these larger homologous sequences, and the resulting DNA flaps are excised by ERCC1-XPF. Both alt-NHEJ and SSA are inherently error-prone, as deletions of DNA and translocations must occur to facilitate strand annealing.

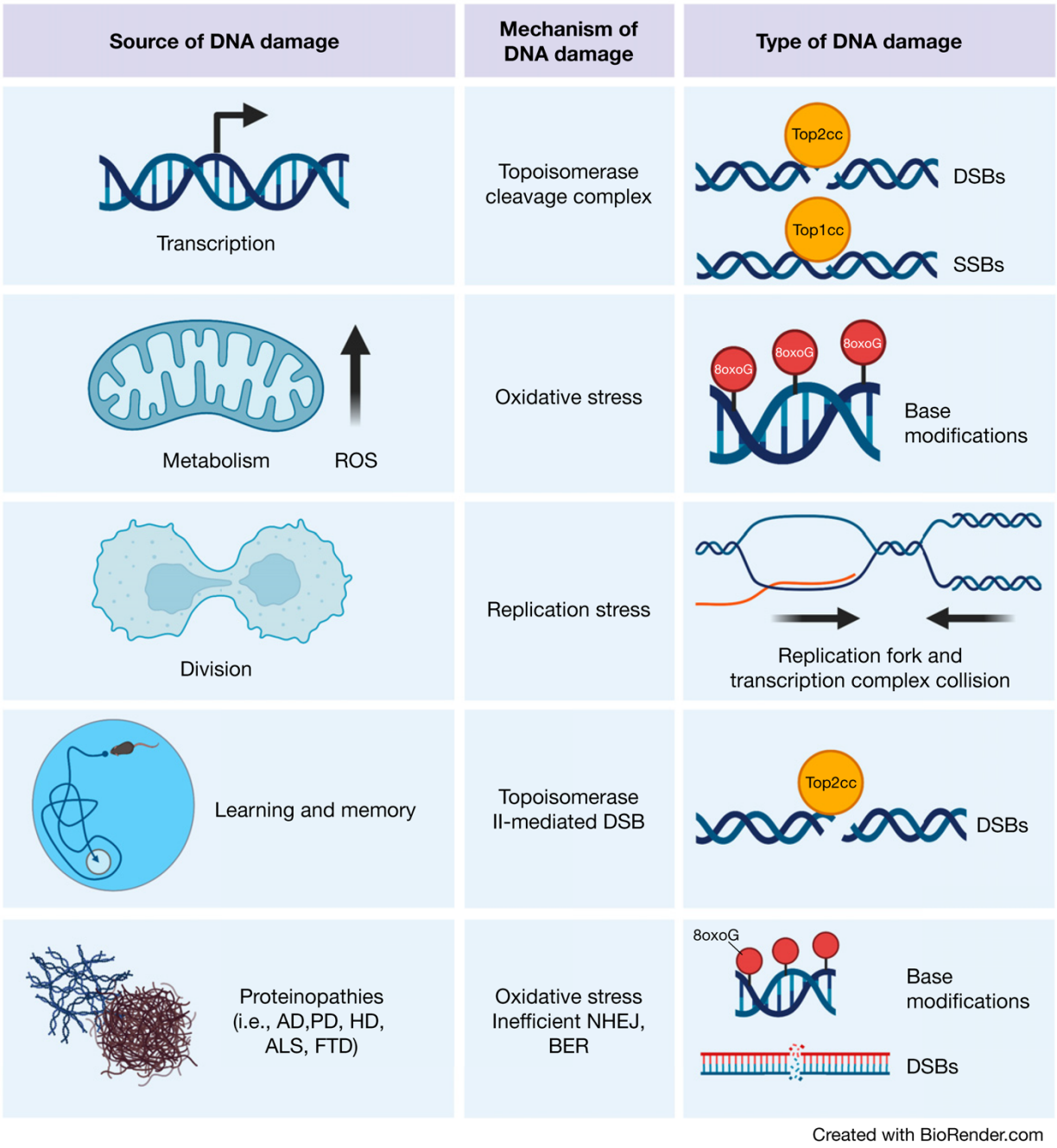

Figure 1-1 Sources of DNA damage in the brain. Transcriptional activities can result in topoisomerase cleavage complexes, which lead to the induction of SSBs or DSBs depending upon the topoisomerase in question. Additionally, metabolic activity by mitochondria generate ROS, which can scar DNA bases with oxidative modifications. Although less common in the adult brain, cell division is also a source of DNA damage. Proliferation increases the chance of replication fork and transcription complex collision, thereby inducing DSBs. In the developing brain, this is a particular risk for NPCs, which harbor increased translocations in long genes (where these collisions are most likely to occur) important for neuronal function. Cognitively demanding tasks recruit specific neuronal ensembles whose plasticity is highly dependent upon immediate early gene transcription. Therefore, neurons generate topoisomerase II-mediated DSBs in response to learning and memory. Finally, the proteins responsible for various neurodegenerative diseases have also been found to play roles in DNA damage detection and repair.

1.1.3 SSB and DSB sensing

Following break induction, chromatin is rapidly modified by DNA damage sensors to facilitate the recruitment of DNA repair proteins. Poly(ADP-ribose) polymerase 1 (PARP1) and Ataxia telangectasia mutated (ATM) are two major sensors of SSBs and DSBs. PARP1 senses both SSBs and DSBs, rapidly generating poly(ADP-ribose) (PAR) chain scaffolds (PARylation) on itself and other target proteins to recruit DNA repair proteins and relax chromatin at break sites. PARylation by PARP1 recruits X-Ray Repair Cross Complementing 1 (XRCC1) which is a crucial stabilizer for end-processing enzymes POLβ and LIG3. PARylation also facilitates MRN recruitment at DSBs. Similarly, following its activation by the MRN complex at DSB sites, the protein kinase ATM phosphorylates numerous downstream substrates such as histone variant H2A.X, checkpoint kinase 2 (CHK2), and p53 to initiate DSB repair, cell cycle arrest, and apoptosis, respectively. In particular, phosphorylation of H2A.X (γH2AX) by ATM is a critical post-translational modification, flanking DSB sites more than 500 kb upstream and downstream to form γH2AX foci, which function as docking sites for chromatin remodelers and DNA repair proteins.

1.2 Neurotoxicity associated with DNA damage

The nervous system is particularly sensitive to loss-of-function mutations in DNA repair proteins. The explanation for this sensitivity may lie in the hallmarks of neuronal identity. That is, neurons perform transcriptionally and energetically demanding cellular functions, are post-mitotic, and long-lived. The consequence of these features are elevated ROS byproducts, exclusion of error-free HR repair, age-associated decline in DNA repair enzyme efficiency, and an overall increased chance of somatic mutation. This is not to say that other cell types in the nervous system (i.e. astrocytes, oligodendrocytes, and microglia) are not susceptible to DNA damage. Indeed, DNA damage in glia plays demonstrable roles in neurodegeneration, as we will discuss later. However, compared to neurons, glial cells are replaceable,

have lower energy requirements, and in some cases, are able to re-enter the cell cycle, thus facilitating DNA repair. Combined, these features reduce the burden of DNA damage toxicity in glia. Therefore, in the following sections, we take a neuro-centric approach to interpreting the effects of DNA damage on the nervous system.

1.2.1 Functional roles for DNA damage in neuronal activity and development could lead to dysfunction later in life

Another reason why neurons are so susceptible to genomic toxicity stems from the fact that DNA breaks seem to serve a functional role in neuronal activity. Stimulating primary neurons with bicuculline or subjecting mice to fear learning results in the induction of DSBs at the promoters of immediate-early genes (Figure 1-1)(31,37). Even simply introducing a mouse to a new environment is quickly followed by the induction of DSBs in neurons(32,38). These activity-induced DSBs are hypothesized to facilitate the expression of immediate early genes through the rapid resolution of topological constraints at their transcription start sites. Previously, to identify the induction of DSBs at immediate-early gene promoters, researchers have utilized γH2AX chromatin immunoprecipitation (ChIP) sequencing(31,37), which generates broad peaks associated with DSB detection. More recently developed technologies may help improve the resolution of activity-associated break induction in neurons(39). For example, a DSB-mapping technique known as END-seq was recently used to identify strand breaks in human induced pluripotent stem cell (iPSC)-derived neurons, resulting in the finding that enhancers are hotspots for SSBs(11,40). Newer break-mapping techniques include single nucleotide precision, Break Labeling *In Situ* and Sequencing (BLISS) for DSBs(41) and single-strand break mapping at nucleotide genome level (SSiNGLe) for both SSBs and DSBs(42). However, the utility of these techniques has yet to be evaluated, as currently neither has been used to analyze the location of DNA breaks in neurons in physiological or pathological conditions.

Crucially, while DNA breaks may serve a physiological function in learning and memory, their

recurrence in neuron regulatory sequences make these regions extremely vulnerable to mutation and translocation. One can imagine that over time, erroneous DSB repair could lead to mutations that result in transcriptomic dysfunction, which could further manifest at the cellular level as impaired synaptic signaling. In line with this hypothesis, DNA repair mapping reveal that post mitotic neurons do indeed accumulate breaks in regulatory elements associated with neuronal function (Figure 1-2)(11,12).

In addition to postmitotic activity, it is clear that somatic mutations induced by erroneous DNA damage repair or transposable elements are a common feature of neural development, giving rise to neuron diversity through genomic mosaicism(30,43,44). While most mutations are likely to be neutral, work has shown that some may underly neurodevelopmental and neurodegenerative disease. For example, work mapping translocations in iPSC-derived neural precursor cells (NPCs) under replicative stress reveal that DSB hotspots reside in long genes that are important for neuronal function and are risk factors for autism spectrum disorder and schizophrenia(13,45,46). This mapping was accomplished through a technique known as linear amplification-mediated high-throughput, genome-wide, translocation sequencing (LAM-HTGTS). Using this technique, endogenous DSBs are identified based on their translocation to a "bait" DSB located at a specific region in the genome. Furthermore, a study performing whole exome sequencing of hippocampal tissue from individuals with Alzheimer's disease (AD) revealed that somatic single nucleotide variations (SNVs) increase with age and are enriched in genes that regulate tau phosphorylation(47). Accumulation of SNVs at neurodegeneration risk genes could potentially increase risk of disease development.

1.2.2 DNA repair syndromes as proxies for aging and neurodegenerative disease

Some of the most long-standing evidence for the role of DNA damage in aging and neurodegeneration stems from inheritable DNA damage disorders, which frequently present with neurologic abnormalities.

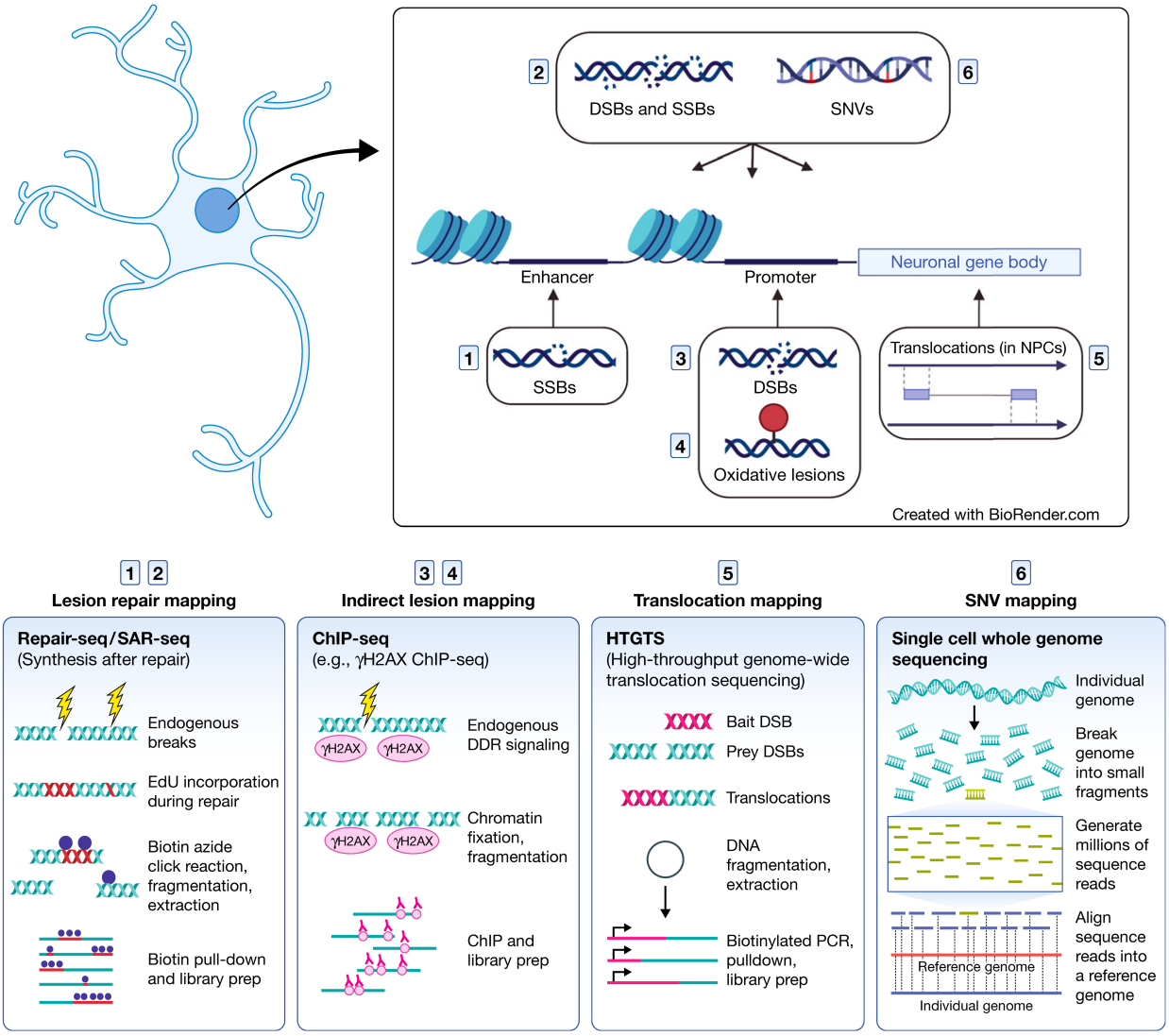

Figure 1-2 DNA lesions and mutations identified in neural genes and the techniques used to map them. While all cell types incur DNA damage and mutations, neurons in particular are susceptible due to activity-induced transcription. Immediate-early genes and other neuronal genes that enable synaptic function are highly transcribed. Accordingly, they accumulate DNA lesions and mutations in their gene body (Wei et al., 2016) and regulatory regions (Wu et al., 2021; Reid et al., 2021; Lodato et al., 2015).The induction of DSBs in the promoters of immediate-early genes facilitates gene expression (Madabhushi et al., 2015). Over time, these insults may impair neural function (Lu et al., 2004; Lodato et al., 2018; Pao et al., 2020).

With the exception of AOA5, which seems to have manifested exclusively in adults so far(48,49), the majority of DNA damage disorders typically present in early childhood. Why then would these disorders support the hypothesis that DNA damage plays critical roles in aging and neurodegeneration? First, as discussed in the previous section, we must acknowledge the pivotal role of DNA damage repair in neurodevelopment, a period in which the rapid proliferation of NPCs results in profound transcriptional and replication-associated DNA damage. Deficient DNA damage repair in these vulnerable NPCs results in developmental abnormalities such as microcephaly, which is a feature of many DNA damage disorders. However, many DNA damage disorders are also defined by age-associated pathologies such as progressive brain atrophy and peripheral neuropathy. In these cases it is likely that post-mitotic neurons are bearing the brunt of the DNA repair deficit. Thus, whether the resulting pathologies of a DNA repair deficit are developmental or age-associated likely depends on both the brain cell type composition at the time and the selective vulnerabilities of different neuronal subtypes to different repair deficits. Finally, the pathogenic load of a loss-of-function mutation accelerates the development of age-associated pathology, which may account for a DNA damage disorder presenting in childhood rather than later in life. In contrast, an individual devoid of DNA repair mutations must experience the progressive stress of aging (i.e. damage accumulation, oxidative stress, declining DNA repair enzyme efficiency) in order to recapitulate the pathogenic load of a DNA damage disorder. In the following subsections, we highlight two recently developed models of DNA damage disorders (one driven by mutant XRCC1, and the other by mutant ATM, and APTX) that have clarified mechanisms of DNA damage-mediated neuronal dysfunction.

1.2.3 Neurological diseases caused by SSBR mutations

To date, loss-of-function mutations in SSBR proteins have manifested exclusively as neurodegenerative syndromes. Ataxia with Oculomotor Apraxia types 1 and 4 (AOA1, AOA4) are caused by mutations in

DNA end-processing enzymes Aprataxin (APTX) and Polynucleotide Kinase 3'-Phosphatase (PNKP) respectively. As their names denote, both are progressive neurodegenerative diseases typified by cerebellar atrophy, ataxia, and oculomotor apraxia. SCAN1, caused by defective TDP1, is a similar neurodegenerative syndrome additionally characterized by peripheral neuropathy(26,28). More recently, mutations have been identified in XRCC1(48,49), the protein that complexes with and stabilizes all of these end-processing enzymes. Defective XRCC1 manifests in individuals as Ataxia with Oculomotor apraxia Type 5 (AOA5), another slow-progressing neurodegenerative disease.

If SSBs are left unrepaired in cycling cells, they can form DSBs upon collision with DNA replication complexes(50). Cycling cells with defective SSBR can access error-free HR during cell division to repair the resulting DSBs. However, post-mitotic neurons are not equipped with this alternate method of repair. This may explain why diseases of SSBR are exclusive to the nervous system; neurons are not able to mitigate SSB accumulation without the presence of a functioning SSBR. To this point, recent investigations into how mutant XRCC1 confers neuropathy have helped clarify the mechanisms by which defective SSBR could be neurotoxic. First, the study of patient fibroblasts from an individual with AOA5 revealed that in the absence of XRCC1, PARP1 becomes hyperactive, producing excessive amounts of poly(ADP-ribose)(48). Unchecked PARP1 activity can induce cell death by progressive NAD+/ATP depletion and Parthanatos, a cell death signaling pathway triggered by excessive poly(ADP-ribose)(51). PARP1 hyperactivity was further demonstrated through conditional deletion of XRCC1 in the mouse brain, which resulted in progressive cerebellar degeneration, ataxia, seizure-like activity, and dysregulated presynaptic calcium signaling in the hippocampus(48,52).

The mechanisms by which PARP1 hyperactivity could mediate neurotoxicity and dysregulated presynaptic calcium signaling have been explored in an additional pair of recent publications. First, in the absence of XRCC1, PARP1 was found "trapped" at break intermediates produced during BER, thus

impeding access of repair factors POLβ and LIG3(53). This indicates XRCC1 is a crucial regulator of PARP1 activity. Second, PARP1 hyperactivity in XRCC1-deficient cells was shown to suppress transcription through the recruitment of ubiquitin protease USP3, leading to excessive deubiquitination of histone substrates(54). Suppressed transcription may account for the dysregulated calcium signaling observed in neurons from XRCC1$^{Nes\text{-}Cre}$ mice, specifically through the suppression of genes that regulate calcium homeostasis. To this point, a separate publication revealed that iPSC-derived neurons accumulate SSBs at enhancers regulating neuronal activity(11). These SSB hotspots were identified through genome-wide mapping of DNA damage repair, dubbed SAR-seq (Synthesis After Repair), whereby EdU incorporation into break sites serves as a molecular landmark for break repair, and END-seq(11). SSB accumulation at enhancers regulating neuronal activity provides a tempting mechanistic explanation for the neurodegenerative hallmarks of SSBR syndromes.

In contrast to mutations in the SSBR pathways, mutations that dysregulate the NER pathway are additionally characterized by symptoms occurring outside of the nervous system. For example, the hallmark feature of Xeroderma Pigmentosum, caused by XP gene mutations, is skin peeling and crusting due to the skin cells' inability to repair bulky DNA modifications caused by UV exposure. Only about 20-30% of XP individuals develop progressive neurodegeneration(55). Furthermore, individuals with Cockayne Syndrome (CS), who are diagnosed based on delayed development, light sensitivity, and progeria, or Trichothiodystrophy (TTD), whose hallmark feature is brittle hair, can present with neurodevelopmental defects such as microcephaly, dysmyelination, and intellectual disability(56). Notably, while postmitotic neurons are able to repair bulky DNA modifications in both the template and non-template strand of transcribed genes, global NER is naturally attenuated in non-transcribed regions of the genome(55,57). Combined with the added stressor of NER mutations, this may account for the neurodegenerative phenotypes observed in XP, CS, and TTD.

1.2.4 Neurological diseases caused by DSBR mutations

One of the most well-known DDR syndromes is Ataxia Telangectasia (AT), which is caused by mutations in ATM kinase. Individuals with AT exhibit profound immune-deficiency and increased cancer susceptibility as well as progressive cerebellar atrophy, which results in ataxia by early childhood(58). Mutations in the MRN complex also produce syndromes with similar clinical phenotypes. Specifically, defective MRE11 causes AT-like disorder, which results in cerebellar atrophy, and defective NBS1 causes Nijmegen Breakage Syndrome, which results in microcephaly(3,4).

While murine knockout of ATM recapitulates the immune deficits observed in AT patients, these mutant mice seem to exhibit only mild ataxia and cerebellar atrophy(59,60). This has been a major limiting factor towards teasing out the molecular mechanisms of AT-related neurodegeneration. Nevertheless, studies utilizing ATM knockout mice have still revealed important roles for ATM in neuron health. First, abnormalities in lysosomal storage have been observed in Purkinje cells of ATM knockout mice, suggesting a pre-degenerative increase in cellular stress(61). Additionally, enriched Top1ccs are also observed in the cerebellum, similar to what is observed in TDP1 knockout mice, suggesting ATM also plays a role in topoisomerase-I mediated break sensing and repair(62,63). Finally, glial ATM seems to play crucial roles in neuronal health as well. Specifically, cerebellar cultures grown from ATM knockout mice exhibit disrupted network synchrony, which is rescued by culture with wild-type astrocytes(64).

Notably, the development of a new mouse model of AT harboring both ATM nonsense mutation and APTX knockout was found to better recapitulate the neurologic deficits observed in AT(65). While progressive cerebellar atrophy and ataxia were not observed in mice with individual mutations in either ATM or APTX, the combination of both mutations lowered the threshold for neuronal genomic instability, resulting in neurological deficits(65). This indicates that at least for murine models of AT, the ATM knockout alone is fairly well tolerated, and additional genomic stress is needed to bring about toxicity in

neurons(66). A follow-up study utilizing this new mouse model explores an intriguing explanation for why certain neuronal populations seem selectively vulnerable to neurodegeneration observed in AT (and other DNA damage syndromes for that matter)(67). While both cerebellar neuron subtypes (Purkinje and granule cells) experience DNA break repair deficiencies in the ATM/APTX double mutant mouse, ATAC-seq (assay for transposase-accessible chromatin using sequencing) revealed that Purkinje cells harbor uniquely open regions of chromatin that were perturbed by aberrant RNA splicing and subsequent R-loop formation (a three-stranded structure formed by an RNA:DNA template hybrid and the non-template DNA strand)(67). The consequent disruption in Purkinje cell gene expression ultimately results in cerebellar atrophy and ataxia.

1.3 DNA damage in neurodegenerative disease

In addition to observations made from genetic disorders, work characterizing the molecular pathophysiology of age-associated neurodegenerative diseases further implicate DNA damage in brain aging and disease. In the following subsections, we highlight recent publications that explore the effects of DNA damage in the context of age-associated neurodegenerative disease, as well as recently developed DNA lesion mapping methodologies that may help us better define regions of the neuronal genome that are vulnerable to lesion accumulation and repair(39).

1.3.1 Oxidative DNA damage

Increased oxidative DNA damage is observed in brain tissue from aged individuals(68) and patients with AD(69–71), Parkinson's disease (PD)(72), Huntington's disease (HD)(73), and amyotrophic lateral sclerosis (ALS)(74,75). This is also accompanied by an age-associated decline in BER efficiency(71,76,77). Recently, a mechanism for the age and disease-associated increase in 8oxoG has been proposed. Specifically, the histone deacetylase HDAC1 has been shown to be critical for the repair of age-associated 8oxoG accumulation by increasing the activity of the DNA glycosylase OGG1(78). In

fact, the pharmacological activation of HDAC1 was shown to mitigate oxidative lesion accumulation in both aged mice and 5XFAD mice (mice expressing human APP and PSEN1 with five familial AD mutations), and improve cognition in 5XFAD mice(78). Importantly, the location of such oxidized bases has proven to be an important mediator of their neurotoxicity. Specifically, the aging brain contains increased 8oxoG at the guanine-rich promoters of genes regulating synaptic function, resulting in their transcriptional suppression (Figure 1-2)(79). 8oxoG is capable of repressing gene transcription through many mechanisms, including blocking transcription factor binding(80,81), recruiting chromatin remodelers that result in the methylation of gene promoters(82,83), and erroneous repair through BER, which could result in single nucleotide variations (SNVs). Accordingly, single-cell whole genome sequencing has revealed that somatic SNVs located near neuronal genes increase with age in human neurons, presumably due to errors in BER, NER, and transcription-associated repair (Figure 1-2)(15,17). It is possible that at the population level, this accumulated genomic diversity in postmitotic neurons could result in neuronal dysfunction.

Aberrant DNA repair may also directly mediate the severity of neurodegenerative disorders like HD, whose toxicity is derived from the CAG trinucleotide expansion of the Huntingtin gene. Specifically, age-dependent CAG expansion occurs in the brains of individuals with HD, gradually increasing the toxicity of the Huntington protein in the striatum. Notably, CAG expansion has been found to be dependent upon DNA repair proteins such as OGG1, MLH1, and MSH2, whose detection of oxidized or mismatched bases in these repetitive elements could potentially elicit erroneous repair, leading to CAG expansion(84–88). Gene-wide association studies have further identified SNPs in DNA maintenance genes that influence the age of onset in this disease(89,90). Therefore, erroneous DNA repair mechanisms also directly influence HD severity.

To further understand how DNA lesions accumulate in the brain, multiple sequencing techniques

are now available that map these DNA lesions genome-wide. Previously, studies have approximated the location of 8oxoG lesions through OGG1 ChIP-seq(91), which is a somewhat indirect method as it captures lesion detection rather than the lesion itself. Newer antibody or biotin-conjugate methods have also been developed to directly target 8oxoG(92,93), however these techniques only permit a window of resolution of around 150 nucleotides. To this end, single-nucleotide resolution DNA lesion sequencing techniques are now being developed that could better define oxidative hotspots in the neuron genome. One such sequencing technique, Click-Code-seq, utilizes BER excision enzymes and click chemistry to specifically tag 8oxoG(94). Another sequencing technique, Nick-seq, is capable of detecting a variety of DNA modifications based on the enzyme or chemistry used to first convert the DNA modification to a strand break(95). It will be interesting to see if these new technologies can be applied to models of neurodegeneration as well as the postmortem human brain.

1.3.2 SSBs and DSBs

A plethora of studies document increased levels of both SSBs and DSBs in AD, HD, PD, and ALS(3,4,8,30,96–99), and their accumulation seem to correlate with important milestones in disease progression. Specifically, increased DDR foci are observed in neurons from individuals with mild cognitive impairment (MCI) and AD compared to aged counterparts(8). Similarly, DSB marker proteins correlate with cognitive impairment in individuals with low levels of amyloid and tau pathology(9). More recently, increased ROS and DSBs have also been documented in neurons derived directly from sporadic AD patient fibroblasts, indicating that age-dependent features of genomic instability are recapitulated in human *in vitro* models of disease(100). These findings have led to the hypothesis that DNA strand breaks may be a contributing factor to disease progression(22).

As previously discussed, one mechanism of DNA break-mediated neurodegeneration may stem from PARP1 hyperactivity. Increased PARP1 activation and elevated poly(ADP-ribose) has been

observed in numerous neurodegenerative disorders and their associated animal models(101,102). For example, oxidative damage-induced poly(ADP-ribose) mediates α-synuclein aggregation and consequent neurodegeneration in PD(103), facilitates the formation of cytoplasmic TDP-43 foci in ALS(104,105), and can mediate neuroinflammatory activity in AD(106). In combination with studies utilizing XRCC1-deficient neurons, these findings have motivated the development of PARP inhibitors as a potential therapeutic for a variety of nervous system disorders(102).

In addition to PARP1 activity, many genes that encode the building blocks of neurodegenerative proteinopathies have been found to play a role in DDR as well. For example, the genes whose mutations can cause ALS or frontotemporal dementia (fused in sarcoma (FUS) and transactive response DNA binding protein 43 (TDP-43)) are involved in SSB and DSB detection and repair. FUS is an RNA/DNA binding protein that has been found to facilitate DSB repair through its colocalization with HDAC1(107). Furthermore, phosphorylation of FUS occurs in response to DSB detection by proteins ATM and DNA-PK(108,109), and FUS activates and recruits the XRCC1-LIG3 complex to sites of oxidative DNA damage in a PARP1-dependent manner(110,111). Recently, TDP-43 was also found to be directly involved in NHEJ through its recruitment and stabilization of the XRCC4-LIG4 complex at DSBs(112,113). The Huntington protein may also play a role in DNA damage detection, potentially serving as a scaffold for ATM at sites of oxidized DNA(114), and ATXN3 and PNKP at sites of transcription-coupled DNA break repair(115). Finally, α-synuclein, whose cytoplasmic aggregation is a hallmark of PD, is able to bind double-strand DNA and facilitate NHEJ in homeostasis(116). However, toxic aggregation of α-synuclein in the nucleus or cytosol elicits the accumulation of DSBs(117,118). Tau may also play a role in DSB repair as well, as its deletion in the mouse brain leads to the accumulation of DSB foci in neurons(119,120).

While these findings have firmly established DNA breaks as a mechanism of neurodegenerative

disease, the mechanisms by which break location may contribute to disease progression are not well described. To this end, genome-wide profiling of DNA breaks in post-mitotic neurons have revealed that their locations are likely major mediators of their toxicity. As described earlier, the use of nucleoside analog incorporation to map DNA repair has led to the observation that postmitotic neurons harbor SSBs and other forms of breaks in the regulatory regions of genes that modulate synaptic plasticity and neuronal function(11,12). It follows that while these breaks may be functionally relevant, over time, their erroneous repair could lead to disruptive translocations, mutations, and genomic instability.

1.4 Neuroinflammation associated with DNA damage

In addition to DNA damage, neuroinflammation has emerged as a core feature and mechanism of neurodegenerative disease. Indeed, many of the risk genes associated with AD mediate their effects through microglia, the brain-resident macrophages(121–123). More recently, researchers have identified senescent-like brain cells in murine models of AD and tauopathy, and their removal via senolytic drugs seems to mitigate pathology and improve cognition(18,19,21,124). Thus, senescence is now considered as a potential driver of neuroinflammation and neurodegeneration. Importantly, while not well-studied in the context of the degenerating brain, the mechanistic link between DNA damage and senescence has already been defined in great detail(125–127). Below, we discuss recent mechanistic insights between DNA damage and neuroinflammation, and how DNA damage may influence neurodegeneration through the activation of senescent-like signaling from different brain cell types.

1.4.1 DNA damage induces senescence

DNA damage is a potent activator of inflammatory signaling and senescence(128–131). Initially defined by the permanent cessation of cell division and evasion of apoptosis, senescence is an age-associated cellular state that is thought to contribute to organismal aging, cancer, and more recently,

neurodegeneration(132). Importantly, removal of senescent cells promotes healthy aging in mice, making senescence-associated inflammatory signaling an attractive target of therapeutic intervention for aging and age-related disease(124,133–135). Senescent cells can be identified by a variety of factors, one being the secretion of pro-inflammatory cytokines (termed senescence-associated secretory phenotype (SASP)) to modulate their microenvironment. Initially, induction of persistent DDR signaling in cell cultures including fibroblasts(128,129), bone marrow-derived macrophages (BMDMs)(131), and primary monocytes(130) was found to elicit the SASP(129). This secretory profile was found to be at least partially ATM-dependent, implying the importance of DSB repair specifically in immune activation(128,130). Previous work with AT fibroblasts had shown that the canonical immune transcription factor NFκB is activated in an ATM-dependent manner following treatment with a radiomimetic, ionizing radiation, or topoisomerase inhibitor(136–138). This suggested NFκB was critical for the expression of pro-inflammatory signaling molecules following DNA damage. Subsequent studies confirmed that following DSB induction, activated ATM couples with a number of protein intermediates leading to its cytoplasmic transport and downstream activation of NFκB(127,139,140). In addition to inducing the expression of inflammatory signaling proteins, NFκB also exerts anti-apoptotic activity through the expression of caspase inhibitors such as FLIP, XIAP, and c-XIAP. This directly counteracts pro-apoptotic activity mediated by DNA damage-induced p53 signaling. Thus, the interplay between NFκB and p53 strongly influence cellular fate following DNA damage accumulation(141).

Interestingly, a subsequent study revealed that DNA damage can also evoke type-I interferon signaling in AT cells due to the accumulation of cytosolic DNA fragments, suggesting activation of inflammatory signaling via DNA damage can occur independent of the DSB DDR(131). Rather, this pathway is initiated through the detection of self-DNA in the cytosol, the source of which can be DNA damage(142–145), micronuclei rupture(146,147), deficient nuclease activity(148,149), or de-repression

of retrotransposable elements(150). In addition to genomic DNA, mitochondrial DNA (mtDNA) is also a major source of innate immune activation(151,152). Cytosolic self-DNA are sensed by the nucleic acid sensor cyclic GMP-AMP (cGAMP) synthase (cGAS) which produces the second messenger cGAMP upon binding to free floating DNA. The production of cGAMP in turn activates Stimulator of IFN Genes (STING). The activation of STING mediates a number of downstream signaling cascades, including the activation of both IRF3 and NFκB, thus resulting in the expression of interferons and pro-inflammatory cytokines(126,153,154). Therefore, DNA damage has direct molecular links to senescence-associated inflammatory signaling, both through DDR pathway activation and the mis-localization of DNA itself (Figure 1-3).

Additional mechanisms exist to elicit inflammatory gene transcription following the detection of cytosolic nucleic acids(155). This includes TLR9 (Toll-like receptor 9), which binds to double-stranded DNA engulfed in endosomes, particularly bacterial DNA or mtDNA. This recruits adaptor protein MYD88 (myeloid differentiation primary response 88) to activate NFκB and stimulate the expression of inflammatory cytokines. An additional mechanism of cytosolic DNA-mediated inflammation is through the NLRP3 inflammasome, which senses cell stressors (such as cytosolic DNA) to activate the cleavage of pro-1L1b and pro-IL18 via Caspase I to elicit their secretion. In particular, microglial NLRP3 has been shown to be a major driver of amyloid beta and tau toxicity in AD, suggesting its activation has important implications for disease progression(156–158).

Interestingly, work characterizing the neurodevelopmental defects observed in the neuroinflammatory disorder Aicardi-Goutières Syndrome (AGS), a type I interferonopathy, indicates that DNA damage can mediate cellular toxicity through multiple different mechanisms in the same disease. AGS is caused by mutations in genes that regulate nucleic acid metabolism. For example, deficits in RNASEH2, an enzyme responsible for removing ribonucleotides from DNA and resolving R-loops,

comprise more than half of AGS diagnoses(159). Accordingly, RNASEH2 murine models of AGS reveal that CGAS-STING sensing of micronuclei is the cause for type I IFN signaling in this disease(147,160,161). However, recent work investigating the cause of AGS neurotoxicity revealed that it is the DDR-mediated activation of p53, not CGAS-STING, that causes neuron cell death, although increased micronuclei and R-loops were observed in astrocytes(162). This indicates that different phenotypes of DNA damage response deficits are mediated by different pathways, which may have preferential function in different cell types.

1.4.2 Senescence-associated inflammation in brain aging and neurodegeneration

It has since been shown that removal of senescent cells in the brain mitigates neurofibrillary tangle (NFT) burden, amyloid burden, neuronal loss, and cognitive decline in mouse models of tauopathy(18,19), AD(21), PD(163), and normal aging(124). Notably, each of these studies attribute different cell types as the primary sources of senescence. For example both microglia(19), astrocytes(19), and neurons(18) have been found to display senescent-like phenotypes in Tau P301S mice, and have been proposed as drivers of cognitive decline and neurodegeneration. Additionally, senescent astrocytes have been identified as modulators of PD pathology(163). Senescent-like phenotypes have also been identified in oligodendrocyte precursor cells (OPCs) in APP/PS1 mice, and their removal has been shown to mitigate amyloid load and cognitive decline(21). Finally, removal of senescent microglia from aged mice has been found to improve cognition(124). In total, these findings place senescence as an encouraging target for therapeutic intervention in neurodegenerative disease, but bring into question how senescence presents in different brain cell types, and how this might affect the progression of various diseases.

Studies have also made more direct links between DNA damage, neuroinflammation, and neurotoxicity. For example, ATM-deficient microglia have been shown to accumulate cytosolic DNA,

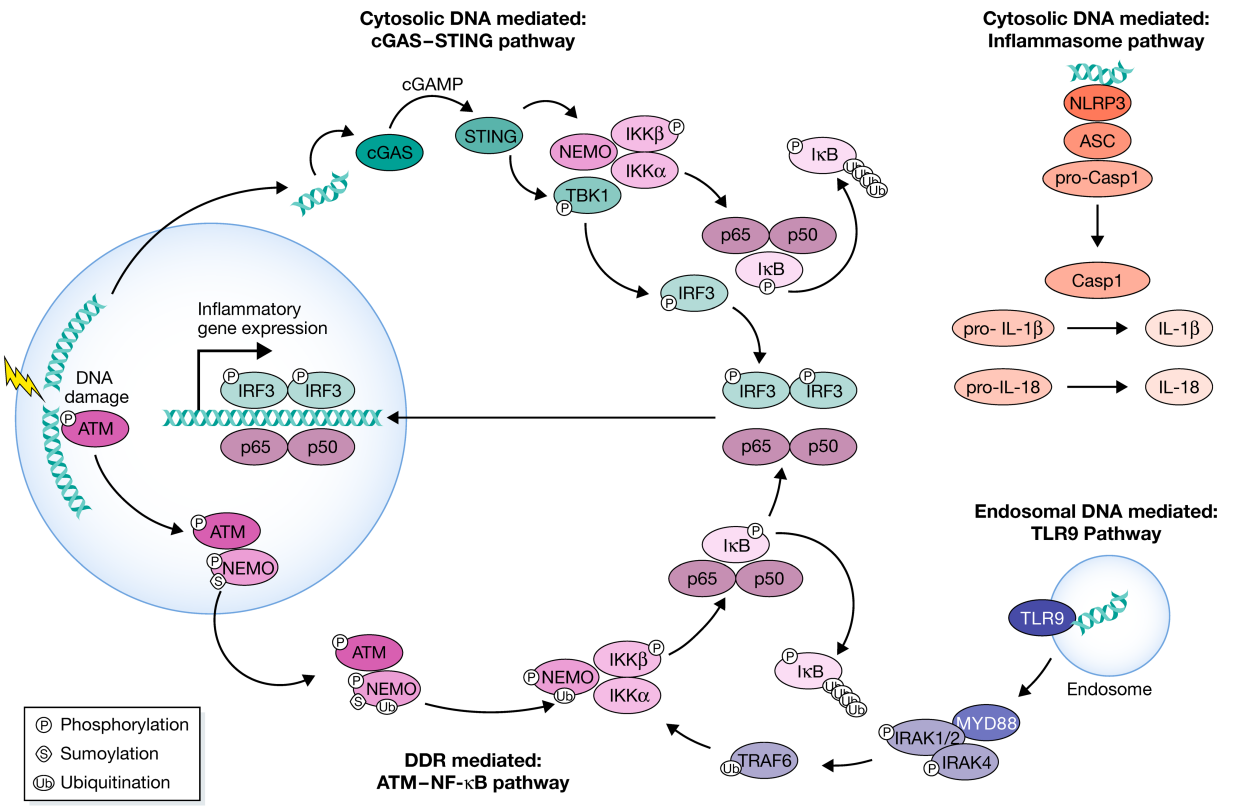

Figure 1-3 DNA damage initiates inflammatory signaling through DDR and cGAS-STING. ATM-NFκB pathway: The activation of ATM by DSBs leads to its coupling with NEMO in the nucleus. NEMO is phosphorylated by ATM and SUMOylated by PIASy in a PARP1-dependent manner, which is not shown here. These modifications lead to NEMO monoubiquitination, and the ATM-NEMO complex is transported to the cytoplasm. Here, NEMO partners with IKKb and IKKa to form the active Inhibitor of KappaB Kinase (IKK) complex. The IKK phosphorylates IkB, allowing NFκB to be transported to the nucleus. The most common form of NFκB is the heterodimer p50-p65, shown here. The phosphorylation of IkB leads to its polyubiquitination and subsequent degradation. cGAS-STING pathway: DSBs result in the leakage of self-DNA into the cytosol, which is sensed by cGAS. cGAS generates second messenger cyclic GAMP. cGAMP binds to STING, which activates TANK-binding kinase 1 (TBK1), which in turn activates IFN Regulatory Factor 3 (IRF3). Homodimerized IRF3 transports to the nucleus and activates the expression of inflammatory genes. STING also facilitates the formation of the IKK complex, which phosphorylates IkB to activate NFκB. TLR9 pathway: Endosomal double strand DNA is bound by TLR9, activating MyD88, which interacts with and activates IRAK1,2,and 4. IRAK1 and 4 dissociate from MyD88 and activate TRAF6. TRAF6 ubiquitinates NEMO, a member of the IKK complex that results in NFκB translocation into the nucleus. Inflammasome pathway: NLRP3 detects cytosolic DNA, leading to the assembly of the NLRP3, ASC, pro-Caspase I inflammasome. pro-Caspase I autoproteolytically matures to functional Caspase I, which cleaves pro-IL1b and pro-IL18 to generate functional IL1b and IL18.

thus activating the cGAS-STING pathway to elicit pro-inflammatory and neurotoxic signals(164,165). Interestingly, sequencing the cytosolic DNA fragments from these microglia revealed that most were derived from the nuclear DNA as intergenic repetitive elements, suggesting that the source of cytosolic DNA may not be random(166). Recent single-nucleus RNA sequencing of AT cerebella reveal that microglial activation likely precedes neuronal degeneration, further emphasizing the role of microglia in ATM-mediated neuropathology(167).

1.4.3 The role of neuronal DNA damage in neuroinflammation

Notably, the concept of a senescent-like phenotypes in neurons has been particularly controversial, presumably because senescence was initially defined in the context of cycling cells(20,168). Nevertheless, observations of senescent-like phenotypes in neurons have been reported for quite some time. As early as 2012, the term "senescence" was used to describe pathological features of neurons in the aged mouse brain, including increased DSBs, lipid peroxidation, and senescent-associated β-galactosidase staining(169). Here, DSBs were considered the major driver of these senescence-associated phenotypes because knock-out of p21, a protein activated by p53 to initiate DSB-induced cell cycle arrest, was able to mitigate their enrichment. Interestingly, re-inspection of older transcriptional data also revealed similar enrichment in AD neurons. In a 2006 study, neurons with high levels of tau pathology or no tau pathology were isolated from AD brain tissue and transcriptionally characterized(170). This dataset was later re-analyzed to show that neurons with high levels of tau were enriched for signatures of DNA damage and senescence(18,170). Senescent-like phenotypes in neurons have also been noted in other models of aging and neurodegeneration(22,171).

Because DNA damage accumulates in neurons early on in AD, and because it is also a primary driver of senescence, it is worth hypothesizing that DNA lesions mediate neurodegeneration at least in part through neuronal senescence, although senescence in other cell types clearly also plays important

roles in neurodegeneration. Nevertheless, future research will have to dissect how different cell types react to senescent neurons, and how this may facilitate the development of neurodegenerative disease. Importantly, as DNA damage is a well-established source of inflammatory signaling, this uncovers a previously unstudied aspect of neuronal response to DNA damage. Compared to microglia and astrocytes, the capacity for inflammatory signaling in neurons has received little attention. Indeed, the protein machinery required to detect cytosolic DNA such as STING is reported to be low in neurons compared to glial cells(164,172). However, work examining the immune response to neurotropic viral infections reveal neuron-derived inflammatory signaling is a critical feature of the antiviral response(173–175). The detection of viral nucleic acids utilizes the same cGAS-STING pathway as that described for detection of self-DNA within the cytosol of senescent cells, suggesting that the mechanism of innate immune signaling in DSB-bearing neurons may be of some significance. Indeed, observations of neuron-derived immune signaling at early stages of neurodegenerative disease indicate that this may play a role in disease progression(176,177). Notably, neuronal cGAS-STING has been shown to be activated in models of HD and ALS, suggesting that toxic protein aggregates may stimulate DNA release (mitochondrial or genomic) to initiate NFκB activation in neurons(178,179).

Intriguingly, the inflammatory transcription factor NFκB also plays neuron-specific roles in learning and memory. Inhibition of NFκB signaling specifically in neurons impairs synaptic plasticity and synaptogenesis(180,181). Furthermore, suppression of neuronal NFκB *in vivo* render neurons more susceptible to kainic acid-induced neurotoxicity(182). These data suggest that on top of its function as a pro-survival and pro-inflammatory transcription factor, NFκB is also critical for homeostatic neuronal function(183). Thus, dysregulated NFκB signaling in neurons could be a key mechanism linking DNA damage accumulation, altered synaptic function, and disease progression.

Chapter 2

Neurons burdened by DNA double strand breaks incite microglia activation through antiviral-like signaling in neurodegeneration

2.1 Introduction

Loss of genomic integrity is linked to aging and neurodegeneration (3,184). DNA damage repair pathways are transcriptionally prominent in the aging brain, and many age-associated neurodegenerative diseases exhibit both accumulation of DNA lesions and reduced DNA repair efficiency (70,79,185). The most toxic of these lesions, the DNA double-strand break (DSB), can drive many phenotypes of aging including senescence, mutation, and cell death. Postmitotic neurons are particularly susceptible to these threats due to their long lifespan, high metabolic activity, and limited DSB repair capacity. While DSB accumulation in neurons is a well-documented feature of aging and neurodegeneration, the transcriptional profile adopted by such population of neurons remains largely unknown.

The accumulation of DSBs is an early feature of Alzheimer's disease (AD), suggesting that they may act as an initiating lesion of toxicity (8). Multiple mouse models of neurodegeneration phenocopy increased DSBs at early pathological stages, including the Tau P301S and P301L tauopathy models, the inducible CK-p25 model, and the hAPP-J20 amyloid pathology model (32,77,186). Recent studies characterizing DNA strand breaks in postmitotic neurons reveal that break location may underlie the functional decline of the brain in aging and neurodegenerative disease (11,12). However, regardless of location, the downstream biological effects of DSB burden in neurons are unclear.

Here, we sought to characterize the biological consequences of DSB accumulation in neurons. We also investigated how this impacts mechanisms of neuroinflammation in age-associated neurodegenerative disease. We utilized fluorescence-activated nuclei sorting (FANS) followed by bulk and single-nucleus RNA-sequencing to transcriptionally characterize neurons burdened with DSBs in the CK-p25 mouse model of neurodegeneration. We found that DSB-bearing neurons activate innate immune signaling pathways reminiscent of those expressed by senescent cells and neurons infected by virus (128,142,174). This is accompanied by degradation of neuronal identity. The gene expression patterns of DSB-burdened neurons were enriched in excitatory neurons from AD postmortem human brain. Spatial transcriptomics of the CK-p25 forebrain revealed signatures of microglial inflammation were proximally associated with DSB-bearing neurons. Correspondingly, suppression of the NFκB transcription factor in neurons suppressed microglial proliferation and activation at both early and late stages of disease, and also rescued synapse loss. Together, these data establish a novel signaling relationship between neurons burdened with DSBs and microglia in age-associated neurodegenerative disease.

2.2 Results

2.2.1 Identification of DSB-bearing neurons at early stages of disease in a mouse model of neurodegeneration

We utilized the CK-p25 mouse model of inducible neurodegeneration to understand how DSB-bearing neurons contribute to disease development. In these mice, the *CamkII* promoter drives the expression of the neurotoxic protein fragment p25 through a doxycycline (dox)-off system (187). P25 is the calpain-cleaved product of p35, an activator of cyclin dependent kinase 5 (Cdk5). Previously, we determined that the first pathologies observed in these mice are increased DSBs in neurons (186) and activation of microglia (188). These pathologies occur 1-2 weeks after the onset of p25 expression when mice are taken off dox. Intracellular amyloid-beta accumulation also occurs as early as 2 weeks after induction (189).

Neuronal loss, learning deficits, and tau hyperphosphorylation are also observed in the following 4-12 weeks (187,189,190). These pathological events are inducible and occur in a highly concerted and predictable manner.

The phosphorylation of the histone variant H2A.X (γH2AX) by ATM kinase occurs rapidly after DSB detection. This post-translational histone modification is essential for efficient DSB recognition and repair, and is a robust DSB biomarker. Using flow cytometry, we identified a distinct population of nuclei expressing high levels of γH2AX (γH2AX^{hi}) at the two-week time point in the CK-p25 cortex, but not in the CK control cortex (Figure 2-1.A). CK mice express the *CamkII*-driven tetracycline transactivator (tTA), but not p25. We performed a timeline analysis to determine when γH2AX^{hi} nuclei begin to accumulate in the CK-p25 cortex. γH2AX^{hi} nuclei were detectable as early as one week after induction (1.038 ± 0.2627 % population), peaked at two weeks (4.614 ± 0.9416 % population), and gradually decreased thereafter (Figure 2-1.B). The significant reduction in γH2AX^{hi} nuclei at six weeks corresponds

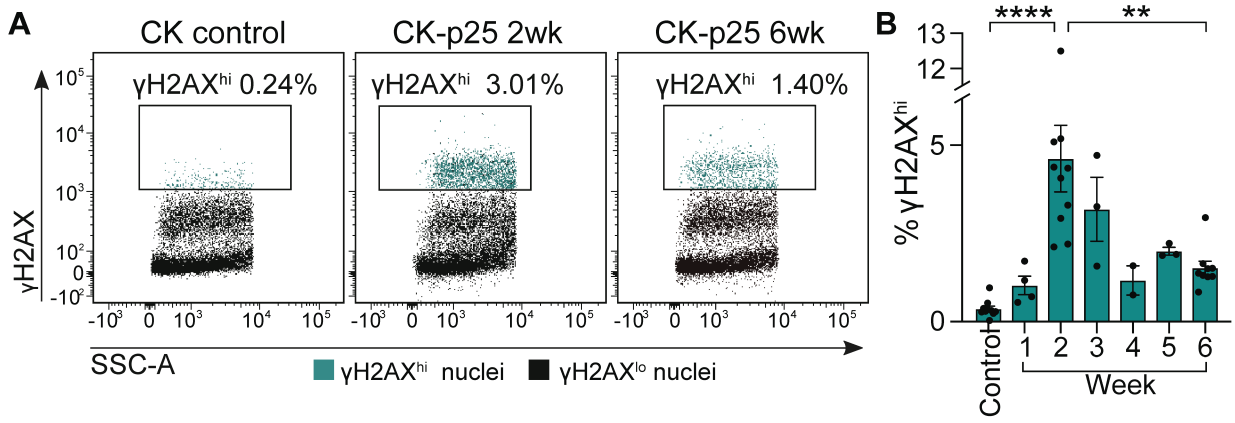

Figure 2-1 γH2AX^{hi} nuclei accumulate in the CK-p25 cortex at early stages of neurodegeneration. (**A**) Flow cytometry dot plots of γH2AX^{hi} nuclei (turquoise) from CK and CK-p25 cortex. Percent total population is indicated above the gating box. (**B**) Quantification of percent γH2AX^{hi} for 1 through 6 weeks induction. Each data point represents percent γH2AX^{hi} nuclei from one mouse cortex. One-way ANOVA with Tukey's test for multiple comparisons. Data are pooled from 4 independent experiments. Error bars represent standard error of mean (S.E.M.); ****P<0.0001, **P<0.01.

with previous observations of neuronal loss in this model, suggesting that γH2AX^{hi} cells degenerate by six weeks (187,190). We were able to observe similar γH2AX^{hi} population dynamics using immunofluorescent microscopy (Figure 2-2). We did not detect γH2AX-immunopositive nuclei after only four days off dox, suggesting that one week is the earliest time point at which this population appears.

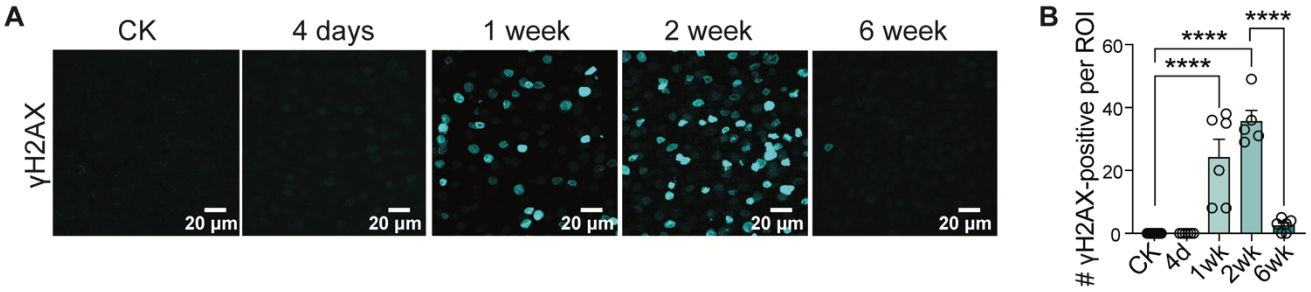

Figure 2-2 γH2AX+ nuclei accumulate as early as 1 week in the CK-p25 cortex. (**A**) Representative images of γH2AX immunostaining in the CK-p25 cortex over a 6-week timeline. (**B**) Average number of γH2AX+ nuclei quantified per image at each timepoint. Each data point represents one mouse. Error bars represent standard error of mean (S.E.M.); ****P<0.0001; One-way ANOVA with Tukey's test for multiple comparisons. Data are averages of 4 images per mouse.

We next sought to identify the cell type composition of γH2AX^{hi} nuclei. While most γH2AX+ nuclei were immunoreactive for NeuN, a general neuron marker, 21.51 ± 2.36 % did not have strong NeuN immunoreactivity (Figure 2-3). Furthermore, none of the γH2AX+ nuclei overlapped with markers of microglia (Iba1), astrocytes (GFAP), or oligodendrocytes and oligodendrocyte precursor cells (Olig2), indicating that the 21.51% with low NeuN immunoreactivity were not likely of glial origin (Figure 2-3). Interestingly, we found that 74.17 ± 1.27 % of γH2AX+ cells with low NeuN immunoreactivity were labeled with Neurod1, a neuronal transcription factor (Figure 2-4.A). 88.98 ± 2.16% of γH2AX+ cells with high NeuN immunoreactivity were labeled with Neurod1 as well (Figure 2-4.A). Additionally, we observed that 85.22 ± 4.52% of γH2AX+ cells with low NeuN immunoreactivity were labeled with GFP, which is fused to the p25 transgene and driven by the CamKII promoter, an excitatory neuron-specific

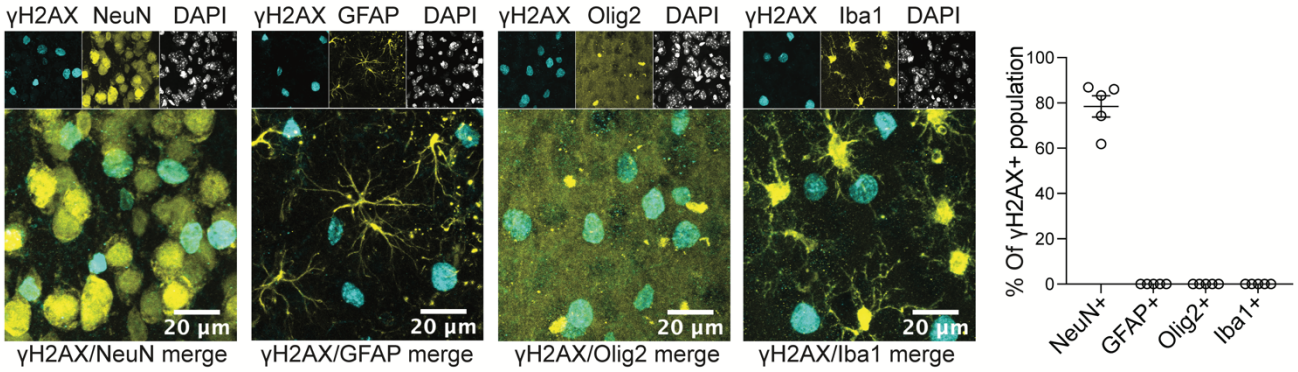

Figure 2-3 γH2AX+ nuclei do not express glial markers. (left): Representative images of cell type and γH2AX immunostaining in the 2-week induced CKp25 cortex. Cell type markers from left to right: neurons (NeuN), astrocytes (GFAP), oligodendrocytes and oligodendrocyte precursor cells (Olig2), microglia (Iba1). (right): Quantification of percent γH2AX+ nuclei overlapping with each cell type marker. Each data point represents one mouse. 50-100 γH2AX+ nuclei were analyzed for each mouse and cell type marker.

gene (Figure 2-4.B). 89.15 ± 3.55% of γH2AX+ cells with high NeuN expression were also labeled with GFP (Figure 2-4.B). These immunostaining analyses indicated that γH2AX+ nuclei with low NeuN immunoreactivity were likely excitatory neurons with some level of cell identity degradation. Degradation of neuronal identity is observed within aging and Alzheimer's disease patients (191), and reduced NeuN expression has been proposed as an indicator of declining neuronal health (192). Indeed, reduced NeuN expression or reduced NeuN immunoreactivity in neurons is an established feature of neuronal damage due to irradiation, ischemia, and axotomy (193–195).

To follow up on this observation, we performed additional flow cytometry analyses of γH2AX^{hi} nuclei, staining for both CamKIIa and NeuN. In support of our immunostaining analyses, we found that all γH2AX^{hi} nuclei were also labeled by CamKIIa (CamKIIa^{hi}), even those with low NeuN immunoreactivity (NeuN^{lo}) (Figure 2-5). Finally, to validate DNA damage response pathways were active in γH2AX^{hi} nuclei, we confirmed co-labeling with the active form of ATM kinase (p-ATM S1981) (Figure 2-6).

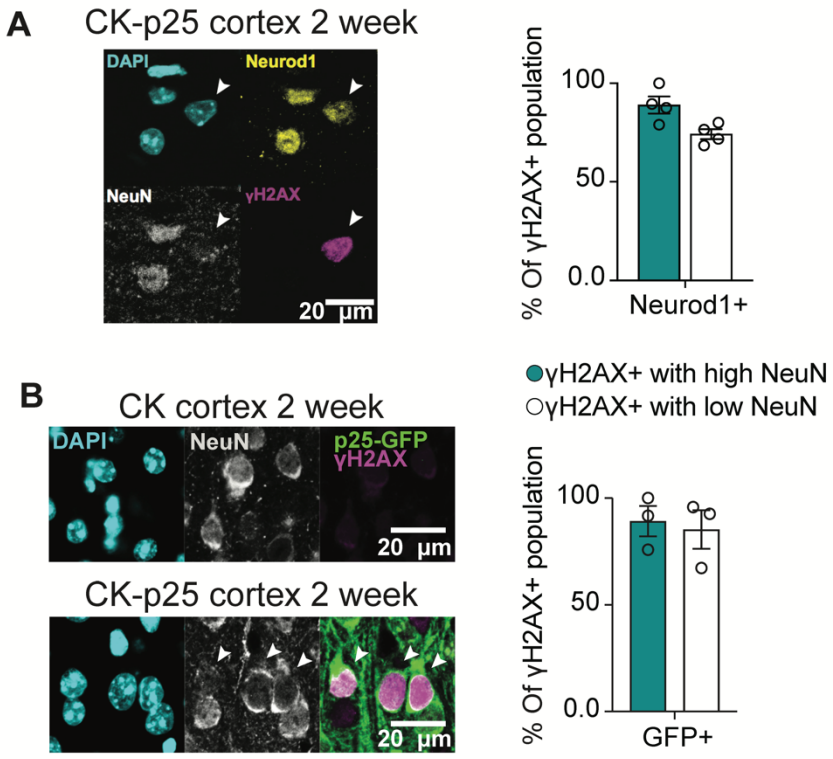

Figure 2-4 γH2AX+ cells with low NeuN express Neurod1 and GFP. (**A**) (left): Representative images of Neurod1, γH2AX and NeuN from CK-p25 cortex at the two-week time point. White arrowhead indicates a γH2AX+ nucleus with high Neurod1 immunoreactivity but low NeuN immunoreactivity. (right): Quantification of Neurod1 expression across γH2AX+ cells with high or low NeuN expression. Each data point represents percent γH2AX+ population with high or low NeuN expression from one CK-p25 mouse. (**B**) (left): Representative images of GFP, γH2AX, and NeuN immunostaining from CK and CK-p25 cortex at the 2-week time point. Arrowheads indicate γH2AX+ nuclei that express p25-GFP irrespective of NeuN immunoreactivity. (right): Quantification of GFP expression across γH2AX+ cells with high or low NeuN immunoreactivity. Each data point represents percent population of γH2AX+ cells with high or low NeuN immunoreactivity from one CK-p25 mouse.

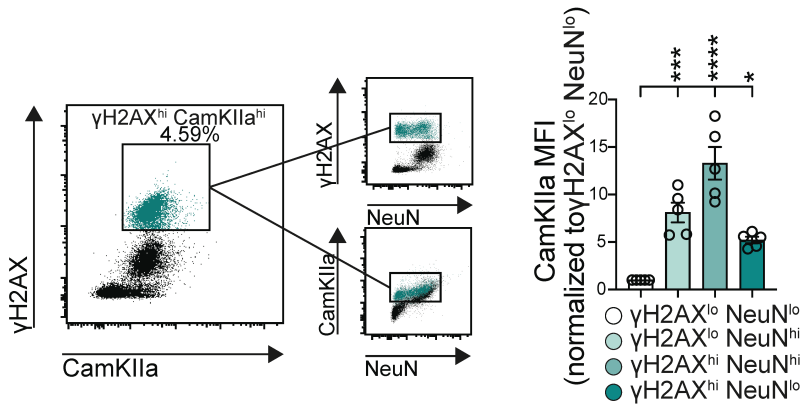

Figure 2-5 All γH2AX^{hi} nuclei are CamKIIa^{hi}. (left): Flow cytometry dot plot of γH2AX, CamKIIa, and NeuN immunoreactivity in nuclei from CK-p25 cortex. γH2AX^{hi} CamKIIa^{hi} nuclei are gated in the left graph. γH2AX^{hi} CamKIIa^{hi} nuclei are highlighted in turquoise in the right two graphs. (right): CamKIIa median fluorescent intensity (MFI) is quantified for γH2AX^{hi} and γH2AX^{lo} populations separated by NeuN expression (NeuN^{hi} or NeuN^{lo}). MFI values are normalized to the γH2AX^{lo} NeuN^{lo} population. Error bars represent standard error of mean (S.E.M); ****P<0.0001, ***P<0.001, *P<0.05; One-way ANOVA with Tukey's test for multiple comparisons.

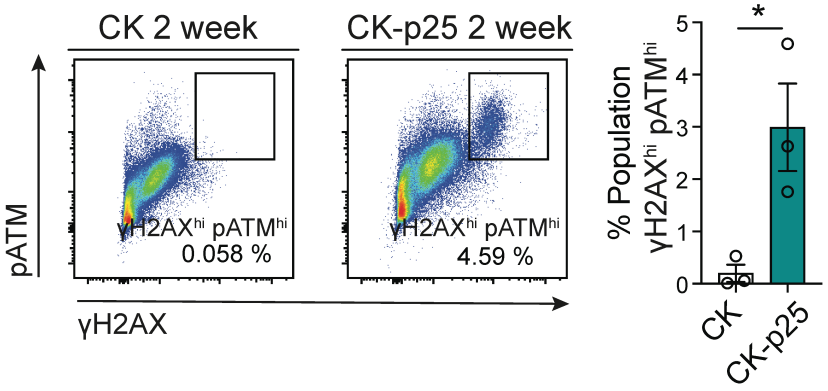

Figure 2-6 γH2AX^{hi} nuclei are pATM^{hi}. (left): Flow cytometry dot plot of γH2AX^{hi} pATM^{hi} nuclei in CK and CK-p25 cortex. (right): Quantification of γH2AX^{hi} pATM^{hi} nuclei in CK and CK-p25 cortex. Each data point represents percent γH2AX^{hi} pATM^{hi} nuclei for one mouse. Error bars represent standard error of mean (S.E.M.); *P<0.05, Student's T-test. Data are representative of 2 independent experiments.

2.2.2 DSB-bearing neurons express antiviral and senescence genes

To formally analyze the population of γH2AX^{hi} cells, we classified nuclei into four distinct populations: γH2AX^{lo} NeuN^{hi} ("Baseline" neurons), γH2AX^{hi} NeuN^{hi} (Stage 1 neurons), γH2AX^{hi} NeuN^{lo} (Stage 2 neurons), and γH2AX^{lo} NeuN^{lo} (putative non-neuronal cells, which we refer to as "Other") (Figure 2-7.A). We used fluorescence activated nuclei sorting (FANS) followed by bulk RNA sequencing to transcriptionally profile each population (Figure 2-7.B). All nuclei were collected for sequencing at the two-week time point, which was when we observed the peak density of γH2AX^{hi} nuclei.

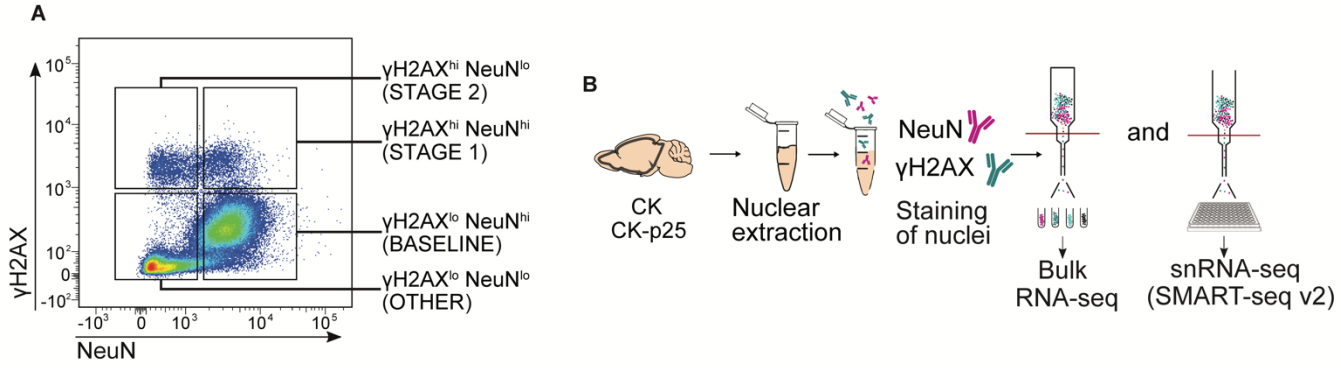

Figure 2-7 Gating and workflow schema for Stage 1&2 RNA-seq. (**A**) Representative dot plot of γH2AX and NeuN immunoreactivity in 2-week CK-p25 cortex. (**B**) RNA seq workflow for the gated populations. Bulk RNA-seq: n=2 per genotype for bulk RNA-seq, 2-week timepoint only. 50,000 nuclei were sorted from each gated population. snRNA-seq: n=3 per genotype × time point for SMART-seq, 1-week and 2-week time points.

We performed three differential expression analyses to characterize gene expression changes in these populations: Stage 1 vs. CK-p25 Baseline, Stage 2 vs. CK-p25 Baseline, and Stage 2 vs. Stage 1. Large transcriptional changes were observed in the first two comparisons. 3,031 upregulated and 717 downregulated transcripts were identified in Stage 1, and 5,055 upregulated and 3,792 downregulated transcripts were identified in Stage 2 ($\log_2$ fold change $\geq |1.0|$, adjusted p-value < 0.05) (Figure 2-8). Comparatively few transcripts were found differentially expressed between Stage 2 and Stage 1 (186 upregulated and 42 downregulated transcripts in Stage 2). Gene set enrichment analysis (GSEA)(196)

revealed that both Stage 1 and Stage 2 neurons displayed a significant enrichment for genes implicated in DSB repair, apoptotic signaling, and cell cycle re-entry, and a significant reduction in synaptic processes (Figure 2-9.A). These pathways were previously found to be dysregulated in both the CK-p25 mouse and AD human brain tissue (186,197).

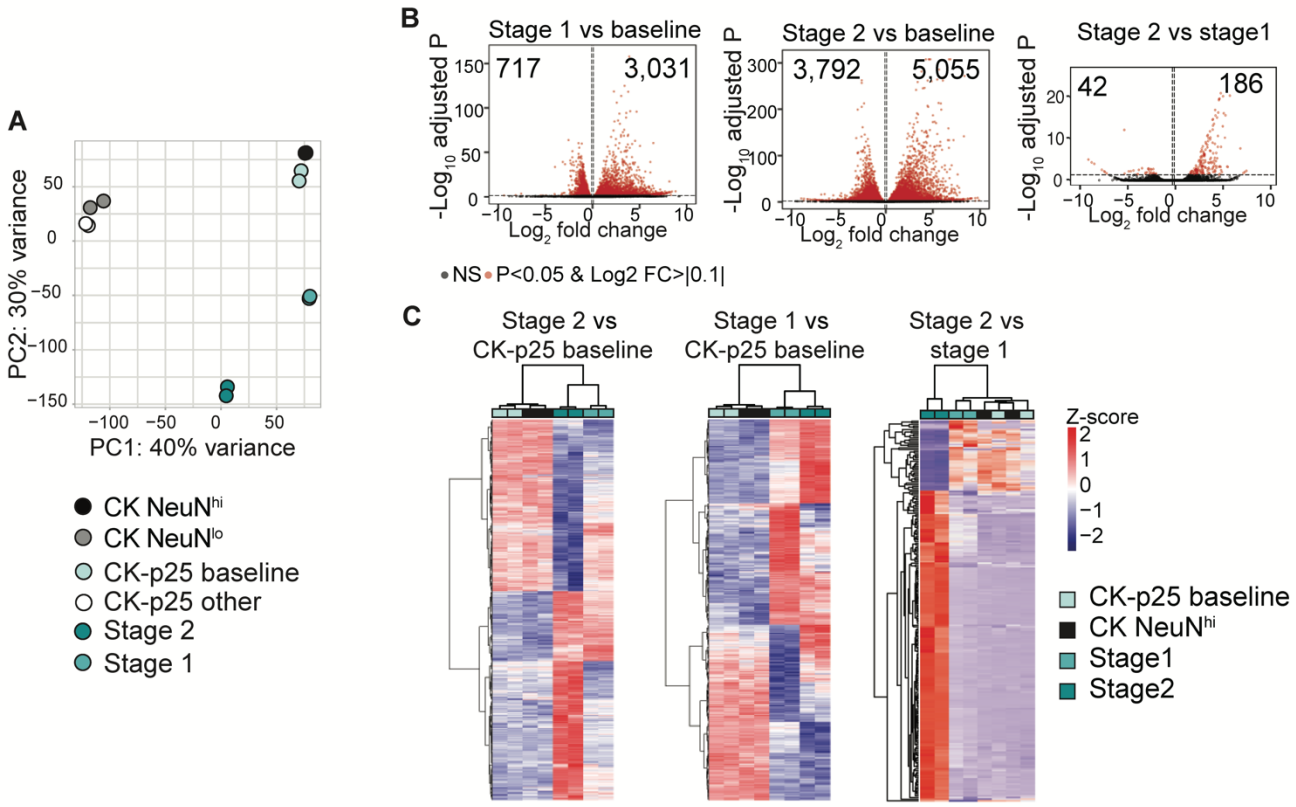

Figure 2-8 Differential analysis of Stage 1 and Stage 2 neurons. (**A**) Principle component analysis (PCA) of normalized gene expression matrix from CK and CKp25 subpopulations. Principle component 1 (PC1): 40% variance. Principle component 2 (PC2): 30% variance. (**B**) Volcano plots of Stage 1 vs. CK-p25 Baseline (top), Stage 2 vs. CK-p25 Baseline (middle), and Stage 2 vs. Stage 1 (bottom) contrasts. Gray circles: non-significant (ns) transcripts. Red circles: transcripts with FDR adjusted p-value <0.05 and log2 fold change >|0.1|. Number of significantly upregulated and downregulated transcripts are shown in the upper right and left corners of the volcano plots respectively. (**C**) Heatmap of differentially expressed genes from Stage 2 vs. CK-p25 Baseline and Stage 1 vs. CK-p25 Baseline contrasts. Each column represents one mouse.

Remarkably, we also found that a number of innate immune pathways were enriched in Stage 1 and Stage 2 neurons. This included gene ontology terms 'Senescence-Associated Secretory Phenotype (SASP)', 'Cytosolic sensors of pathogen-associated DNA', and 'Positive regulation of innate immune response' (Figure 2-3.A). Upon closer inspection, we observed an enrichment of genes linked to DSB-mediated activation of SASP signaling, particularly in Stage 2 neurons. This included nucleic acid sensors such as *Cgas* and *Zbp1*, NFκB subcomponents *Rela* and *Relb*, SASP factors *Il6*, *Il15, Ccl2, Cxcl10,* and interferon stimulated genes *Isg15 and Ifitm3* (Figure 2-9.B). Notably, a number of these genes are expressed in neurons following viral infection (174,198). These genes are also classic markers of senescence, suggesting that DSB accumulation elicits senescent and antiviral-like pathways in neurons.

Because the CK-p25 model is characterized by the development of type-I interferon-responsive microglia specifically by two weeks induction (188), we wanted to determine if DSB-bearing neurons express cytokines before microglia. To do this, we performed multiplexed fluorescent RNAscope in-situ hybridization in the CK-p25 cortex after one and two weeks off dox. We focused our profiling on *Cxcl10* and *Ccl2* because these pro-inflammatory chemotactic molecules were highly expressed in Stage 2 neurons and are known to be secreted by neurons upon viral infection, downstream of type-I IFN (174,199,200). First, we performed RNAscope for the excitatory neuron marker *Camk2a* to again confirm if γH2AX+ nuclei were of neuronal origin. Consistent with our RNA-seq and flow cytometry data, 98.81 ± 1.19% of γH2AX+ nuclei also expressed *Camk2a* (Figure 2-10). This high positivity rate confirms that γH2AX+ nuclei are nearly exclusively excitatory neurons. RNAscope analysis also revealed that γH2AX+ nuclei were the only cells to express *Cxcl10* and *Ccl2* at the one-week time point. In contrast, *Cxcl10* and *Ccl2* gene expression was highly enriched in γH2AX- nuclei at the two-week time point (Figure 2-11). Both γH2AX+ and γH2AX- nuclei had reduced *Cxcl10* and *Ccl2* expression by six weeks (Figure 2-11). Analysis of the cell type markers associated with *Cxcl10* expression revealed that the majority of γH2AX+

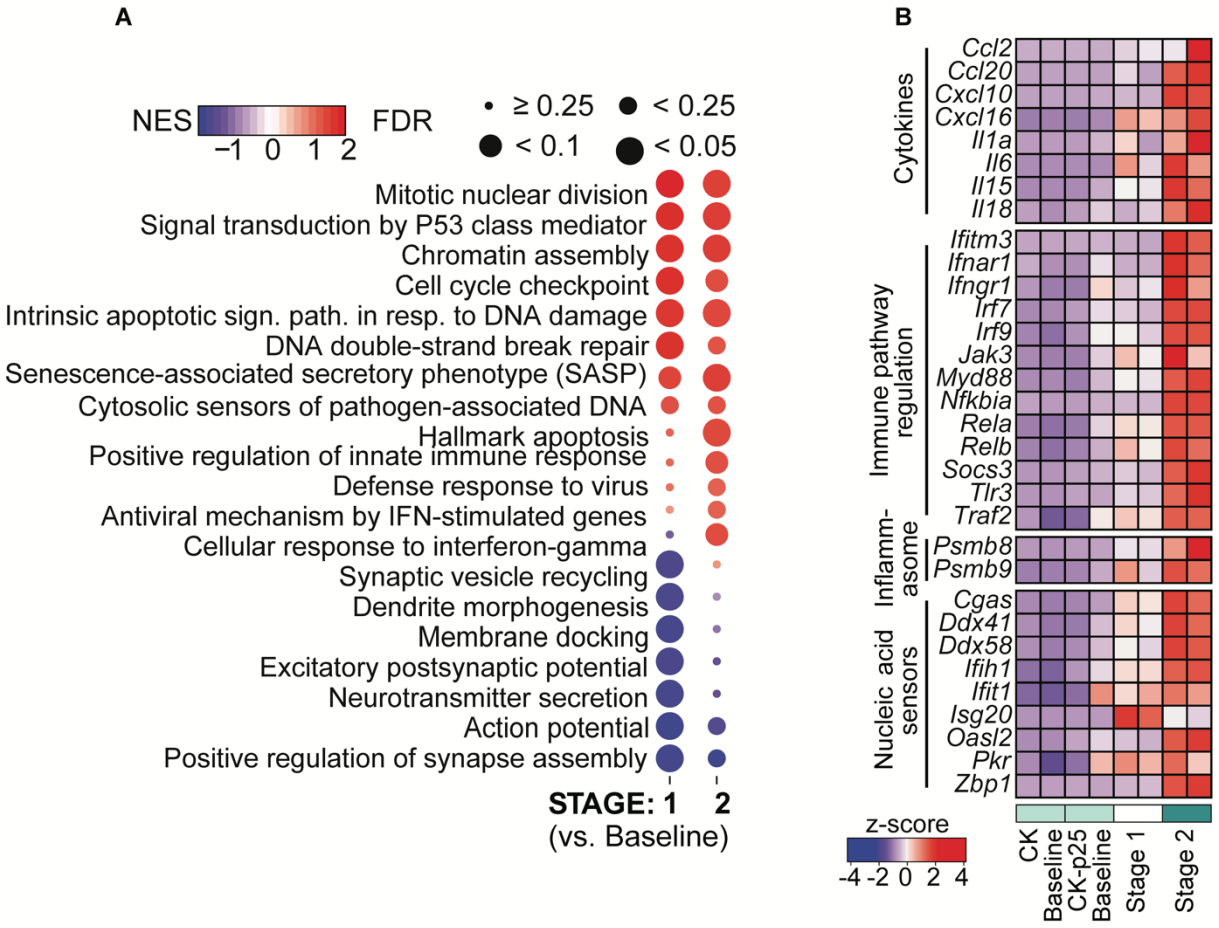

Figure 2-9 Stage 1&2 neurons express DNA damage and SASP genes. (**A**) Differential gene ontology terms from bulk RNA-seq data. Color indicates normalized enrichment score (NES). Size indicates false discovery rate (FDR). (**B**) Heatmap of differentially expressed genes belonging to inflammatory gene sets from bulk RNA-seq data. Each column represents one mouse.

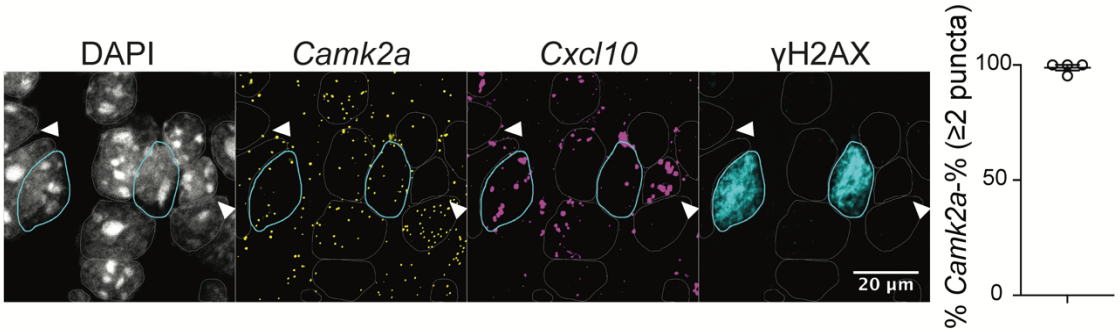

Figure 2-10 γH2AX+ nuclei express *Camk2a*. Representative image of RNAscope probes *Camk2a* (yellow) and *Cxcl10* (magenta), and γH2AX immunostaining (turquoise). The percent of γH2AX+ cells that are *Camk2a*+ (2 or more *Camk2a* puncta within the nucleus) are quantified to the right. Each data point represents one 2-week induced CK-p25 mouse. 17-42 γH2AX+ cells were quantified for each mouse. Turquoise outlines indicate γH2AX+ *Camk2a*+ cells. Gray outlines indicate γH2AX- cells. White arrows indicate *Camk2a*- cells. Data are representative of 2 independent experiments.

nuclei expressing *Cxcl10* were astrocytes and microglia (Figure 2-12). Taken together, these data indicate that expression of *Cxcl10* and *Ccl2* in γH2AX+ cells precedes their expression in glial cells, and that cytokine secretion from DSB-bearing neurons may be an early mechanism of glial cell recruitment and activation in the CK-p25 brain.

To identify the master regulators of DSB-associated neuronal immune signaling, we performed transcription factor enrichment analysis using Enrichr (201). A subset of immune pathway genes was extracted from the significantly upregulated genes in Stage 2 neurons for analysis. The overlap between this immune gene module and transcription factor target genes was then calculated. Multiple subunits of the NFκB complex were consistently enriched across Enrichr transcription factor libraries, including Rela, Nfkb1, and Relb (Table A1). Notably, the NFκB transcription factor plays a well-established role in SASP activation and the DSB response (202,203). We chose to focus on Rela, also known as p65, because it is a core member of the canonical NFκB complex, and it was most frequently enriched in the Enrichr analysis. We stained for p65 in one, two, and six-week CK and CK-p25 cortices. NFκB is normally sequestered in the cytosol, but translocates to the nucleus to form an active complex upon cellular insult. Nuclear p65 intensity was significantly higher in γH2AX+ cells compared to other γH2AX- cells at the one and two week time points (Figure 2-13), supporting evidence of increased NFκB transcriptional activity. By six weeks, there was no significant difference between γH2AX+ and γH2AX- nuclei in nuclear p65 intensity (Figure 2-13.B).

2.2.3 Single cell RNA-sequencing analysis in DSB-bearing neurons

In our bulk RNA-seq analysis, inflammatory gene expression was lower in Stage 1 neurons compared to Stage 2 neurons (Figure 2-9.B). We also performed a flow cytometry analysis of Stage 1 and Stage 2 populations over one through six weeks, and found that one week after induction, Stage 1 neurons made up 75% of all $\gamma H2AX^{hi}$ neurons, while Stage 2 neurons made up the remaining 25%. By two weeks

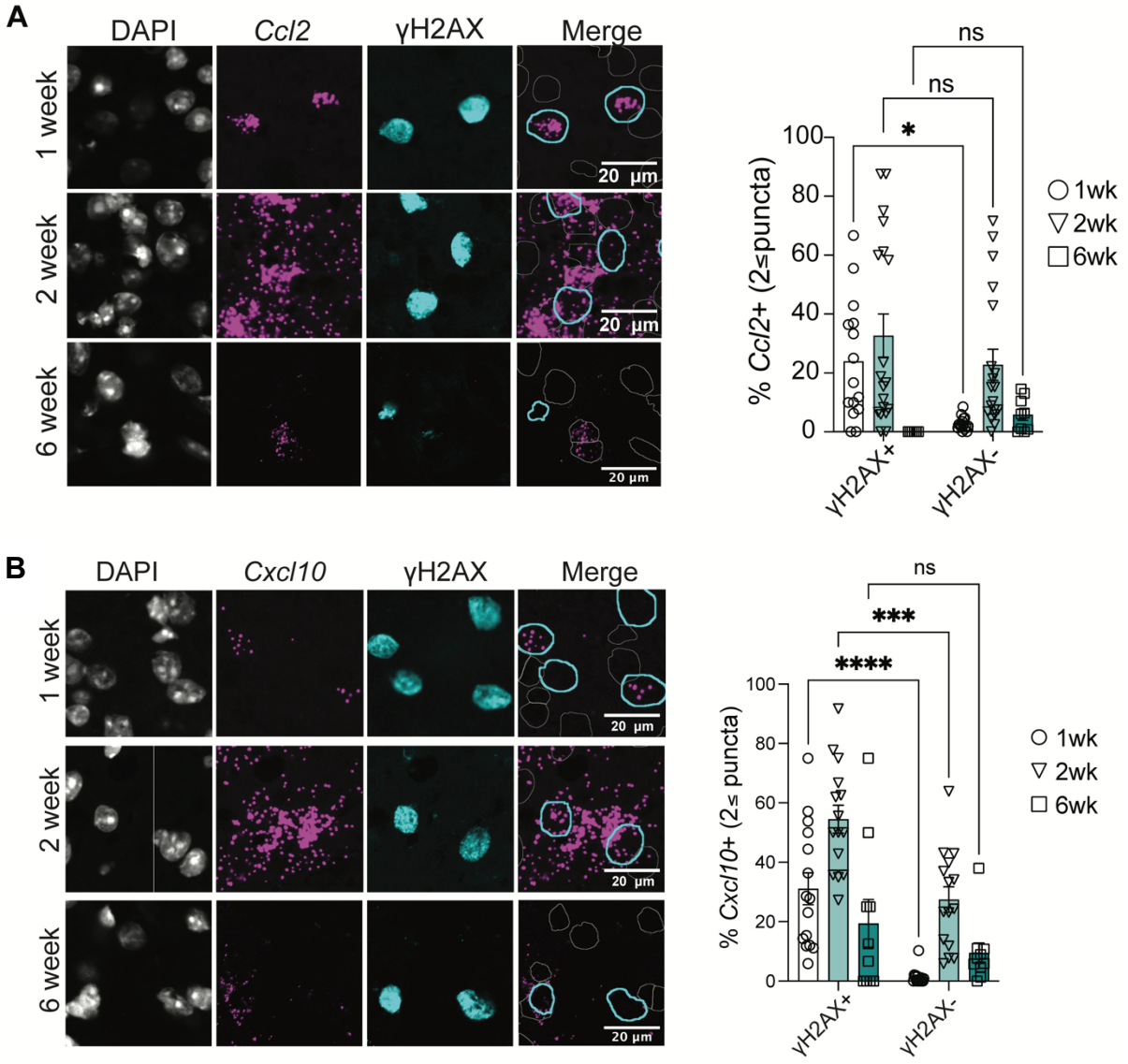

Figure 2-11 γH2AX+ cells express *Ccl2* and *Cxcl10* first. (**A**) (left): Representative images of Ccl2 RNAscope combined with γH2AX immunofluorescent staining for 1, 2, and 6-week CK-p25 cortex. (right): Quantification of number of γH2AX+ and γH2AX- cells with 2≤ Ccl2 puncta. Datapoints represent the average percent Ccl2+ cells in one image from one mouse. 4-3 images were taken per mouse. (1-week n=4, 2-week n=5, 6-week n=3). (**B**) (left): Representative images of Cxcl10 (magenta) combined with γH2AX immunostaining (turquoise). Imaging was performed for 1, 2, and 6-week CK-p25 cortices. (below): Quantification of number γH2AX+ and γH2AX- cells with 2≤ Cxcl10 puncta. Each data point represents the average % Cxcl10+ cells in one image from one mouse. 4-3 images were taken per mouse. (CK-p25 1-week n=4, CK-p25 2-week n=4, CK-p25 6-week n=3). Error bars represent standard error of mean (S.E.M.); ****P<0.0001, ***P<0.001, n.s. not significant; Two-way ANOVA followed by Sidak's test for multiple comparisons. Data are representative of two independent experiments.

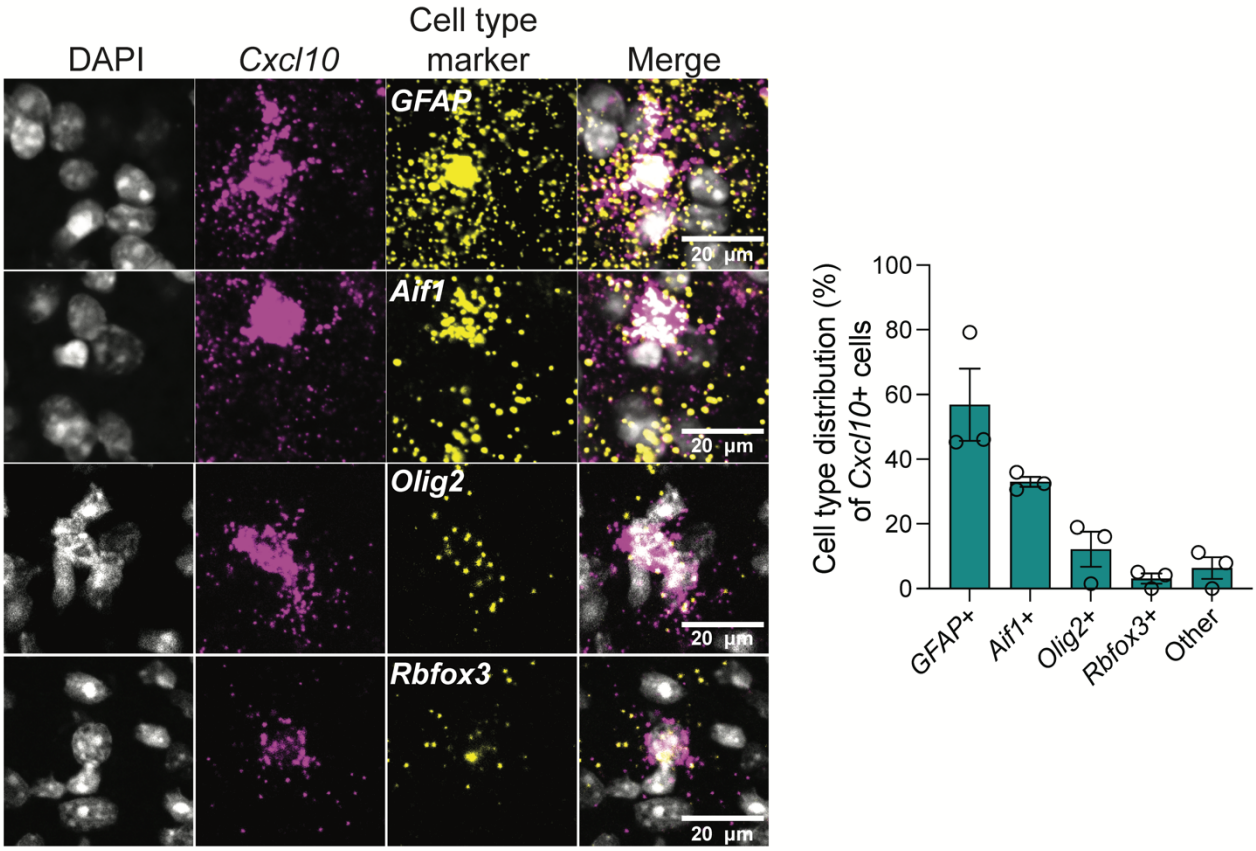

Figure 2-12 Astrocytes and microglia express *Cxcl10* at the two week time point. (above): Representative images of RNAscope probes for astrocytes (*GFAP*), microglia (*Aif1*), oligodendrocytes (*Olig2*), neurons (*Rbfox3*), and *Cxcl10*. (below): Quantification of *Cxcl10*+ nuclei that were *GFAP*+, *Aif1*+, *Olig2*+, *Rbfox3*+, or other. Each data point represents the average percent of *Cxcl10*+ nuclei that were also positive for a given cell type marker for one CK-p25 mouse.

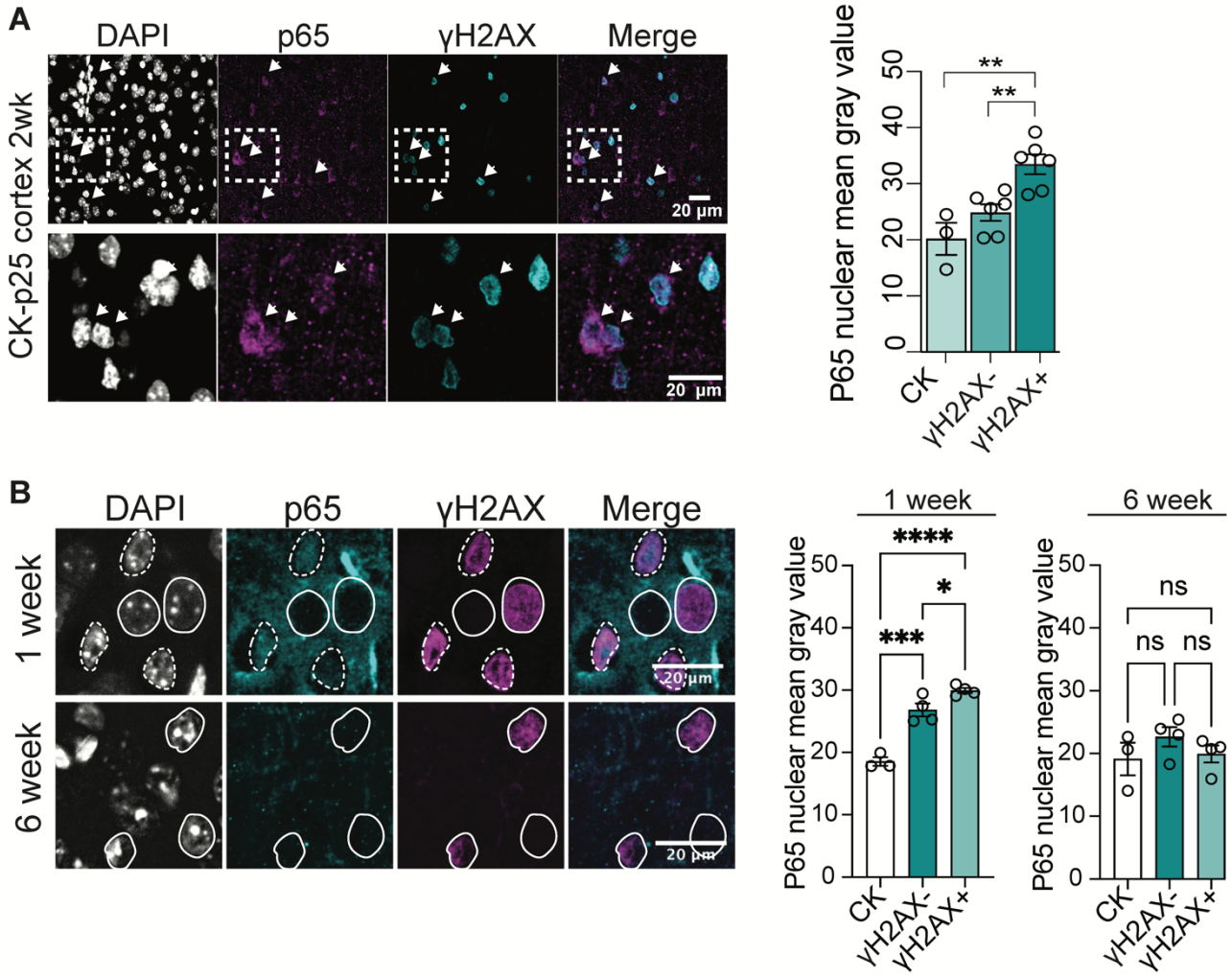

Figure 2-13 γH2AX+ cells have increased nuclear p65. (**A**) (left): Representative image of p65 immunostaining in 2-week CK-p25. (right): Quantification of p65 mean intensity for γH2AX+ and γH2AX- nuclei. Data points represent the average p65 nuclear mean gray value of 20-60 nuclei from one mouse. (**B**) (left): Representative images of p65 immunostaining in CK-p25 cortex at- w1eek and 2-week time points. (right): Quantification of p65 mean intensity for γH2AX+ and γH2AX- nuclei. Each data point represents the average p65 nuclear mean gray value of 20-60 nuclei from one mouse. The white dashed lines indicate γH2AX+ nuclei with nuclear expression of p65. The solid white lines indicate both γH2AX+ and γH2AX- nuclei with little nuclear p65. ****P<0.0001, ***P<0.001, **P<0.01, *P<0.05, n.s. not significant; One-way ANOVA with Tukey's test for multiple comparisons.

however, the total population of γH2AX^{hi} neurons was approximately 50% Stage 1 and 50% Stage 2 (Figure 2-14). This suggested that the Stage 2 population may develop after Stage 1, which aligned with our initial prediction when defining these distinct cellular states based on NeuN expression. To better understand the relationship between Stage 1 and Stage 2 neurons, we performed single nucleus RNA-sequencing on each FANS-gated population at both one and two-week timepoints (Figure 2-7.B). A total of 1,357 single nucleus libraries were prepared using SMARTseq2 chemistry. Following quality control measures (see Methods), 889 libraries remained for downstream analysis (Figures 2-15, 2-16). Cells were classified into major cell type clusters based on marker gene expression, resulting in the identification of 521 excitatory neurons, 71 inhibitory neurons, 131 oligodendrocytes, 33 oligodendrocyte precursor cells (OPCs), and 50 microglia. We did not detect any astrocytes.

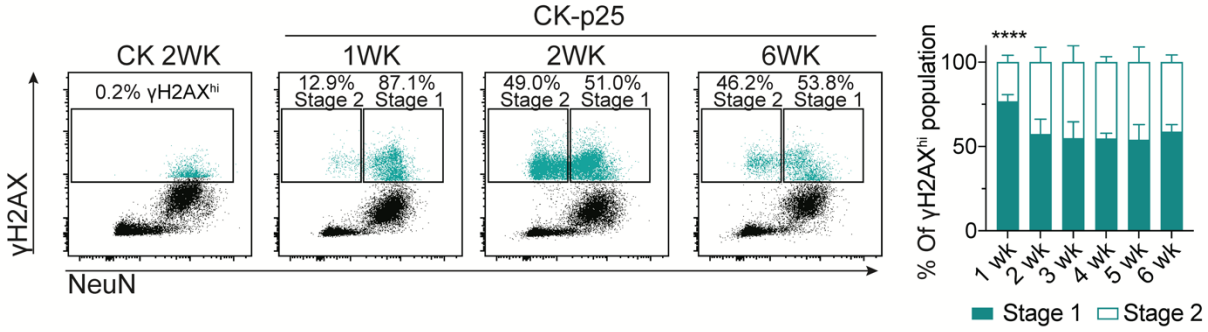

Figure 2-14 Analysis of Stage 1 and Stage 2 populations by time point. (left): Representative dot plots of γH2AX and NeuN immunoreactivity in CK and CK-p25 mice at 1, 2, and 6-week time points. Stage 1 and Stage 2 percent population was calculated with respect to the total γH2AXhi population. (right): Stage 1 and Stage 2 percent population quantified for each time point. Error bars represent standard error of mean (S.E.M.); ****P<0.0001.). Two-way ANOVA followed by Sidak's test for multiple comparisons. Data are pooled from four independent experiments.

Remarkably, the majority of nuclei sorted under the Stage 2 gate formed their own cell type cluster (Figure 2-15), accounting for the remaining 83 cells. While we did identify 13 Stage 2-gated nuclei in microglia and oligodendrocyte clusters, all of the nuclei in question came from one CK-p25 mouse (Figure 2-17). None of the other five CK-p25 mice had Stage 2-gated nuclei fall into glial clusters. Combined with our previous cell type immunostaining analysis (Figure 2-3), we concluded that the immune

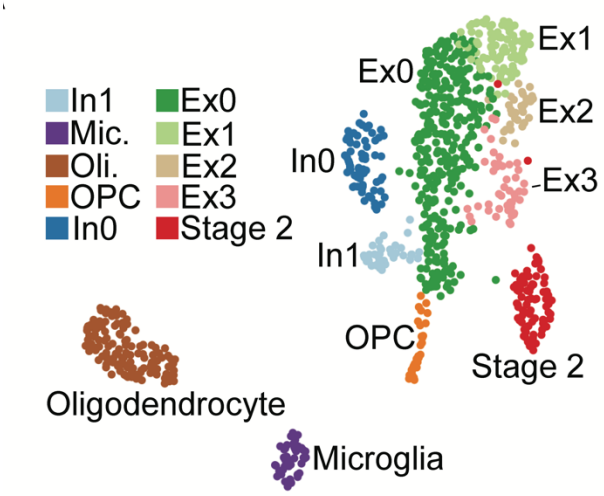

Figure 2-15 Single nucleus RNA-seq of Stage 1&2 neurons. UMAP of gated populations from CK and CK-p25 cortex at 1-week and 2-week timepoints.

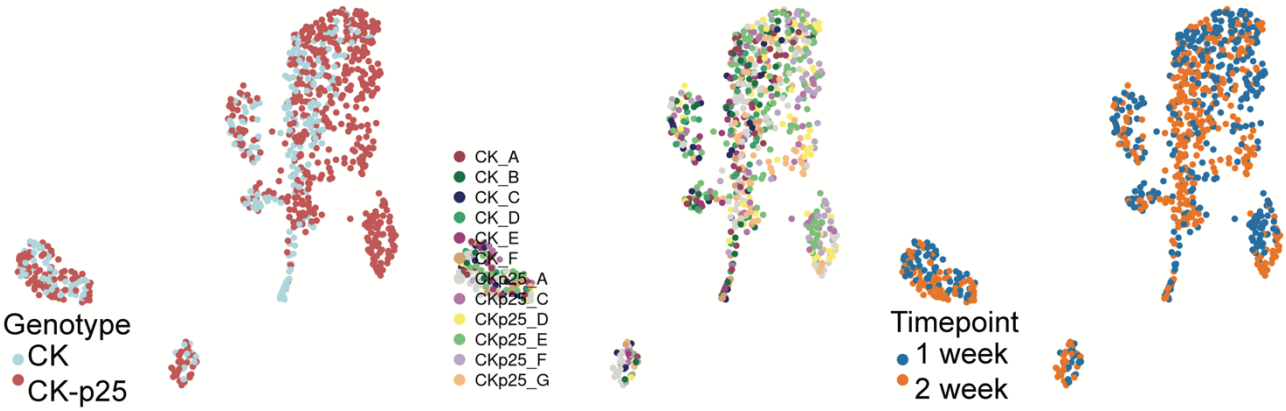

Figure 2-16 UMAPs labeled by genotype, mouse ID, and time point.

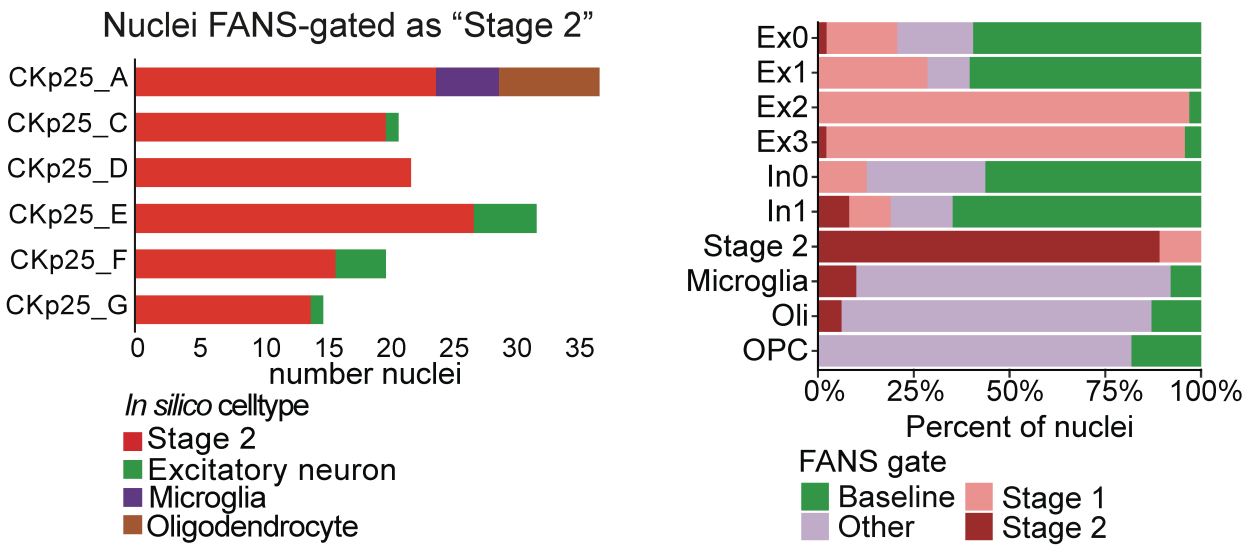

Figure 2-17 Single nuclei distribution by FANSs gate and *in silico* cell type. (left): Distribution of Stage 2-gated nuclei in in silico cell type clusters, stratified by biological replicate. (right): Percent FANS label distribution across snRNA-seq cell type clusters. Bar graph colors refer to FANS gate label.

signature identified in the Stage 2 population was not likely to be driven by contamination from microglia or oligodendrocytes. Compared to other neuronal clusters, the *in silico* Stage 2 cluster was significantly enriched for the FANS-gated Stage 1 and Stage 2 gene signatures (Figure 2-18). Interestingly, the Stage 2 cluster expressed only moderate levels of the excitatory neuron cluster markers *Camk2a*, *Gria1*, and *Syt2*, and lacked marker genes of other canonical cell types such as inhibitory neurons (*Gad1*, *Gad2*), astrocytes (*GFAP*), microglia (*Cd33*, *Csf1r*), oligodendrocytes (*Plp1*, *Mbp*), and OPCs (*Bcan*). Instead, the Stage 2 cluster expressed marker genes indicative of senescence, including *Cdkn1a,* and *Ubb* (Figure 2-19). These distinctive cell type markers further suggested to us that the Stage 2 cluster represented a population of DSB-bearing neurons engaged in a senescence-like inflammatory response.

To further examine Stage 1 and Stage 2 cell type heterogeneity, we subclustered all neuronal cells. This resulted in the identification of four excitatory neuron subclusters (Ex0-3), and two inhibitory neuron subclusters (In0, In1) (Figure 2-15). Stage 1 cells were enriched in subclusters Ex2 and Ex3 compared to

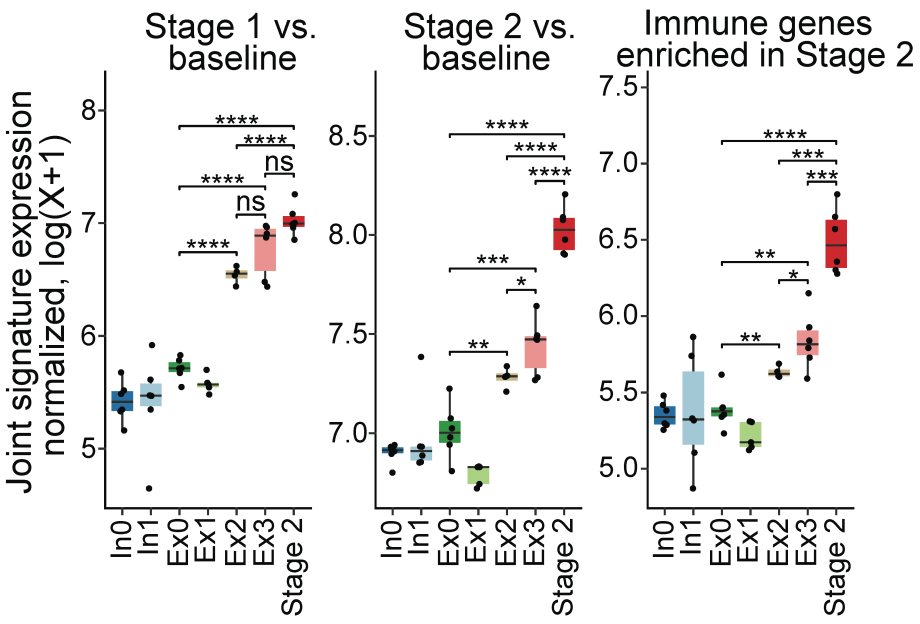

Figure 2-18 Bulk RNA-seq gene signature enrichment in neuron cell type clusters. Stage 1 signature enrichment (left), Stage 2 signature enrichment (middle), and immune genes from Stage 2 enrichment (right). Each datapoint indicates average gene expression across all nuclei from one mouse. Only CK-p25 mice were used for this analysis. ****P<0.0001, ***P<0.001, **P<0.01, *P<0.05, n.s. not significant; One-way ANOVA with Tukey's test for multiple comparisons.

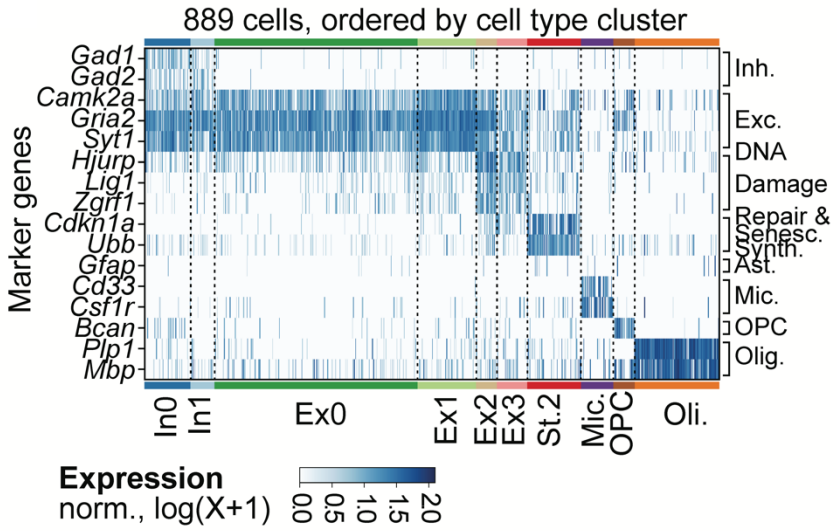

Figure 2-19 Marker gene expression for each cell type cluster. Columns represent 889 individual cells ordered by cell type cluster.

Ex0 and Ex1 (Figure 2-17). In addition to excitatory neuron markers, subclusters Ex2 and Ex3 were also marked by genes associated with DNA repair and DNA synthesis, such as Holliday junction–recognizing protein (*Hjurp)*, the helicase *Zgrf1,* and Ligase I (*Lig1)*. Both *Hjurp* and *Zgrf1* are involved in homologous recombination, a form of DSB repair that requires entry into S-phase of the cell cycle (Figure 2-19). Expression of these genes by postmitotic neurons may reflect erroneous cell-cycle reentry in an effort to repair DSBs (204). *LigI* is involved in both DNA replication and numerous DNA repair pathways, including alternative end-joining of DSBs. These genes indicate Ex2 and Ex3 cells were likely engaged in a DSB repair response and cell cycle re-entry (Figure 2-19).

Interestingly, *Hjurp*, *Zgrf1*, and *LigI* were not expressed in the Stage 2 cluster. Combined with the enrichment for the classical senescence marker *Cdkn1a*, and the fact that these cells are still γH2AX^{hi}, we hypothesized that Stage 2 cells may be engaged in an even later stage of response to DSBs. This motivated us to perform trajectory analysis. The single cell analysis package Monocle 3 (205) was used to order cells from subclusters Ex0, 1, 2, 3 and Stage 2 along a pseudotime, which was generated through a learned trajectory of subcluster gene expression differences (Figure 2-20). Both CK and CK-p25 cells were used

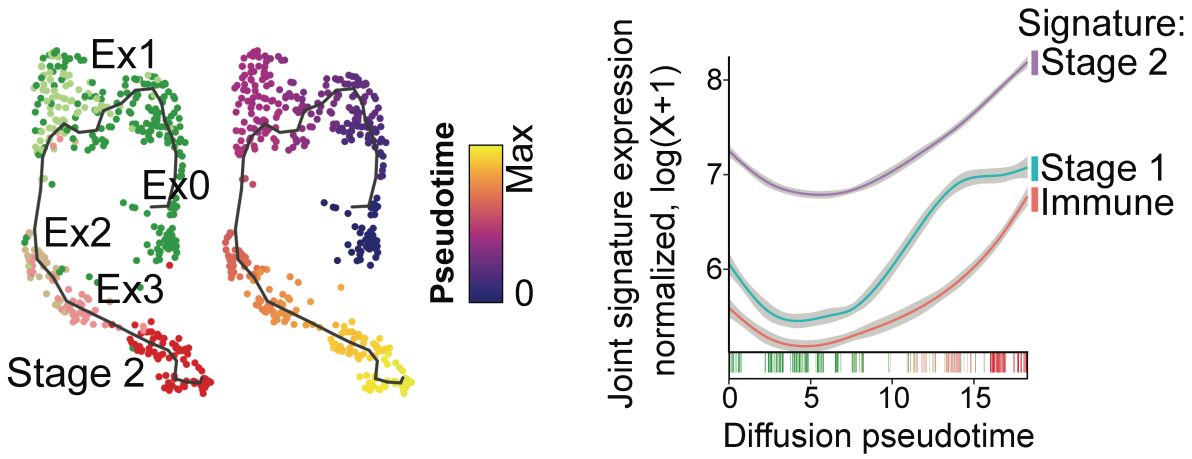

Figure 2-20 Trajectory analysis of Ex0, 1, 2, 3, and Stage 2 neurons. Smoothened gene signature expression across pseudotime. Stage 1= Stage 1 gene signature. Stage 2= Stage 2 gene signature. Immune= Genes belonging to immune gene ontologies from Stage 2 gene signature. padj<0.05, $\log_2$ fold-change ≥1.0.

for this analysis. Next, we identified genes that changed as a function of pseudotime. We observed sequential enrichment of Stage 1 and Stage 2 gene signatures along pseudotime (Figure 2-20). The expression of Stage 2 signature genes specifically involved in immune response (Immune) were also enriched at the end of pseudotime (Figure 2-20). We found that genes associated with neuronal identity such as *Gria2* and *Kalrn* were most highly expressed at the beginning of the trajectory (Figure 2-21). Meanwhile, genes associated with DSB repair and DNA synthesis like *Hjurp* and *Lig1* peaked along the middle, and *Cdkn1a* expression peaked at the end of the trajectory. We also observed late-stage expression of *Apoe*, supporting previous observations that *Apoe* expression increases in neurons following injury (206). While expression of the gene encoding NeuN (*Rbfox3*) increased significantly in Ex1 compared to Ex0, we did not observe a significant difference in expression between Ex0 and Stage 2 (Figure 2-22). This indicates that reduction of NeuN in Stage 2 neurons likely occurs at the post-transcriptional level, and agrees with previous observations that reduced NeuN antigenicity or protein levels are observed in damaged neurons (193,195). We also observed a significant increase in *Rela* expression in Ex1 and Ex2 neurons compared to Ex0, but we did not observe a significant difference in expression between Ex0 and Stage 2 (Figure 2-22).

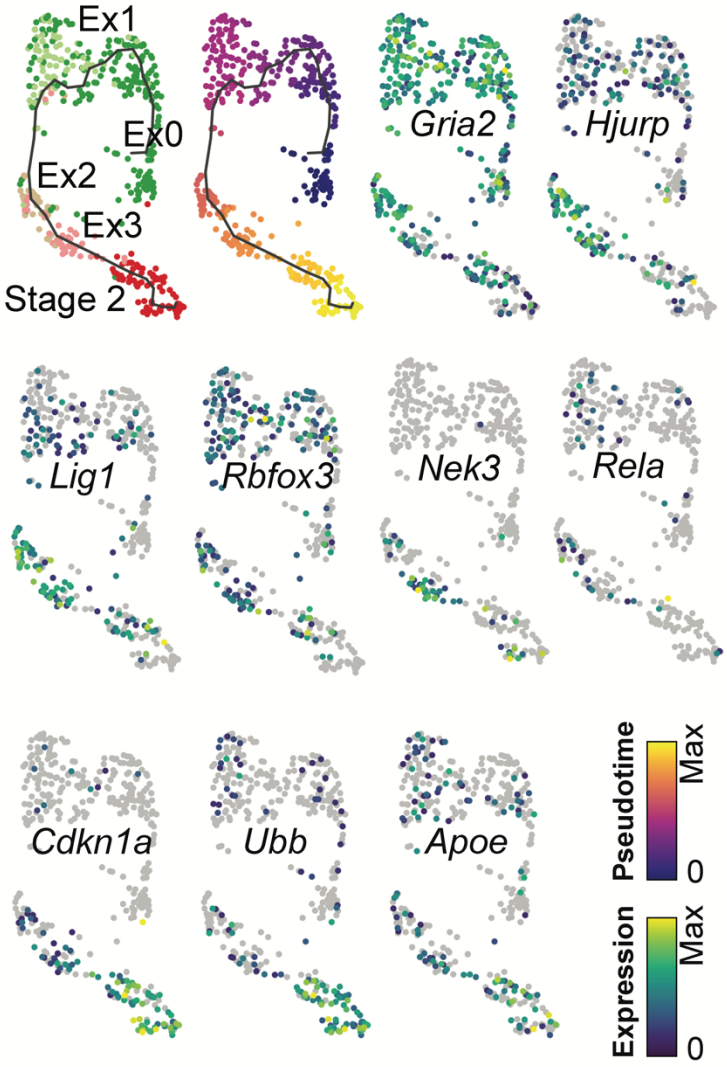

Figure 2-21 Gene expression across Ex0, 1, 2, 3, and Stage 2 neurons. Cells from each cluster are ordered across pseudotime. Individual genes are mapped across pseudotime.

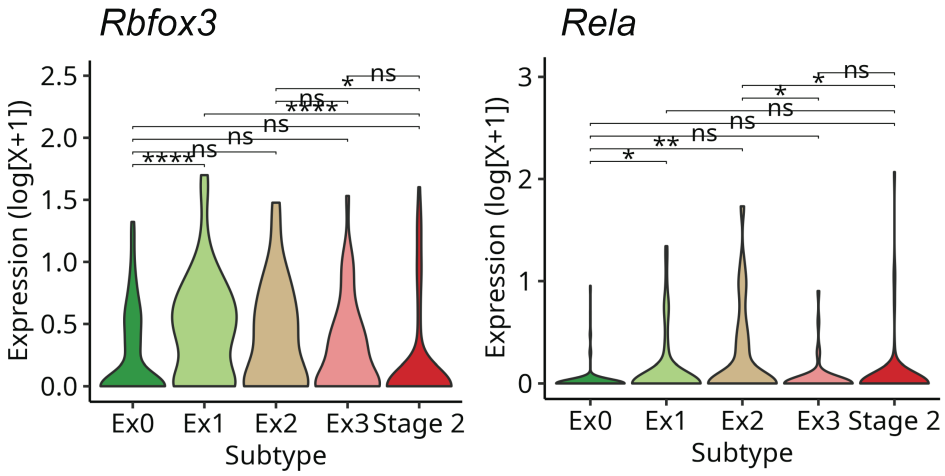

Figure 2-22 Quantification of Rela and Rbfox3 gene expression for neuron cell type clusters. ****P<0.0001, ***P<0.001, **P<0.01, *P<0.05, n.s. not significant; One-way ANOVA with Tukey's test for multiple comparisons.

2.2.4 DSBs elicit innate immune signaling in neurons

We next wanted to determine if the gene signatures identified in CK-p25 mice could be recapitulated independent of p25 expression. We also wanted to test if DSBs induction is sufficient to trigger inflammatory gene expression in neurons. To accomplish this, we first treated murine primary neuron cultures with etoposide (ETP). ETP produces DSBs by inhibiting topoisomerase-II function, thus preventing the re-ligation of cleaved DNA-TopII complexes (Figure 2-23). The dose of ETP used was consistent with previous studies using ETP to investigate DSB-elicited immune activity (153,207). Neuron cell type purity was also confirmed in primary neuronal cultures (See Methods, Figure 2-24).

RNA-sequencing was performed to profile the transcriptional changes occurring in primary neurons after ETP treatment (Figure 2-25.A). There was a significant upregulation of 7,532 transcripts and downregulation of 7,106 transcripts compared to vehicle-treated control neurons (DMSO) (adjusted p-value<0.05) (Figure 2-26). Notably, GSEA revealed that biological pathways mediating senescent and antiviral activity such as 'Interferon alpha response,' and 'Il6 jak stat3 signaling,' were enriched in ET

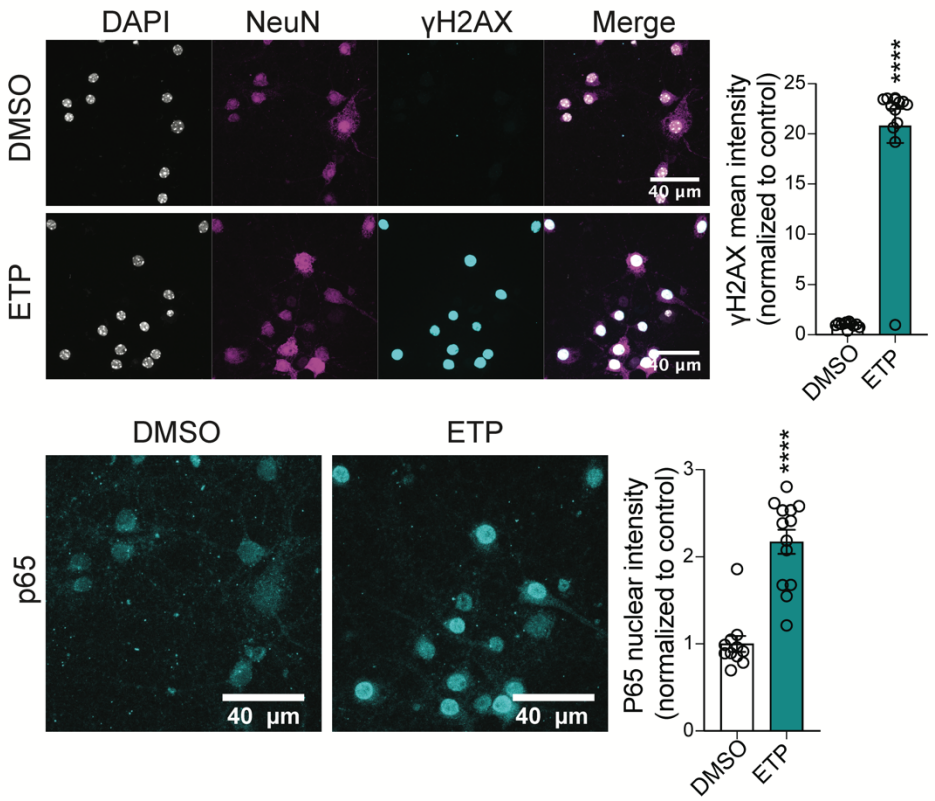

Figure 2-23 p65 localizes to the nucleus of etoposide-treated primary neurons. (top): Representative images of NeuN and γH2AX immunostaining in ETP and vehicle-treated primary cultures. Each data point represents γH2AX mean gray value for one nucleus. (bottom): Representative images of p65 immunostaining in ETP and vehicle-treated primary cultures. Each data point represents p65 mean gray value for one nucleus. Error bars represent standard error of mean (S.E.M.); ****P<0.0001, ***P<0.001. Student's T-test. Data are representative of 3 independent experiments.

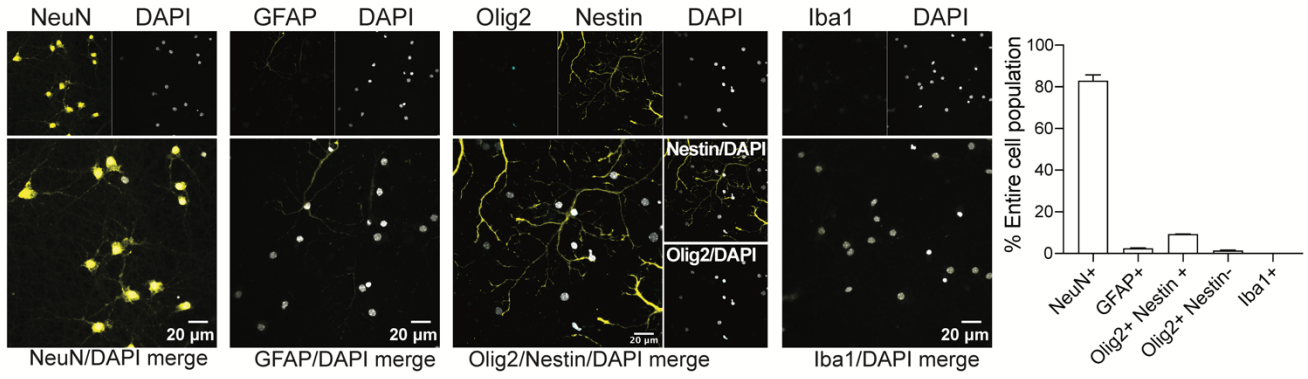

Figure 2-24 Cell type analysis of primary neuron cultures. Representative images of cell type immunostaining in DIV13 primary neuron cultures. The percent nuclei that stained positively for each cell type marker are quantified on the right. Three images were analyzed for each cell type marker. Data are representative of two independent experiments.

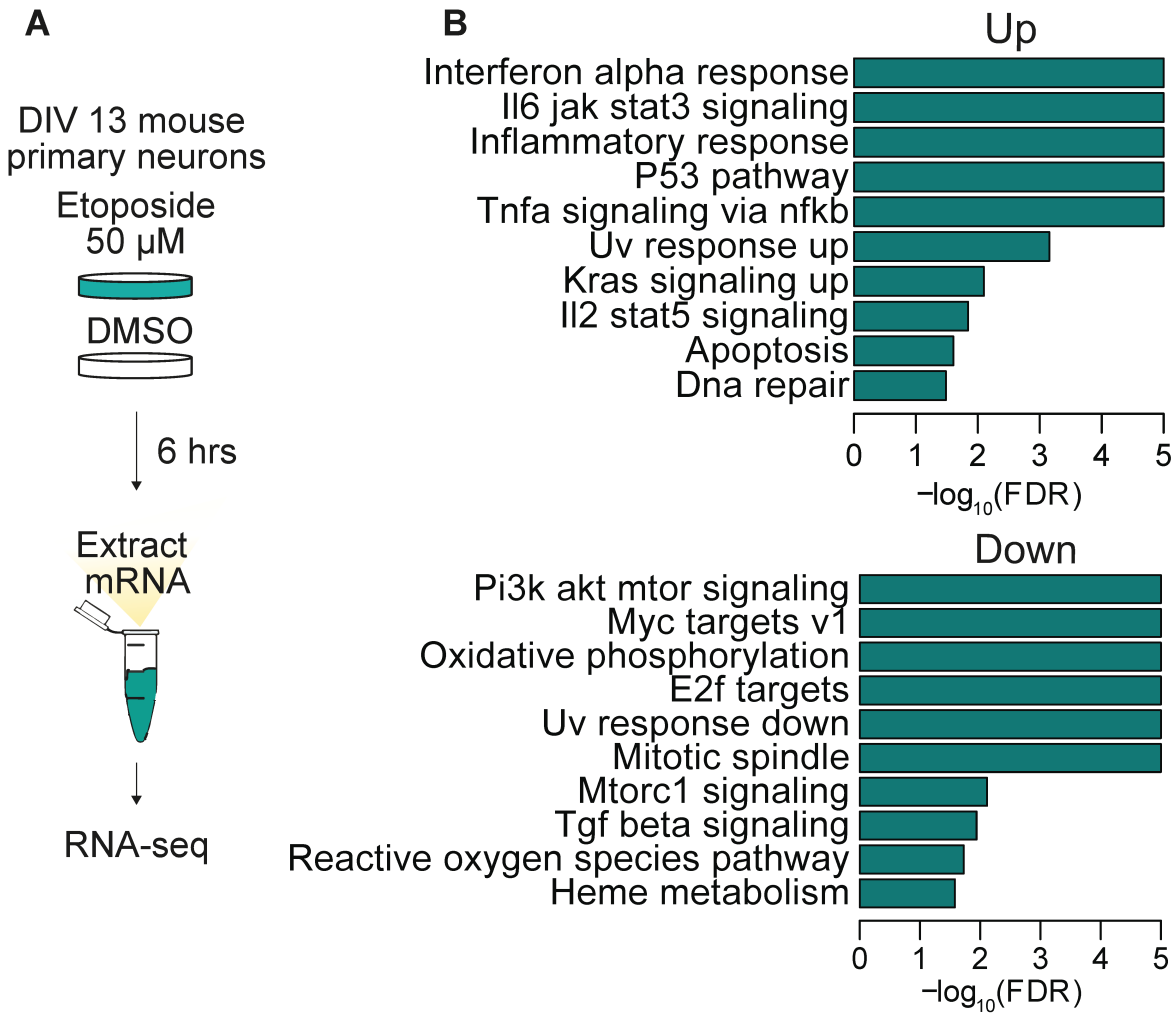

Figure 2-25 Etoposide-treated primary neurons upregulate inflammatory processes. (**A**) Schematic of etoposide (ETP) treatment. DIV13 neuron primary cultures were treated with either 50µM ETP or vehicle control (DMSO) for 6 hours. (**B**) Differential gene ontology terms identified through GSEA from ETP vs. DMSO contrast.

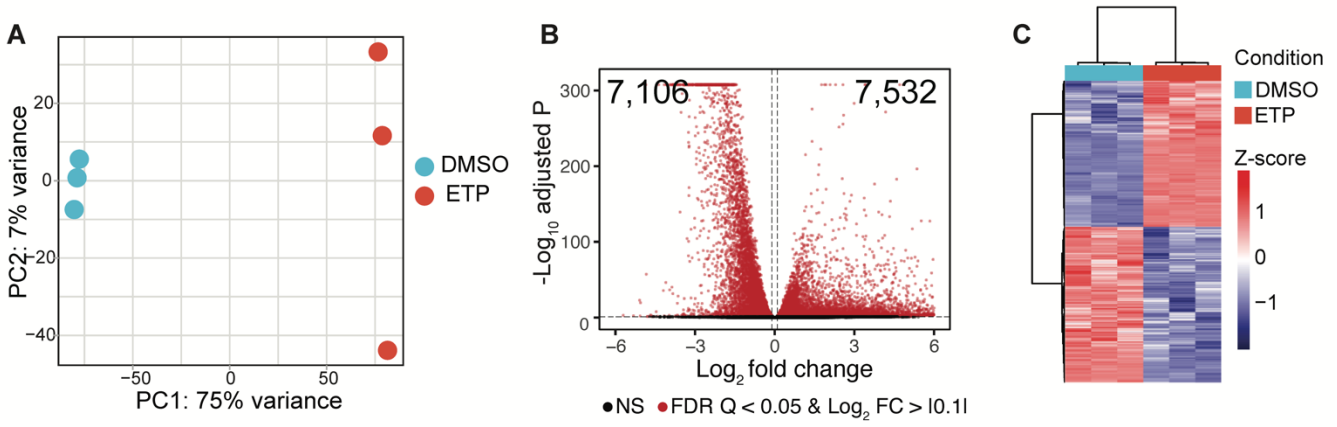

Figure 2-26 Differential analysis of ETP-treated primary neurons. (**A**) PCA plot of normalized gene expression matrix from ETP and DMSO-treated primary neurons. Principle component 1 (PC1): 75% variance. Principle component 2 (PC2): 7% variance. (**B**) Volcano plot of ETP vs. DMSO contrast. Gray circles: non-significant (ns) transcripts. Red circles: transcripts with FDR adjusted p-value <0.05 and log2 fold change >|0.1|. Number of significantly upregulated and downregulated transcripts are shown in the upper right and left corners respectively. (**C**) Heatmap of differentially expressed genes from ETP vs. DMSO contrast. Columns represent biological replicates.

treated cultures (Figure 2-25.B). Furthermore, many of the cytokines upregulated in Stage 2 neurons were also upregulated in ETP-treated neurons, including *Ccl2*, *Cxcl10*, *Cxcl16*, and *Il6* (Table A2). Stage 1 and Stage 2 gene signatures were both significantly enriched in differentially expressed genes from ETP-treated neurons (p=0.00064 & p=0.0081 respectively) (Figure 2-27.A). Venn-diagram analysis indicated that 12.29% of all protein-coding DEGs (total protein-coding DEGs from all datasets) were shared between ETP, Stage 1 and Stage 2 conditions (Figure 2-27.B). This overlap was enriched for DNA damage repair genes such as *Parp10*, *Tdp2*, *Fanca*, and *Rad54l*. A further 12.86% of all DEGs were shared between ETP and Stage 2 conditions. This overlap was enriched for immune genes such as *Rela*, *Nfkbia*, and *Irf1* (Figure 2-27.B). p65 nuclear intensity was also significantly increased in ETP-treated neurons (Figure 2-23). We also used X-ray irradiation as an independent method to induce DSBs. Exposing primary neuronal cultures to 10 Gy irradiation was also able to increase nuclear p65 intensity in neurons, as was treatment with a lower dose of ETP (25μM) (Figure 2-28.A, B). Furthermore, both X-ray irradiation and 25μM ETP significantly increased many of the genes shared by the higher dose ETP treatment and

Stage 1 or Stage 2 (Figure 2-28.C). Together, these data indicated that Stage 1 and Stage 2 gene signatures can be recapitulated in primary neuron cultures independent of p25 expression.

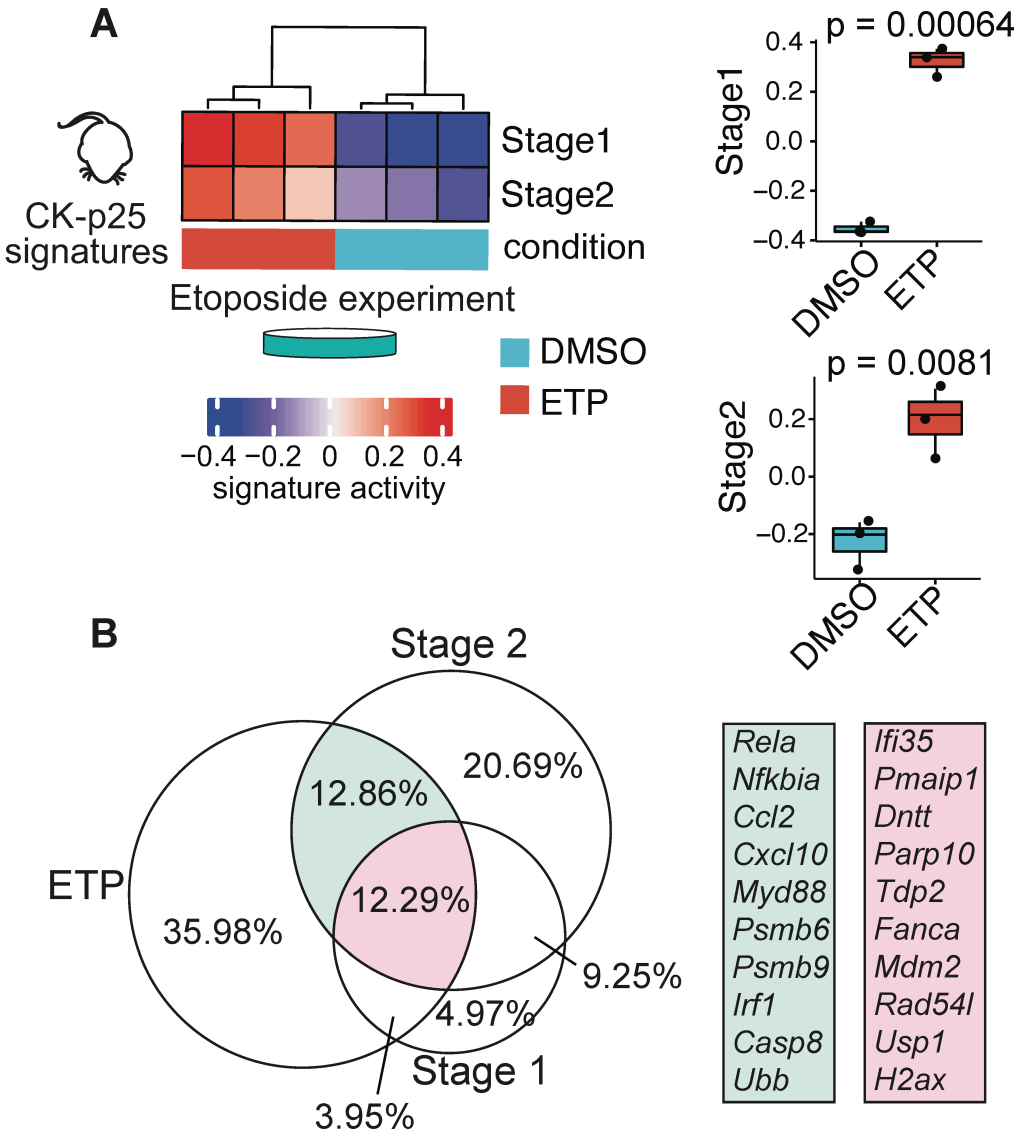

Figure 2-27 Etoposide-induced gene expression is enriched for Stage 1&2 signature genes. (**A**) (left): Heatmap of Stage 1 and Stage 2 signature enrichment in DMSO and ETP-treated neurons. (right): Quantification of Stage 1 and Stage 2 signature enrichment in DMSO and ETP-treated neurons. Each data point represents one biological replicate. (**B**) Venn diagram of significantly upregulated protein-coding genes from ETP-treated neurons and Stage 1 and Stage 2 gene signatures. Percentages are in reference to the total number of unique genes from all three gene sets. Genes overlapping in ETP and Stage 2 are in turquoise. Genes overlapping in ETP, Stage 2, and Stage 1 are in magenta. The area of the circles are in proportion to the size of the gene sets. Error bars represent standard error of mean (S.E.M.); ****P<0.0001, ***P<0.001. Wilcoxon test (A).

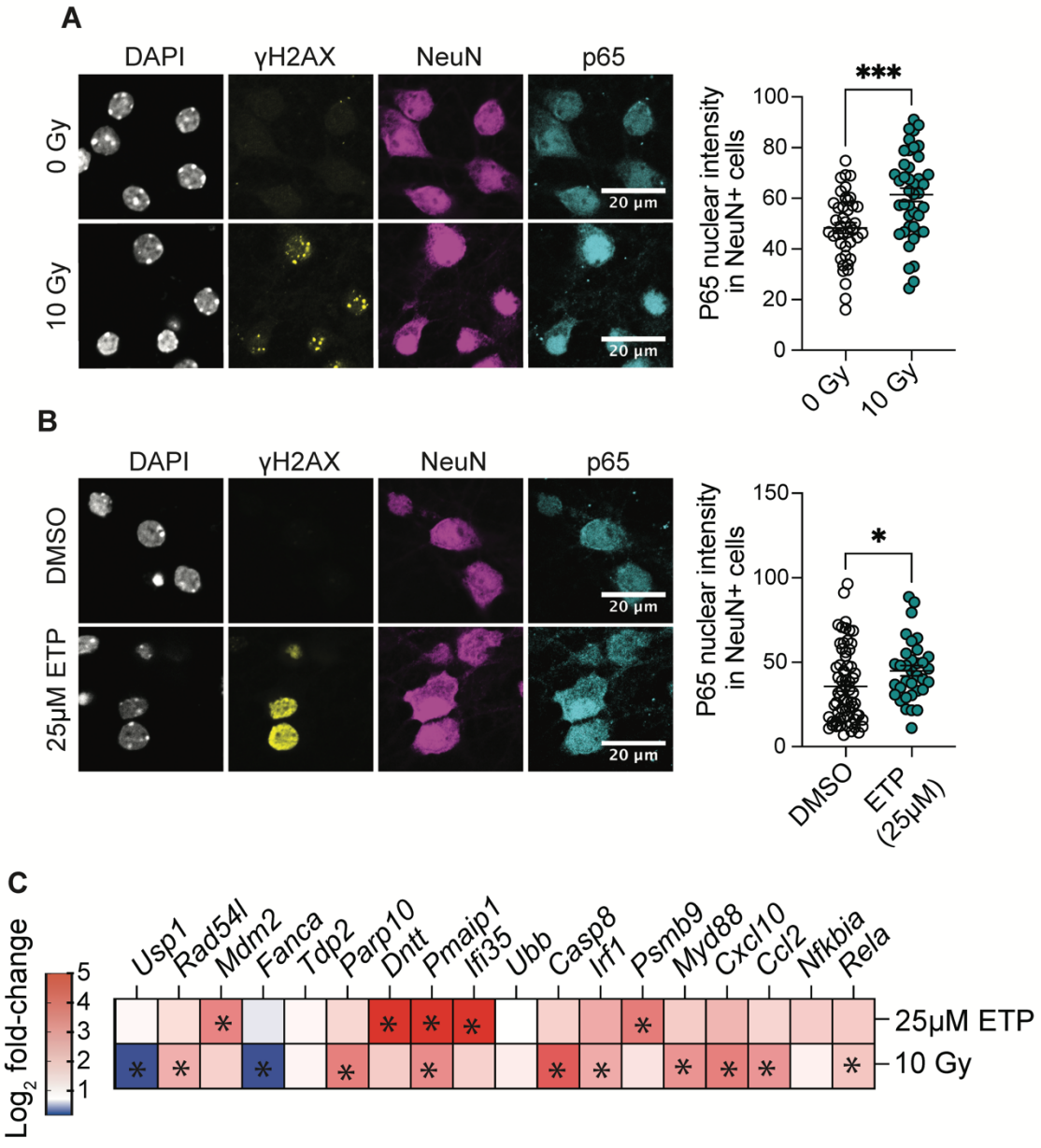

Figure 2-28 X-ray irradiation and a lower dose of etoposide also induces inflammatory gene expression in primary neurons. (A, B) Representative images of p65 immunostaining from 10 Gy and 0 Gy X-ray (A), and 25μM ETP treated primary neurons (B). Each data point represents the p65 mean gray value for one nucleus. (0 Gy n=42, 10 Gy n=42, DMSO n=65, 25μM ETP n=34) **(C)** RT-qPCR of upregulated genes shared between 50μM ETP, Stage 1, and Stage 2 neurons in X-ray and 25μM ETP-treated primary neurons. The average of 3 replicates are represented in the heatmap. Log2 fold change is shown for each condition relative to a control (0 Gy and DMSO primary neurons respectively). Significantly upregulated genes are indicated with an asterisk. Error bars represent standard error of mean (S.E.M.); ***P<0.001, *P<0.05. Student's T-test. Data are representative of two independent experiments (A, B).

2.2.5 A DSB-associated immune signature is conserved in AD human neurons

We next sought to determine if signatures of DSB-bearing neurons could also be detected in the human brain. First, we used the Stage 2 gene signature to identify neurons with DSB-associated immune activation in a previously published snRNA-seq dataset of individuals with and without AD pathology (Figure 2-29.A)(208). We assessed Stage 2 gene expression in all major brain cell types: excitatory neurons, inhibitory neurons, astrocytes, oligodendrocytes, oligodendrocyte precursor cells, and microglia. For each cell type, genes were ranked based on their expression and correlation to 'global pathology,' a variable quantifying three major AD pathologies: neuritic plaques, diffuse plaques, and neurofibrillary tangles (209). Genes that positively correlated with global pathology for each cell type were then sampled for the enrichment of Stage 2 genes (Figure 2-29.A). The strongest enrichment of Stage 2 genes was identified in excitatory neurons (p=8.7E-19), and inhibitory neurons (p=7.7E-7). Astrocytes and oligodendrocytes were also found to have a significant enrichment of Stage 2 genes correlating with global pathology, albeit to a much lesser extent (Figure 2-29.B), (Bonferroni adjusted p-value < 0.01). Therefore, while we cannot exclude the possibility that human astrocytes and oligodendrocytes may carry some disease-associated enrichment for Stage 2 genes, the Stage 2 signature is largely driven by neurons in this dataset. Furthermore, when assessing the Stage 2 genes positively correlated with global pathology in excitatory neurons, we again observed an enrichment of immune-related biological pathways, including the genes Ccl2-like receptor (*CCRL2*), *CD74*, *CXCL16*, and *APOE* (Figure 2-29.C, D).

To validate the enrichment of DSB-bearing neurons identified in our snRNA-seq analysis, we sorted γH2AX^{hi} and γH2AX^{lo} NeuN^{hi} and NeuN^{lo} nuclei from the postmortem temporal cortex of 6 individuals, and then performed bulk RNA-sequencing (Figures 2-30, 2-31.A-C). These individuals were part of the Massachusetts Alzheimer's Disease Research Center (MADRC) cohort, and were divided by Braak score as either AD (Braak 4-6), or non-AD (Braak 1-3). Age, sex, and other biological variables

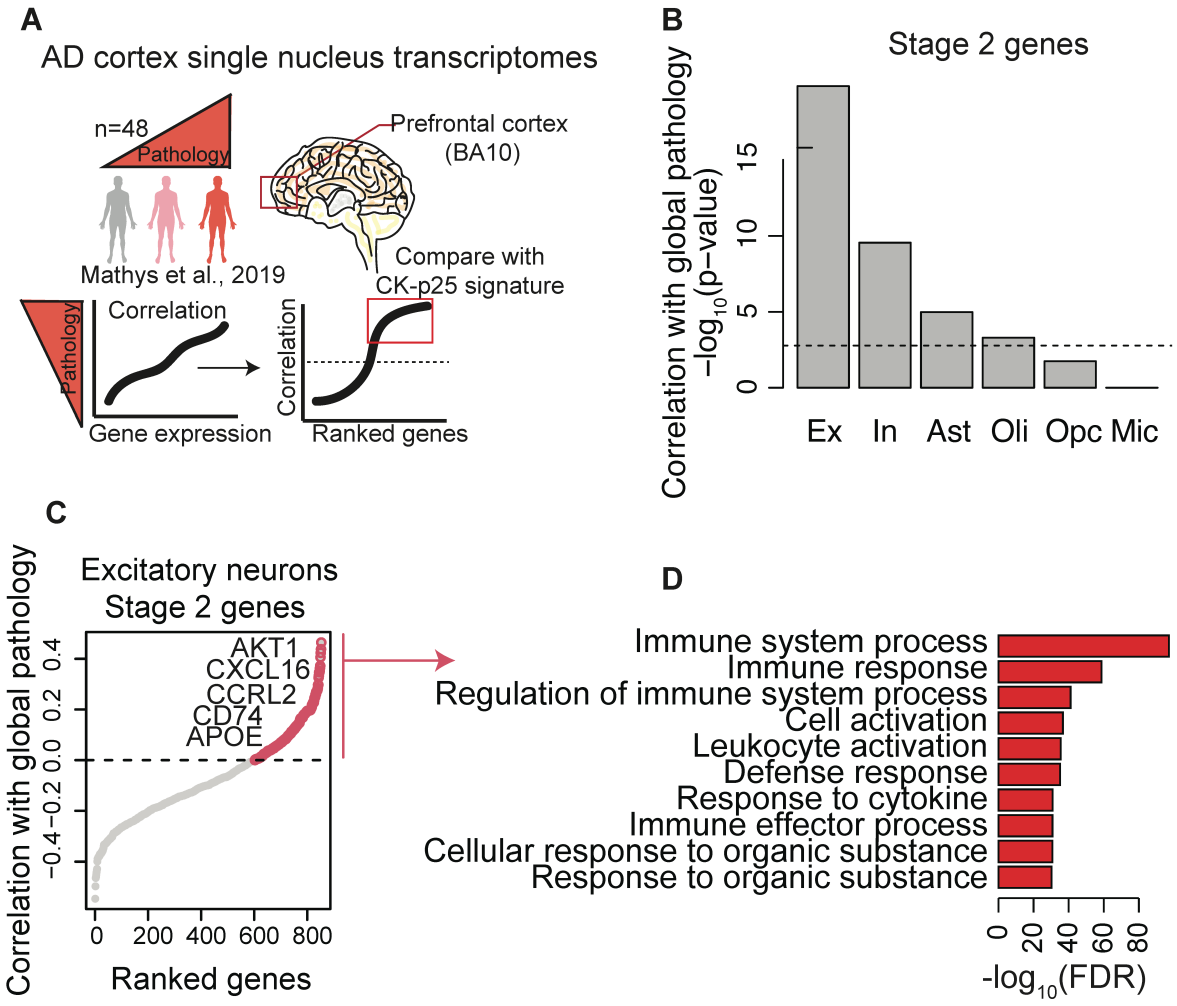

Figure 2-29 Stage 2 gene expression correlates with AD global pathology. (**A**) Schematic of the Stage 2 signature analysis in the AD snRNA-seq dataset (209). (**B**) Quantification of Stage 2 signature correlation with global pathology in cell type clusters (209). Stage 2 genes were tested for significant and positive correlation with the global pathology metric for each major cell type. The -$\log_{10}$ p-value for these tests are shown in the histogram. The dashed line indicates a p-value of 0.01 after Bonferroni correction for multiple testing. Excitatory neurons (Ex), Inhibitory neurons (In), Astrocytes (Ast), Oligodendrocytes (Oli), Oligodendrocyte precursor cells (Opc), Microglia (Mic). (**C**) Stage 2 signature genes ranked by their correlation with global pathology in excitatory neurons. Example Stage 2 genes are shown with red circles. (**D**) Gene ontology of Stage 2 signature genes positively correlated with global pathology.

for each individual are available in Table A3. To assess the cell type specificity of our sorted populations, we examined the expression of several cell type marker genes (Figure 2-31.D-F). Unlike the Stage 2 nuclei from the CK-p25 mice, γH2AX^{hi} NeuN^{lo} nuclei from the human brain were enriched for glial markers (Figure 2-31.E, F). This indicated to us that human glial cells also accumulate DSBs, as has been previously reported (8), and that γH2AX^{hi} nuclei with low NeuN expression are likely to contain a heterogenous population of many different cell types. Thus, to ensure we were analyzing neuronal gene expression, we focused our analysis on γH2AX^{hi} NeuN^{hi} nuclei.

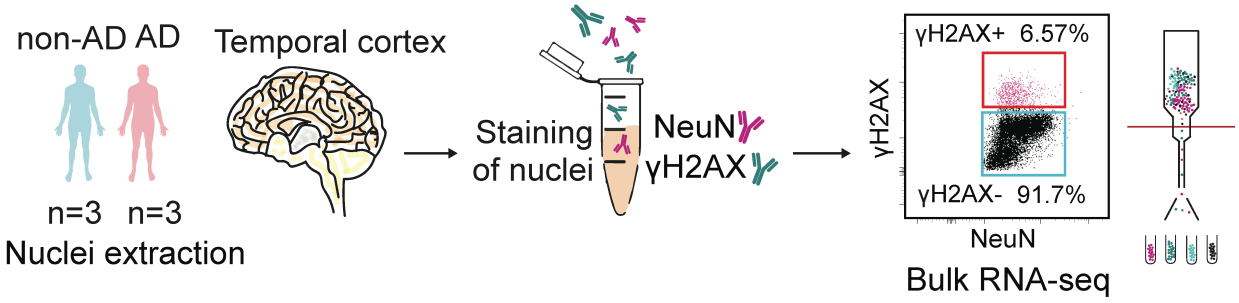

Figure 2-30 Schematic of γH2AX^{hi} nuclei sorting from AD and non-AD brain tissue.

We assessed Stage 1 and Stage 2 gene signature activity in NeuN^{hi} nuclei from the human brain (Figure 2-32.A). γH2AX^{hi} neurons displayed modest enrichment for the CK-p25 Stage 1 and Stage 2 genes (p=0.31 and p=0.04 respectively) (Figure 2-32.B). Comparing samples by AD status and γH2AX status further revealed that Stage 1 and Stage 2 gene activity was markedly enriched in γH2AX^{hi} neurons from AD individuals (p=0.0075 and p=0.0021, respectively) (Figure 2-32.C,D). Furthermore, when contrasting all γH2AX^{hi} neurons against all γH2AX^{lo} neurons, we found that the average $\log_2$ fold change values for both Stage 1 and Stage 2 gene sets were positive and significantly higher than the average $\log_2$ fold change values for all other genes (Figure 2-33.A). We also assessed the transcriptional similarity between human γH2AX^{hi} neurons and ETP-treated primary neurons. Compared to γH2AX^{lo} neurons, we found that gene

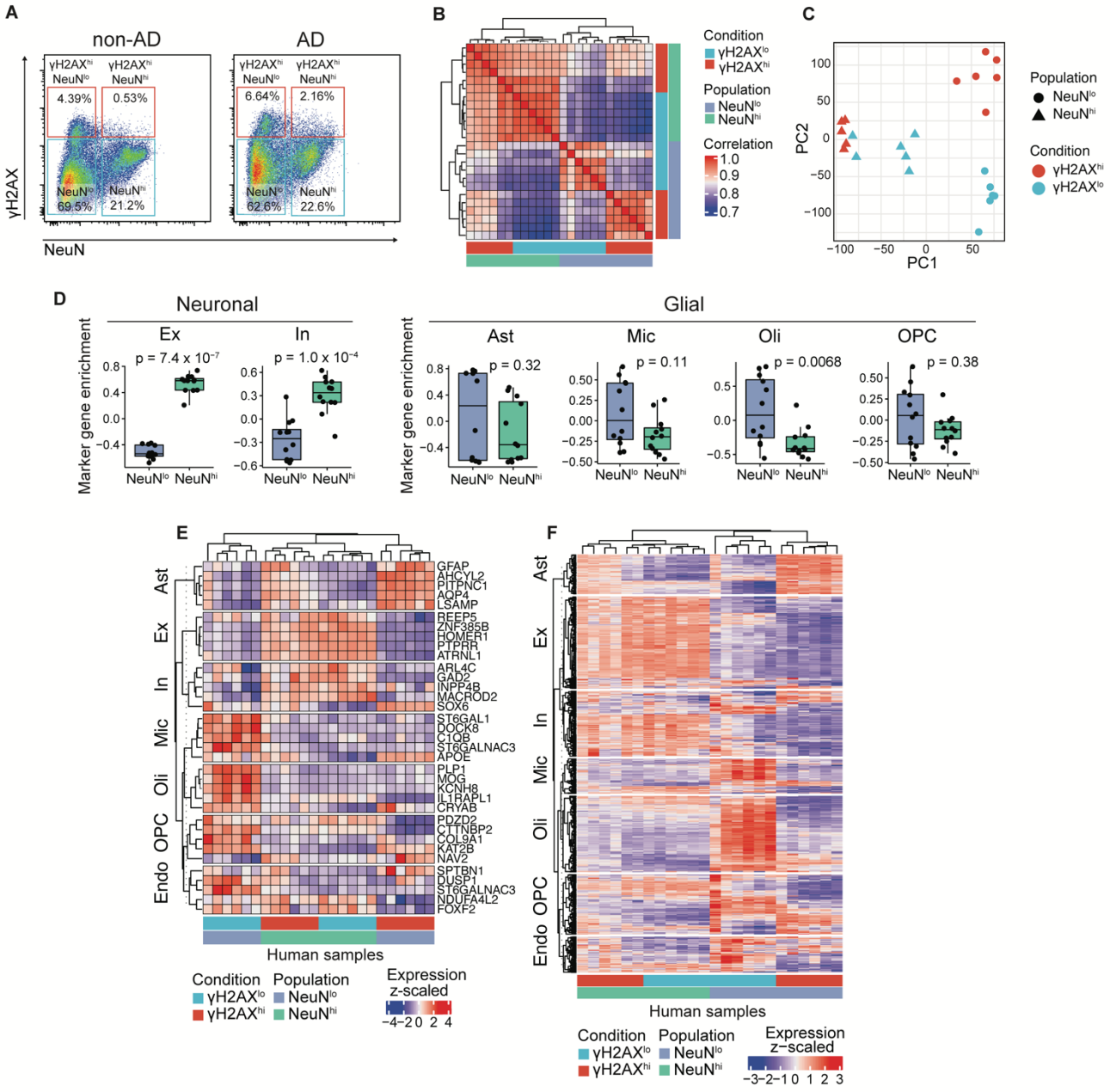

Figure 2-31 Cell type analysis of γH2AX^{hi} nuclei sorted from postmortem human brain. (**A**) Flow cytometry dot plot of γH2AX gating for human NeuN^{hi} and NeuN^{lo} nuclei. Percent total population is indicated for each gating box. (**B**) Correlation heatmap of γH2AX^{hi} and γH2AX^{lo}/NeuN^{hi} and NeuN^{lo} bulk RNA-seq libraries from postmortem temporal cortex. (**C**) PCA plot of normalized gene expression from γH2AX^{hi} and γH2AX^{lo}/NeuN^{hi} and NeuN^{lo} samples. (**D**) Quantification of normalized neuronal and glial marker gene expression in NeuN^{hi} and NeuN^{lo} samples. Mean gene expression is compared with a Wilcoxon test. Gene set enrichment was calculated using Gene Set Variation Analysis (GSVA). (**E**) Gene expression heatmap of top five marker genes for major brain cell types. Each column represents one human sample. (**F**) Gene expression heatmap of all marker genes for major brain cell types. Each column represents one human sample. Excitatory (Ex), Inhibitory (In), Astrocyte (Ast), Microglia (Mic), Oligodendrocyte (Oli), Oligodendrocyte Precursor Cells (OPC), Endothelial (Endo).

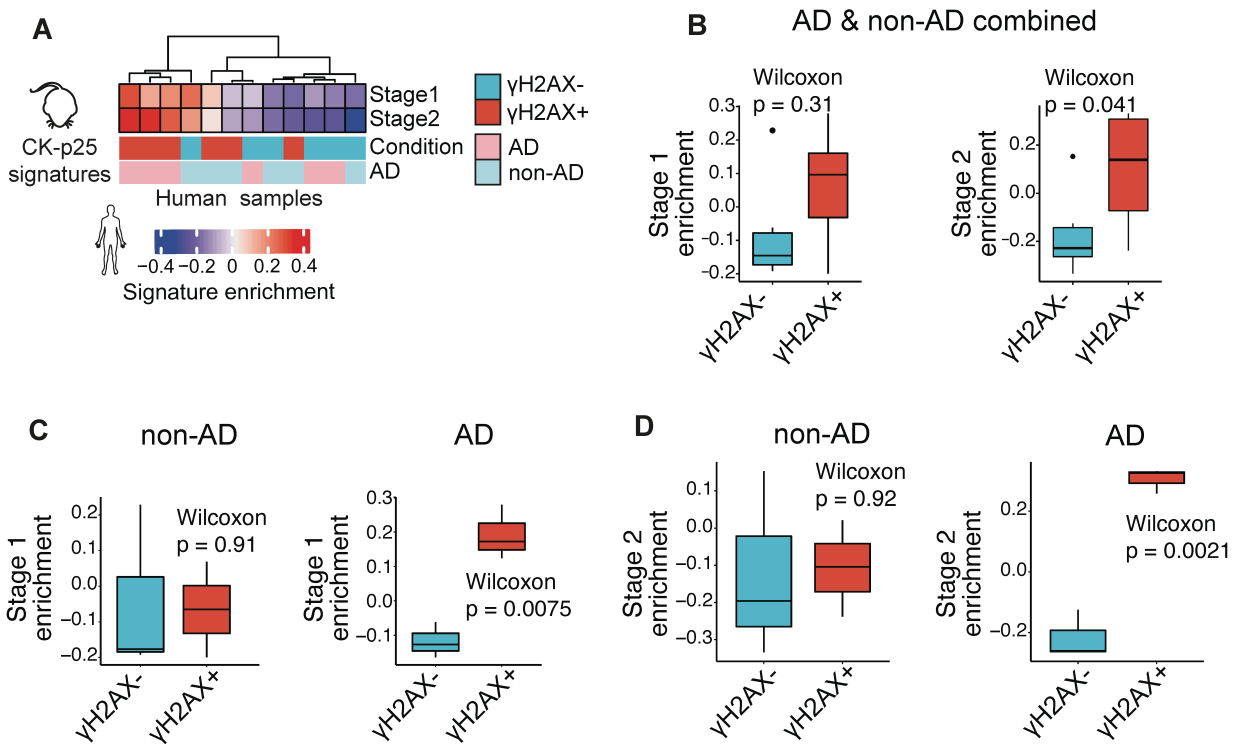

Figure 2-32 γH2AX^{hi} neurons from the AD brain are enriched in for Stage 1&2 gene signatures. (**A**) Heatmap of Stage 1 and Stage 2 signature enrichment in γH2AX^{hi} and γH2AX^{lo} human NeuN^{hi} nuclei. Quantification of Stage 1 and Stage 2 signature enrichment in γH2AX^{hi} and γH2AX^{lo} human NeuN^{hi} nuclei samples by FANS gate (**B**), and FANS gate and disease status (**C, D**). Error bars represent standard error of mean (S.E.M.). Wilcoxon test (B-D).

expression in γH2AX^{hi} neurons tended to be more similar to gene expression in ETP-treated neurons (Figure 2-33.B).

To further verify the enrichment of immune activation in DSB-bearing neurons from brains with AD pathology, we assessed nuclear p65 expression in NeuN-expressing neurons with high versus low burdens of DSBs in the AD postmortem brain. We acquired 4 prefrontal cortex tissue samples from individuals belonging to the Religious Orders Study cohort. All individuals analyzed exhibited AD pathology, described in Table A4. To bin neurons by DSB burden, we analyzed γH2AX expression in NeuN-expressing nuclei. The median γH2AX expression was calculated for each brain, and used to split

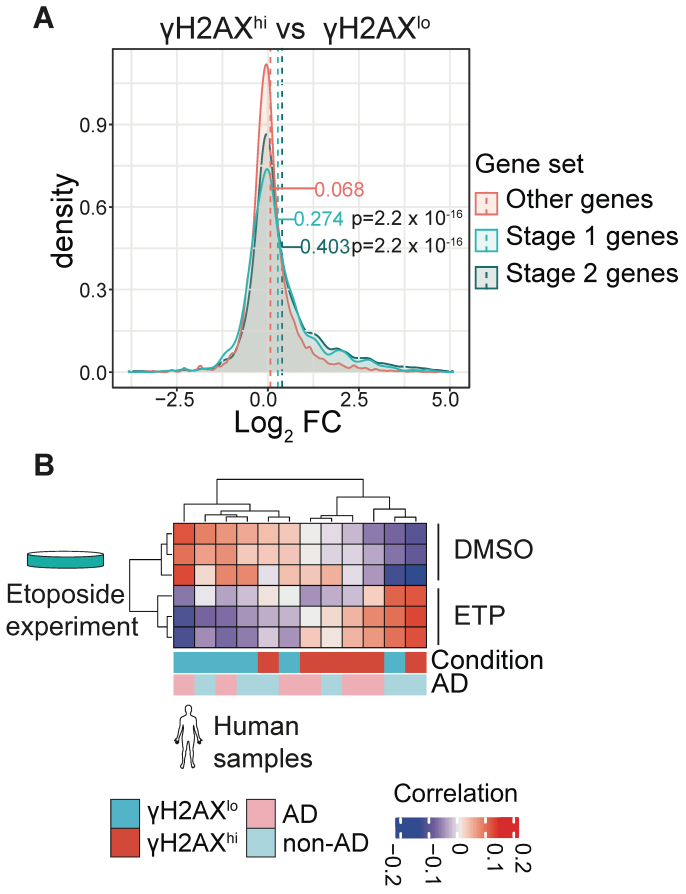

Figure 2-33 DNA damage signature enrichment in γH2AX+ neurons from the AD brain. (**A**) Distribution of $\log_2$ fold change values for Stage 1 genes (light blue), Stage 2 genes (dark blue), and other genes (red). $\log_2$ fold change values are from $\gamma H2AX^{hi}$ vs $\gamma H2AX^{lo}$ comparison. Mean $\log_2$ fold change for each gene set are compared with a Wilcoxon test. (**B**) Heatmap of ETP differentially expressed genes and their transcriptional correlation with $\gamma H2AX^{hi}$ and $\gamma H2AX^{lo}$ human neuronal nuclei.

neurons into the high or low DSB condition (Figure 2-34.A). Neurons with high DSB burden consistently expressed higher levels of nuclear p65 compared to neurons with low DSB burden (Figure 2-34.B, Figure 2-35). Furthermore, we observed a strong positive correlation between raw γH2AX values and raw p65 values when grouping together all neurons from all individuals (p<0.0001) (Figure 2-34.C).

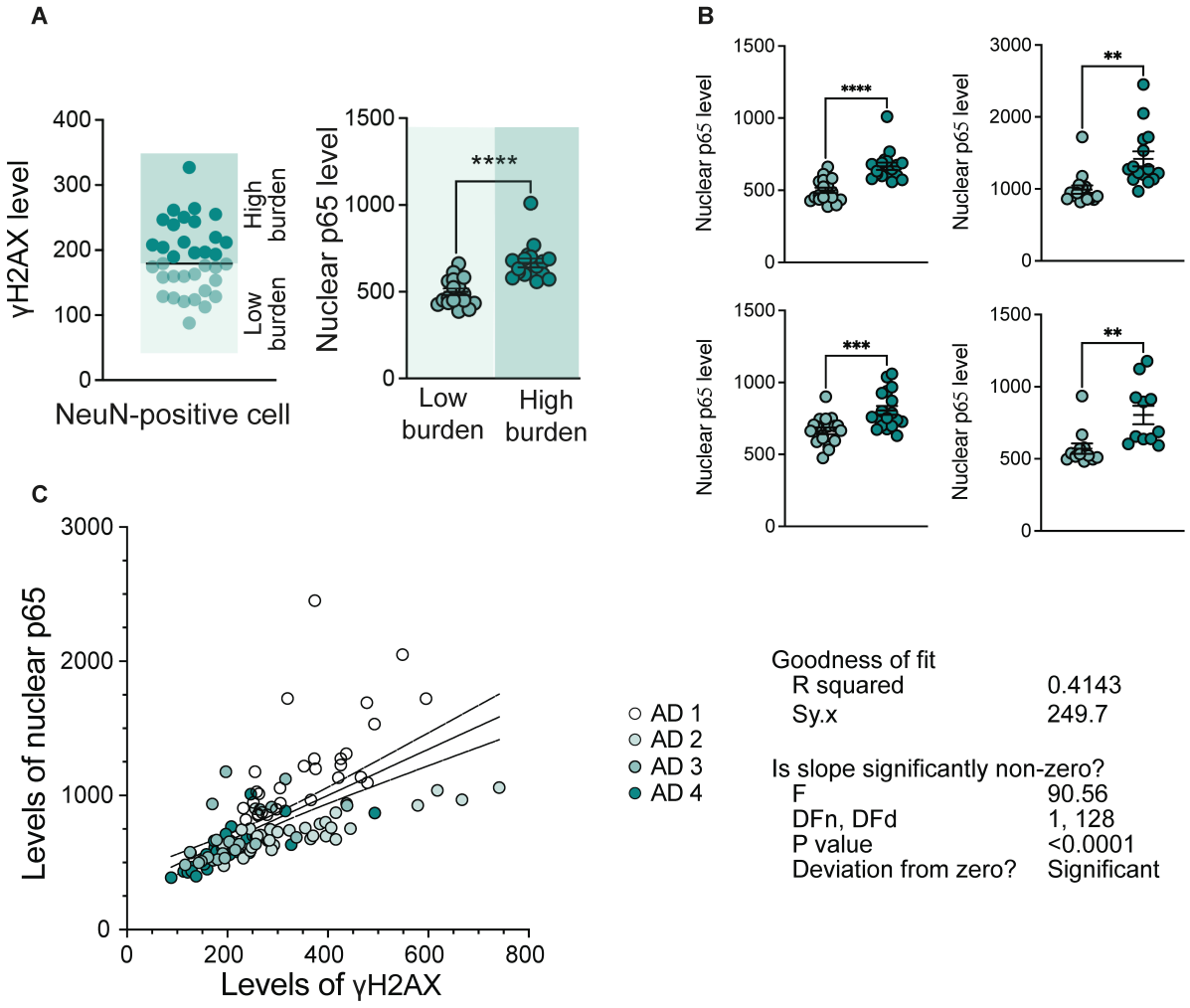

Figure 2-34 P65 expression positively correlates with γH2AX in AD neurons. (**A**) Schematic for binning γH2AX expression in NeuN+ cells and nuclear p65 quantification. For each individual, the median γH2AX expression in NeuN+ cells was calculated. Cells were then binned as 'High burden' or 'Low burden' based off of median γH2AX expression. Nuclear p65 intensity was calculated for all cells. (**B**) Raw p65 levels from the four AD individuals used for analysis. (**C**) (left): Scatterplot of raw γH2AX and p65 values for all AD individuals. Each data point represents p65 and γH2AX values from one NeuN+ cell. The color of the data point corresponds to the AD individual. (right): Simple linear regression for p65 vs. γH2AX. Error bars represent standard error of mean (S.E.M.); ****P<0.0001, ***P<0.001, **P<0.01, n.s. not significant. Student's T-test (A, B).

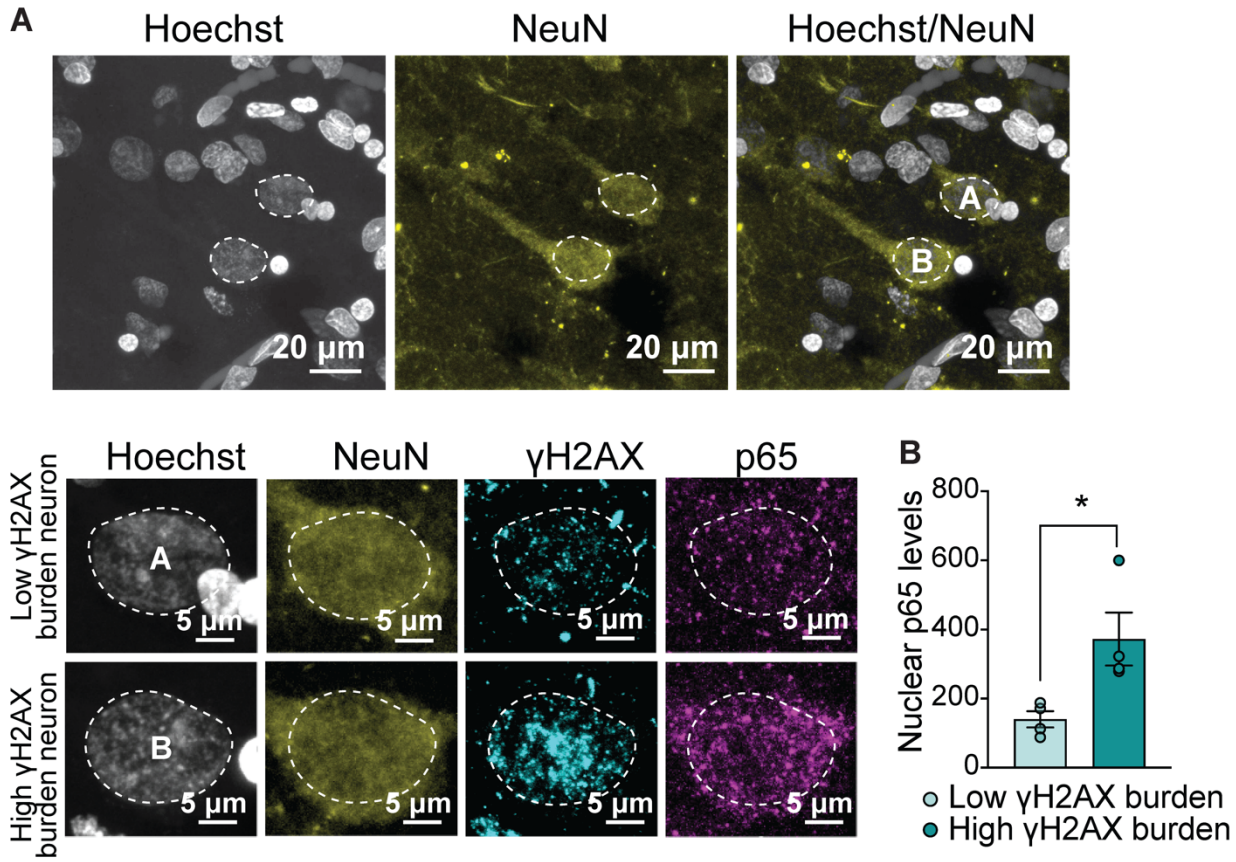

Figure 2-35 Neuronal p65 nuclear expression correlates with γH2AX in the AD brain. Representative image of γH2AX, p65, and NeuN in the AD brain. (top): Two NeuN+ nuclei are outlined (white dashed line). (bottom): magnification of the two outlined nuclei. Top nucleus (A) represents low DSB burden, bottom nucleus (B) represents high DSB burden. Quantification of p65 nuclear enrichment in low and high DSB-burdened neurons. Each dot represents the average of 23-41 NeuN+ nuclei per individual. Error bars represent standard error of mean (S.E.M.); *P<0.05. Student's T-test.

In summary, through the analysis of an independent snRNA-seq dataset, FANS RNA-sequencing and immunofluorescent microscopy, we found that Stage 1 and Stage 2 gene signatures were active in human DSB-bearing neurons. Furthermore, this neuronal immune signature was further amplified in the context of AD pathology, suggesting that it may serve a functional role in disease-associated neuroinflammation.

2.2.6 DSB-bearing neurons stimulate glial activation

We have previously published an in-depth characterization of reactive microglia in CK-p25 mice using snRNA-seq (188). We wondered if these microglia were responding to immune signaling from DSB-bearing neurons. To address this, we performed γH2AX immunostaining followed by spatial transcriptomics on two-week induced CK-p25 brains (Figure 2-36.A). The capture areas of 10X Visium spatial transcriptomics slides are large enough to encompass the transcriptional profile of 3-5 cells in mouse brain tissue. Therefore, we hypothesized that capture areas with γH2AX signal would also contain transcripts from nearby microglia. First, we identified 23 spatial clusters across three CK and four CK-p25 coronal sections (Figure 2-36.B, C, Figure 2-37.A, B). Next, we used a binary classification system to identify capture areas with γH2AX signal past a given threshold (i.e., γH2AX-positive capture areas) (See Methods, Figure 2-36.D, E, Figure 2-37.C). To determine if the reactive microglia characterized in Mathys et al., 2017 were enriched in γH2AX+ capture areas, we performed a differential comparison between all γH2AX+ capture areas and all γH2AX- capture areas. Using GSEA, we identified a robust enrichment of the microglia signature (1,383 significantly upregulated genes in reactive microglia compared to homeostatic microglia) within γH2AX+ capture areas (Figure 2-38.A). This indicated that overall, the reactive microglia signature characterized in Mathys et al., 2017 was significantly associated with γH2AX+ neurons.

By mapping the density of γH2AX+ capture areas across all spatial clusters, we further prioritized

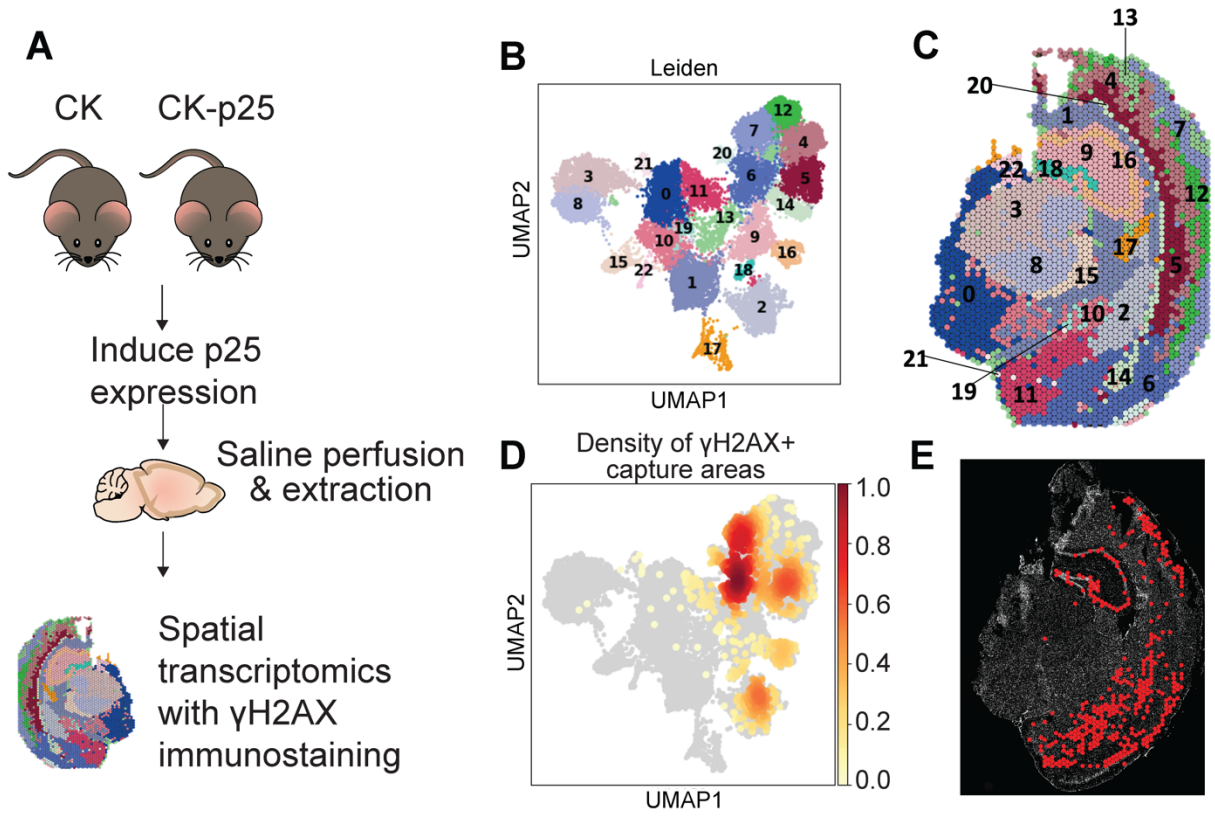

Figure 2-36 Spatial transcriptomics paired with γH2AX staining reveal brain regions dense with DSB-bearing neurons. (**A**) Schematic of spatial transcriptomics experiment. CK (n=3) and CK-p25 (n=4) were induced for two weeks. Coronal brain sections were stained and imaged for γH2AX, then sequenced. (**B**) UMAP of capture areas from all samples. Leiden clusters are indicated by color and number. Each dot represents one capture area. (**C**) Leiden clusters superimposed onto a CK-p25 brain slice used for spatial transcriptomics. (**D**) UMAP indicating the density of γH2AX+ capture areas. (**E**) γH2AX-positive capture areas identified in one CK-p25 brain slice.

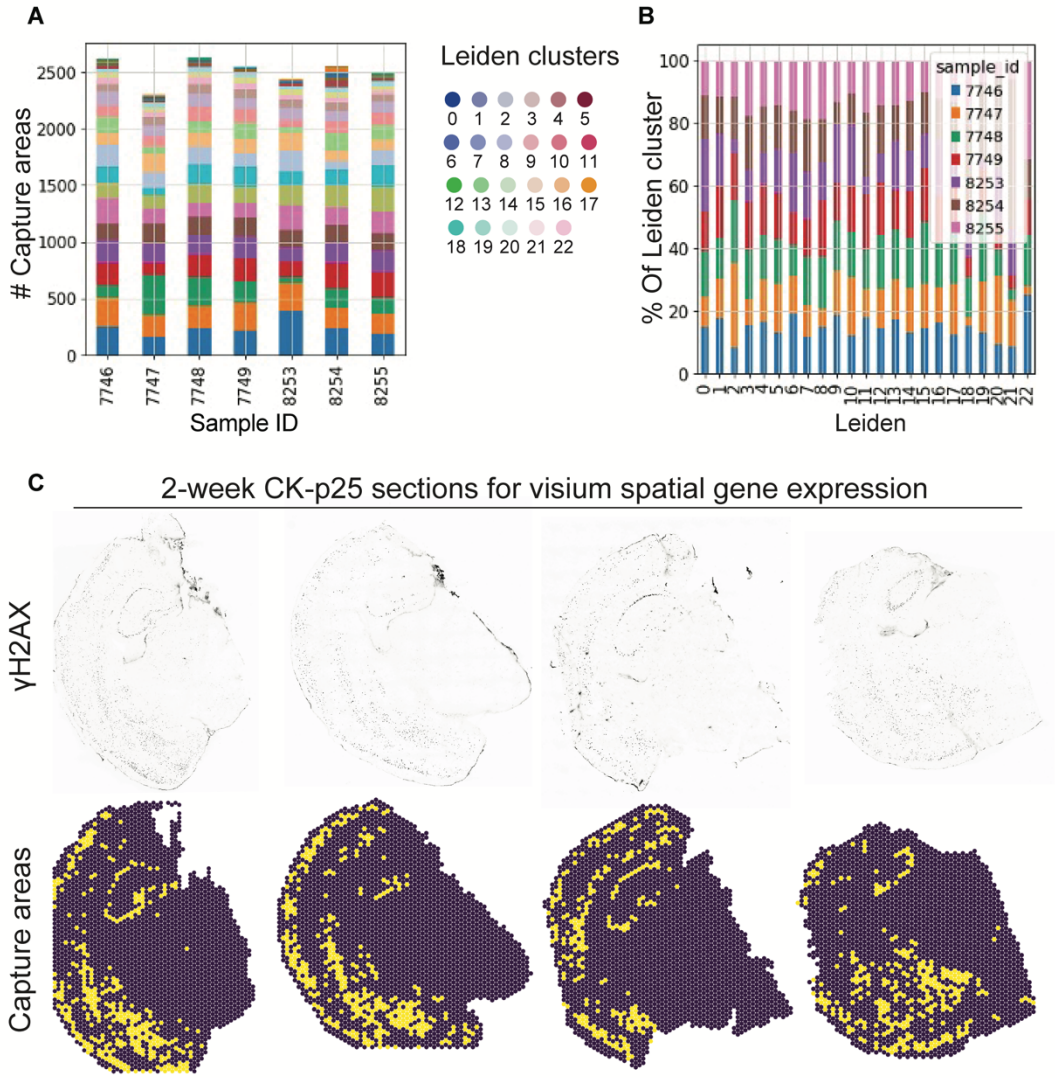

Figure 2-37 Spatial transcriptomics paired with γH2AX staining of CK-p25 coronal sections. (**A**) Distribution of capture areas amongst Leiden clusters for each sample. The y-axis refers to number capture areas. Colors refer to Leiden cluster ID. (**B**) Distribution of samples by spatial cluster. Colors refer to sample ID. (**C**) (top): γH2AX immunostaining for each CK-p25 section. (bottom): Corresponding capture areas identified as γH2AX+ are marked in yellow. γH2AX-capture areas are marked in purple.

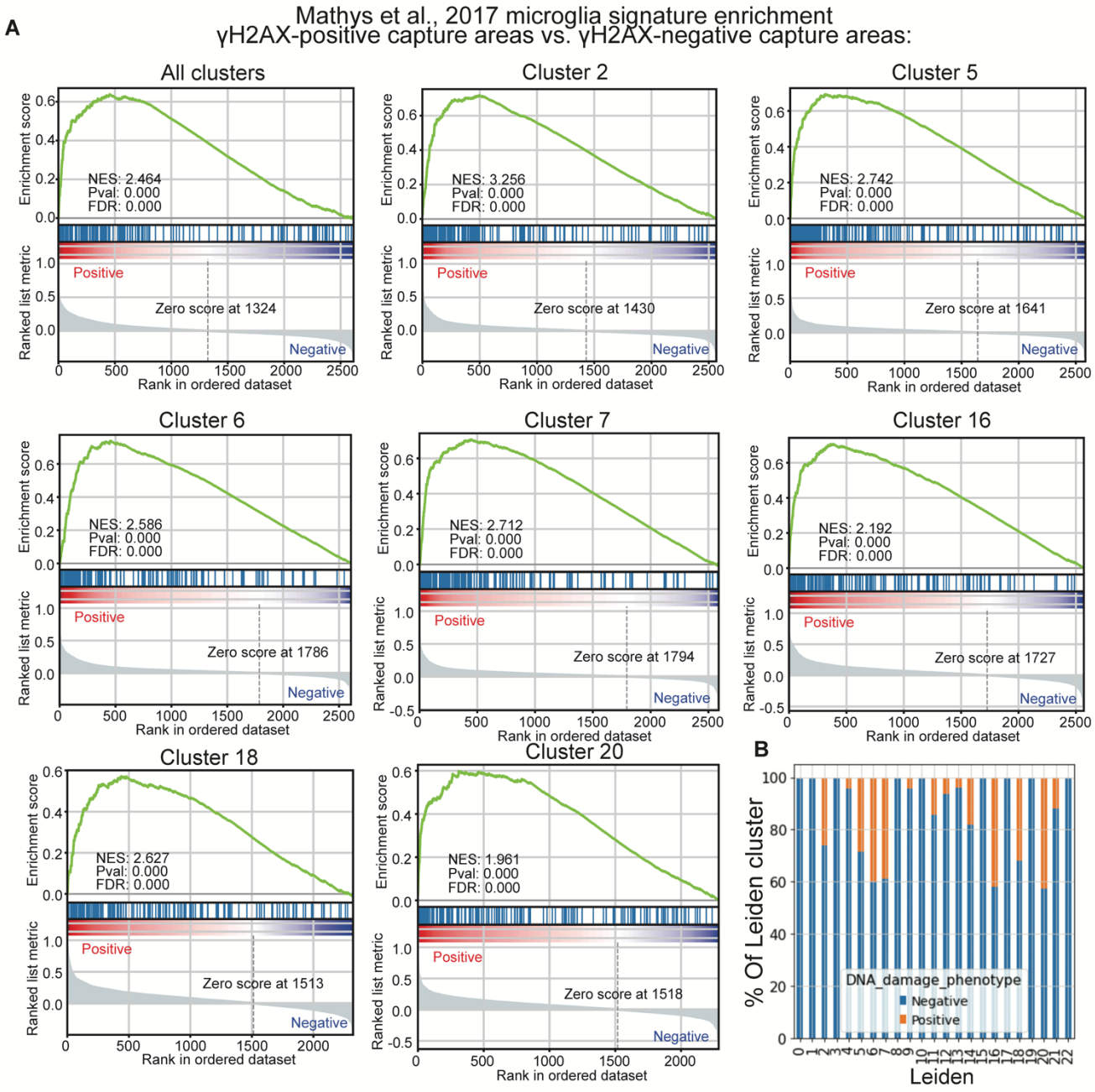

Figure 2-38 Reactive microglia gene signatures are enriched in brain regions dense with DSB-bearing neurons. (**A**) Gene set enrichment analysis of γH2AX+ capture area differentially expressed genes (DEGs). DEGs were tested for the enrichment of the reactive microglia signature (16). The analysis was first performed for all γH2AX+ capture areas, then for individual clusters comprised of 20% or more γH2AX+ capture areas. Normalized enrichment score (NES). False discovery rate (FDR). (**B**) Percent γH2AX+ capture areas by Leiden cluster. Orange indicates γH2AX+ capture areas. Blue indicates γH2AX- capture areas.

distinct spatial clusters enriched for γH2AX+ capture areas (Figure 2-36.D, Figure 2-38.B). We focused on spatial clusters with γH2AX+ capture areas comprising 20% or more of total capture areas (Figure 2-38.B). This included clusters 16 and 18, which corresponded to CA1, 2, 3 and the dentate gyrus respectively, and clusters 2, 5, 6, 7, which were primarily localized to the cortex. Differential comparisons of γH2AX+ capture areas and γH2AX- capture areas within each cluster of interest revealed a significant enrichment of the reactive microglia signature (Figure 2-38.A). Notably, many of the marker genes for reactive microglia displayed expression patterns that visually correlated with γH2AX+ capture areas, including the galectin gene *Lgals3bp*, lipase *Lpl*, cystatin *Cst7*, and MHC Class I gene *H2-D1* (Figure 2-39).

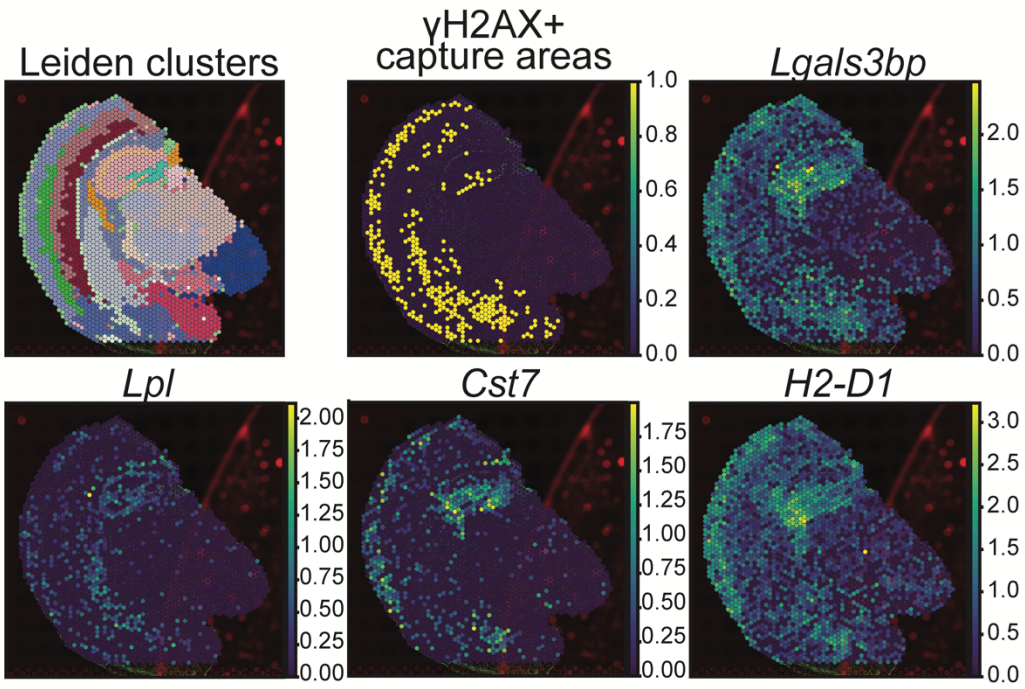

Figure 2-39 Spatial clusters, γH2AX+ capture areas, and reactive microglia signature gene expression in one CK-p25 sample.

To corroborate this finding, we also assessed the spatial relationship between microglia and DSB-bearing neurons through immunofluorescent microscopy (Figure 2-40.A). By analyzing the density of γH2AX+ neurons for each cortical layer, we were able to identify a strong enrichment of DSB-bearing neurons in layers 2/3 and 6 (Figure 2-40.B). Analyzing the number and size of Iba1+ microglia for each cortical layer revealed an increased density and size of microglia particularly in layers 2/3 (Figure 2-40.C), D), suggesting that regions with high densities of DSB-bearing neurons also have higher densities of microglia with larger soma area. The density of DSB-bearing neurons by cortical layer also seemed to associate with *Cxcl10* and *Ifitm3* expression levels and γH2AX+ capture areas identified through the Visium analysis (Figure 2-41). Collectively, these data indicated that reactive microglia are closely associated with γH2AX+ neurons, providing evidence for neuro-immune communication between damaged neurons and microglia.

To determine if microglia responded to DSB-mediated immune signaling, we sought to inhibit a master regulator of immune gene expression in neurons. Our data revealed that NFκB transcription factor activity is increased in DSB-bearing neurons, as are the genes downstream of NFκB activation. Therefore, we focused on inhibiting NFκB transcriptional activity. To achieve this in the CK-p25 mouse, we opted for brain-wide viral delivery of shRNAs targeting p65 (210). We performed retro-orbital injections of PHP.eb AAV shp65-RFP or Scramble-RFP into CK-p25 mice. CK control mice were injected with phosphate-buffered saline. Two weeks after injections, mice were taken off dox and induced for two weeks (Figure 2-42).

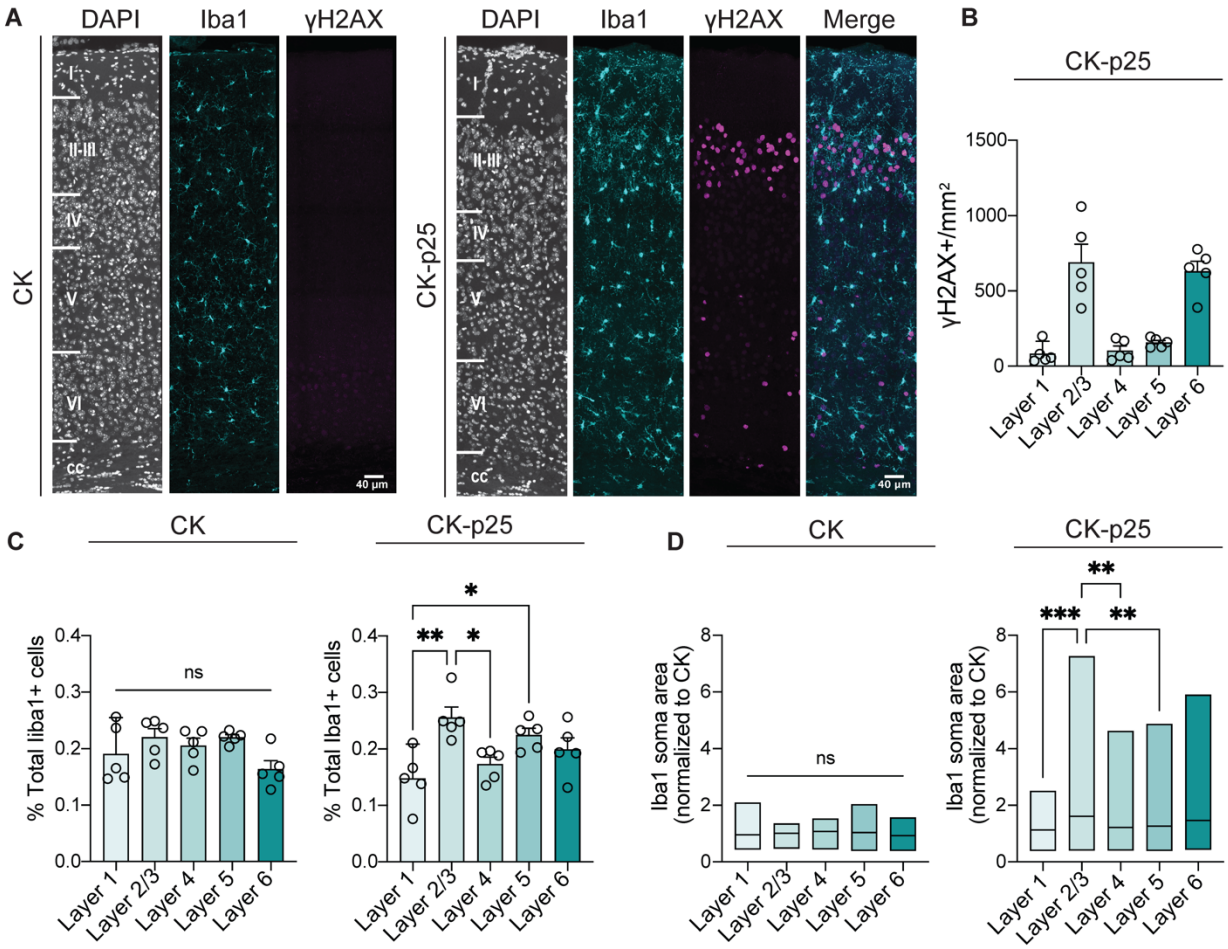

Figure 2-40 Microglia are recruited to brain regions dense with DSB-bearing neurons. (**A**) Representative images of CK and CK-p25 cortical layers, microglia (Iba1) are shown in turquoise and γH2AX are shown in magenta, Bregma = -2.0 mm AP. (**B**) Quantification of γH2AX+ nuclei density by cortical layer in 2-week induced CK-p25. Each data point represents one mouse. (**C**) Quantification of total Iba1+ cell distribution by cortical layer, normalized to CK. Each data point represents one mouse. (**D**) Quantification of Iba1+ soma area by cortical layer, normalized to CK. Box plots represent data from 236-289 Iba1+ cells per mouse. Error bars represent standard error of mean (S.E.M.); ***P<0.001, **P<0.01, *P<0.05, n..s. not significant. One-way ANOVA with Tukey's test for multiple comparisons (C, D).

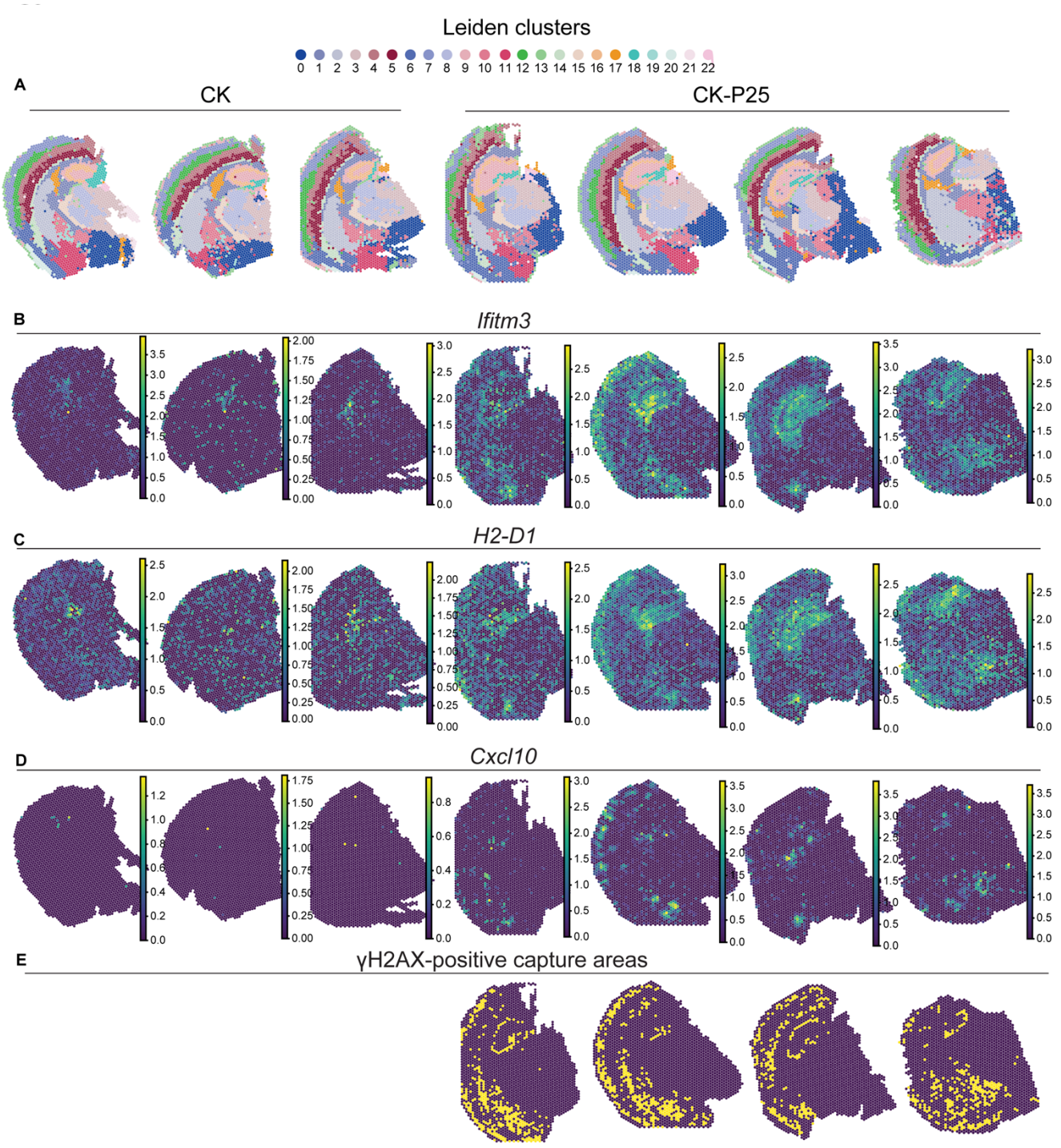

Figure 2-41 Gene expression across spatial transcriptomic capture areas. (**A**) Distribution of Leiden clusters for each sample. (**B-D**) Expression of reactive microglia and DSB-bearing neuron genes (**B**) *Ifitm3*, (**C**) *H2-D1*, and (**D**) *Cxcl10* for each sample. (**E**) Distribution of γH2AX+ capture areas for each CK-p25 sample.

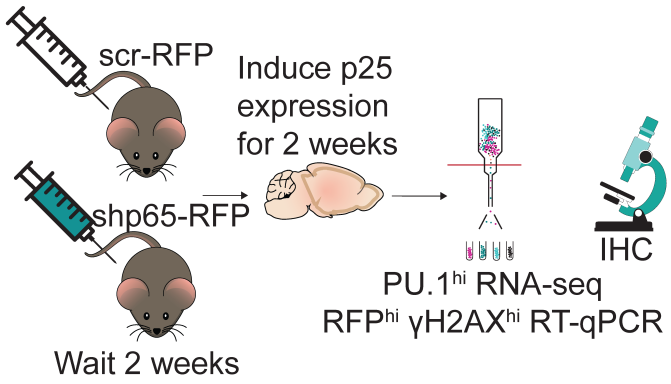

Figure 2-42 Schematic of neuronal p65 knock-down experiment. CK-p25 mice received retro-orbital injections of Scramble shRNA-RFP AAV or shp65-RFP AAV. CK mice received retro-orbital injections of PBS. Mice recovered for two weeks before being taken off dox. Brains were collected at the 2-week time point.

The majority of RFP co-localized with NeuN and γH2AX, indicating neurons were the primary targets of shRNA expression, and confirming the previously reported tropism of PHP.eb for neuronal infectivity (Figure 2-43.A, B)(210). The reduced expression of p65 in mice was confirmed via qPCR and immunofluorescent staining (Figure 2-43.C, D). The number of γH2AX+ neurons remained the same between p65 knock-down (p65kd) and Scramble mice (Figure 2-43.E). Next, we sorted γH2AX^{hi} RFP^{hi} neurons from both p65kd and Scramble mice to assess changes in immune gene expression (Figure 2-44). RT-qPCR analysis revealed that a number of immune genes were downregulated in DSB-bearing neurons from p65kd mice compared to Scramble, including *Ccl2, Icam1, Il6*, and *Cxcl1* (Figure 2-45.A). Downregulation of *Ccl2* in DSB-bearing neurons was also confirmed via RNAscope (Figure 2-45.B). This indicated knockdown of p65kd reduces neuron immune gene signatures.

To determine if suppressing neuron immune genes attenuates microglial activation, we performed immunofluorescent staining with the microglia marker Iba1. We found that microglia proliferation was suppressed in p65kd mice (Figure 2-46), which was confirmed through flow cytometry analysis of PU.1^{hi} nuclei from the entire cortex (Figure 2-47.A).

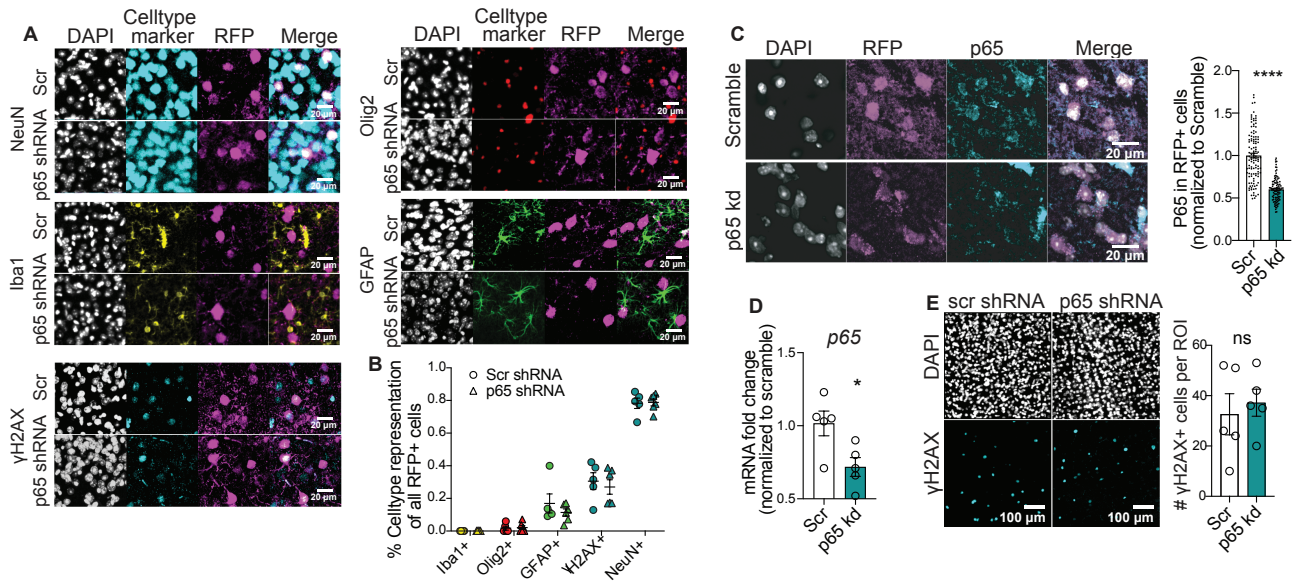

Figure 2-43 P65kd in 2-week CK-p25 cortex. (**A**) Representative images of cell type markers and RFP immunostaining in Scramble and p65kd cortex. Neurons (NeuN), microglia (Iba1), γH2AX+ cells (γH2AX), oligodendrocytes and oligodendrocyte precursor cells (Olig2), astrocytes (GFAP). (**B**) Quantification of RFP+ cell type distribution. Total number of RFP+ cells are quantified per image, then the fraction co-stained for a cell type marker are calculated. Each data point represents one mouse. (**C**) (left): P65 and RFP immunostaining in Scramble and p65kd CK-p25 cortex. (right): Quantification of p65 mean intensity. Data is from three animals, two sections each. Scramble n=113 cells, p65kd n=103 cells. (**D**) RT-qPCR of p65 in RFP^{hi} NeuN^{hi} nuclei from Scramble and shp65-treated CK-p25 mice. (**E**) (left): Representative images of γH2AX immunostaining in p65kd and Scramble CK-p25 cortex. (right): Number of γH2AX+ cells per image are quantified. Each data point represents one mouse. Error bars represent standard error of mean (S.E.M.); ****P<0.0001, ***P<0.001, **P<0.01, *P<0.05, n.s. not significant. Student's t-test (C-E).

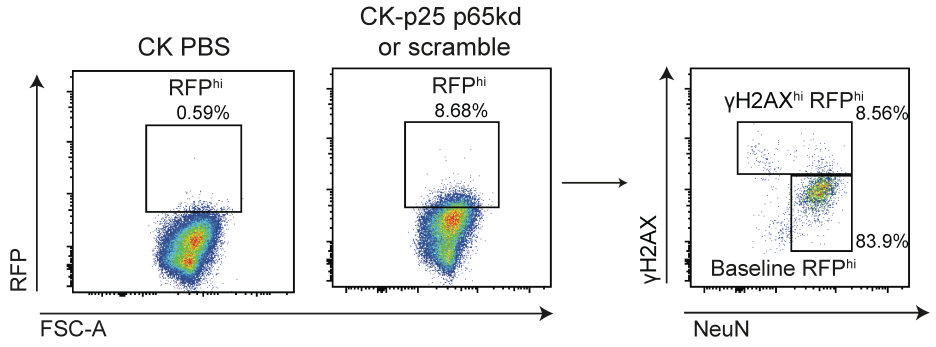

Figure 2-44 Sorting schematic for RFP^{hi} γH2AX^{hi} and γH2AX^{lo} neurons. 30,000 nuclei were collected for each gate for each animal.

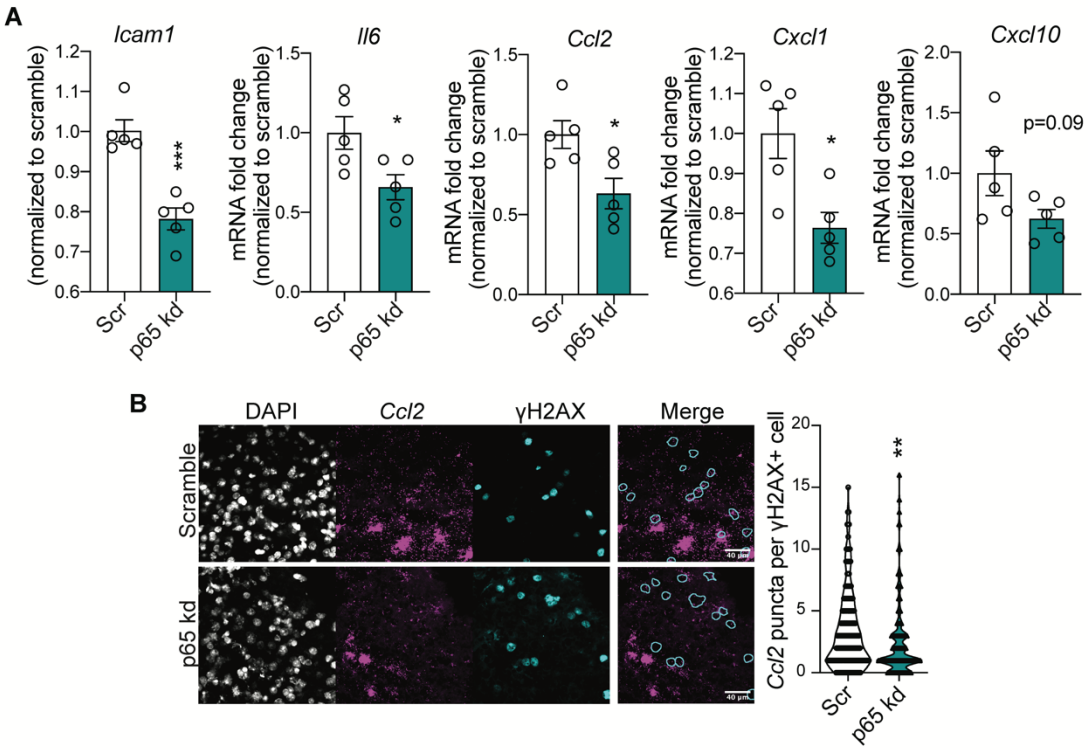

Figure 2-45 p65kd suppresses immune gene expression in γH2AX^{hi} neurons. (**A**) qRT-PCR of immune genes in sorted RFP^{hi} γH2AX^{hi} nuclei. (**B**) (left): Representative images of Ccl2 RNAscope combined with γH2AX immunofluorescence in Scramble and p65kd cortex. (right): Quantification of Ccl2 puncta per γH2AX+ cell. Each data point represents one cell (n=197 for Scramble, n=157 for p65kd). 20-40 cells were analyzed per mouse. Error bars represent standard error of mean (S.E.M.); ****P<0.0001, ***P<0.001, **P<0.01, *P<0.05; n.s. not significant. Student's T-test. Scramble (n=5), p65kd (n=5). I: CK (n=7), Scramble (n=5), p65kd (n=6).

We also found that microglia soma area was significantly reduced, but differences in branch length and end points were not statistically significant (Figure 2-46). These data show that suppressing neuron immune signaling significantly alters the number and morphology of microglia.

To determine if changes in microglia number and morphology were accompanied with changes in gene expression, we performed RNA sequencing on sorted PU.1^{hi} nuclei from CK control, CK-p25-Scramble, and CK-p25-p65kd cortex (Figure 2-42, Figure 2-47). Differential analysis comparing microglia from p65kd and Scramble cortices revealed the upregulation of 627 transcripts and downregulation of 160 transcripts (Figures 2-47.C, 2-48.A). Genes that were downregulated

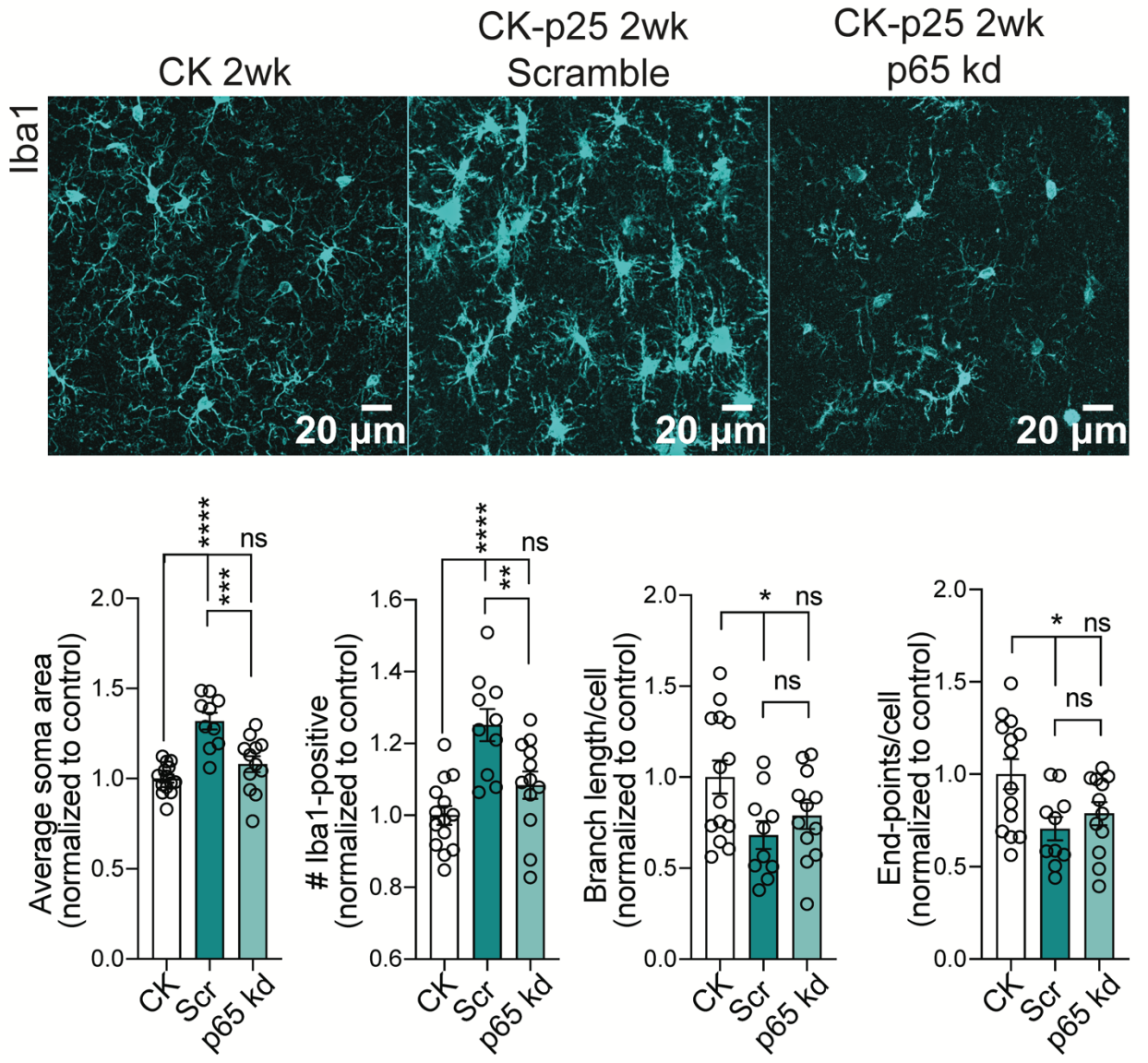

Figure 2-46 CK-p25 microglia respond to p65kd in neurons. (top): Representative images of Iba1 in CK, Scramble, and p65kd cortex. (bottom): Quantification of (left to right): Iba1+ soma area, number Iba1+ per image, average branch length per Iba1+ cell, and number end-points per Iba1+ cell. Each data point represents one image. Two images were taken per mouse. Error bars represent standard error of mean (S.E.M.); ****P<0.0001, ***P<0.001, **P<0.01, *P<0.05; n.s. not significant. One-way ANOVA followed by Tukey's test for multiple comparisons.

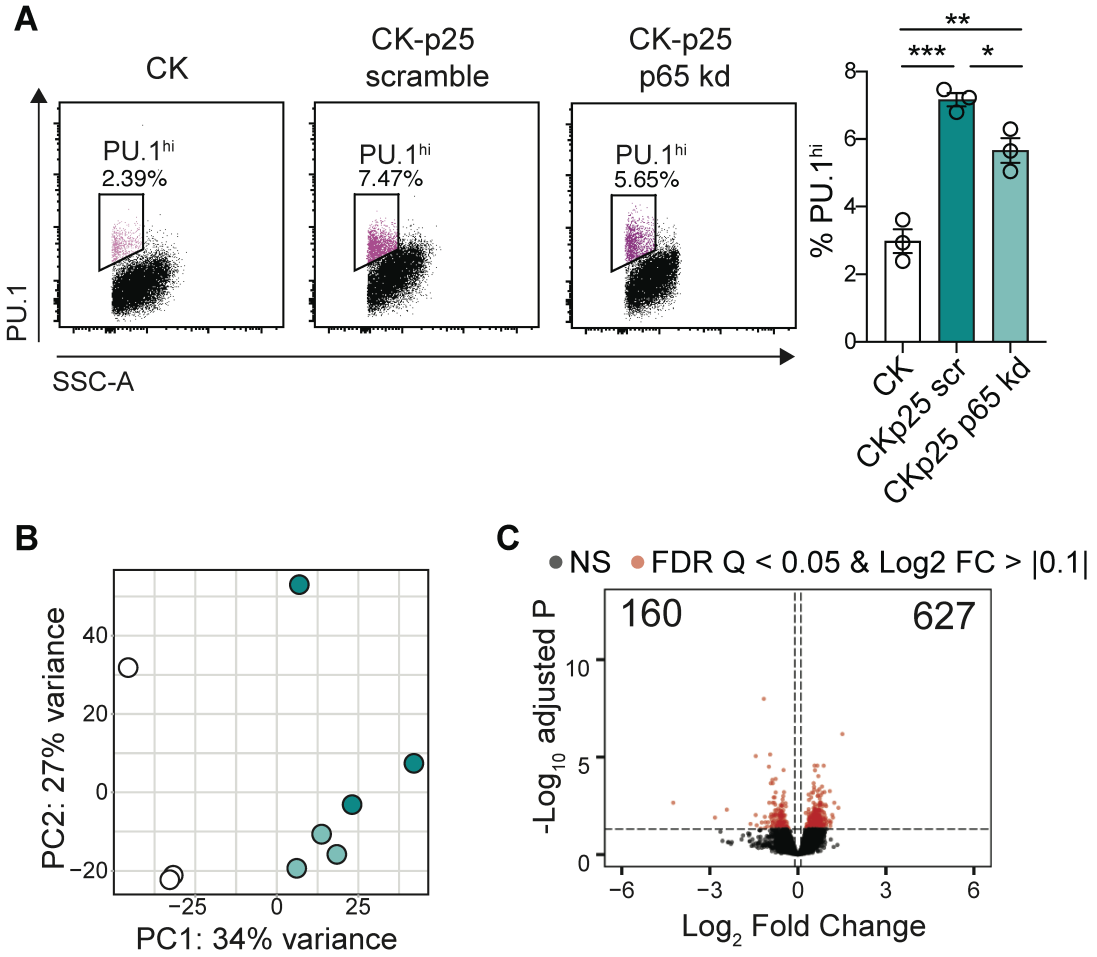

Figure 2-47 Microglia number are reduced in p65kd CK-p25 mice. (**A**) (left): Sorting schematic for Pu.1^{hi} nuclei for bulk RNA-sequencing. (right): Quantification of total percent Pu.1^{hi}. One data point represents one mouse. (**B**) PCA plot of normalized gene expression from Pu.1^{hi} bulk RNA-sequencing. (**C**) Volcano plot from 65 vs. Scramble contrast. Gray circles: non-significant (ns) transcripts. Red circles: transcripts with FDR adjusted p-value <0.05 and log2 fold change >|0.1|. Number of significantly upregulated and downregulated transcripts are shown in the upper right and left corners of the volcano plots respectively. Error bars represent standard error of mean (S.E.M.); ***P<0.001, **P<0.01, *P<0.05. One-way ANOVA followed by Tukey's test for multiple comparisons (A).

in microglia from p65kd mice were involved in cell killing and antigen processing, such as *H2-Q2*, *Lag3*, *Ccr5*, and *Ccr2*. Notably, the *Ccr2* gene encodes the receptor for CCL2, further implying an alteration of the CCL2-CCR2 axis compared to scramble mice (Figure 2-48.B, C). We also observed a downregulation of genes related to lipoprotein processing (Figure 2-48.B,C). Interestingly, pathways related to synaptic activity and membrane organization were significantly upregulated in microglia from p65kd mice. This included calcium channels *Cacna1g*, *Cacna1c*, and *Cacnb2*, and sodium channel *Scn1a*, suggesting p65kd microglia may return to a more homeostatic state embodied by CK microglia (Figure 2-48.B). Together, these results suggest that neuron immune signaling disrupts microglia homeostatic activity and activate cell killing and antigen processing mechanisms in microglia.

To gain a better understanding of how microglia respond to neuronal p65kd over time, we generated a mir30-based shRNA driven by an hSyn promoter packaged in AAV-PHP.eB to suppress p65 exclusively in neurons (Figure 2-49.A). CK-p25 brains injected with mir30-based shp65 were collected for analysis at 1, 2, and 6 weeks after p25 induction (Figure 2-49.B). After confirming suppression of p65 expression (Figure 2-49.C, D), we assessed microglia number and morphology at each timepoint (Figure 2-50.A). We found that neuronal p65kd was able to suppress microglial proliferation for 1 through 6 weeks of p25 induction (Figure 2-50.A, B). Neuronal p65kd was also able to ameliorate branch shortening and end-point reduction at 1 and 2 weeks, but not at 6 weeks (Figure 2-50.C). While we did not observe any rescue in microglia morphology at the 6-week timepoint, we did observe a significant reduction in the percentage of microglia that were MHCII-positive (Figure 2-51). MHCII expression is a hallmark feature of late-responding microglia in CK-p25 (188). Interestingly, while neuronal p65kd did not affect levels of endogenous amyloid-beta, phosphorylated tau, or neuronal loss, we observed a striking rescue of synaptic density as measured by vGlut1 and Synaptophysin (Figures 2-52, 2-53). We also observed a

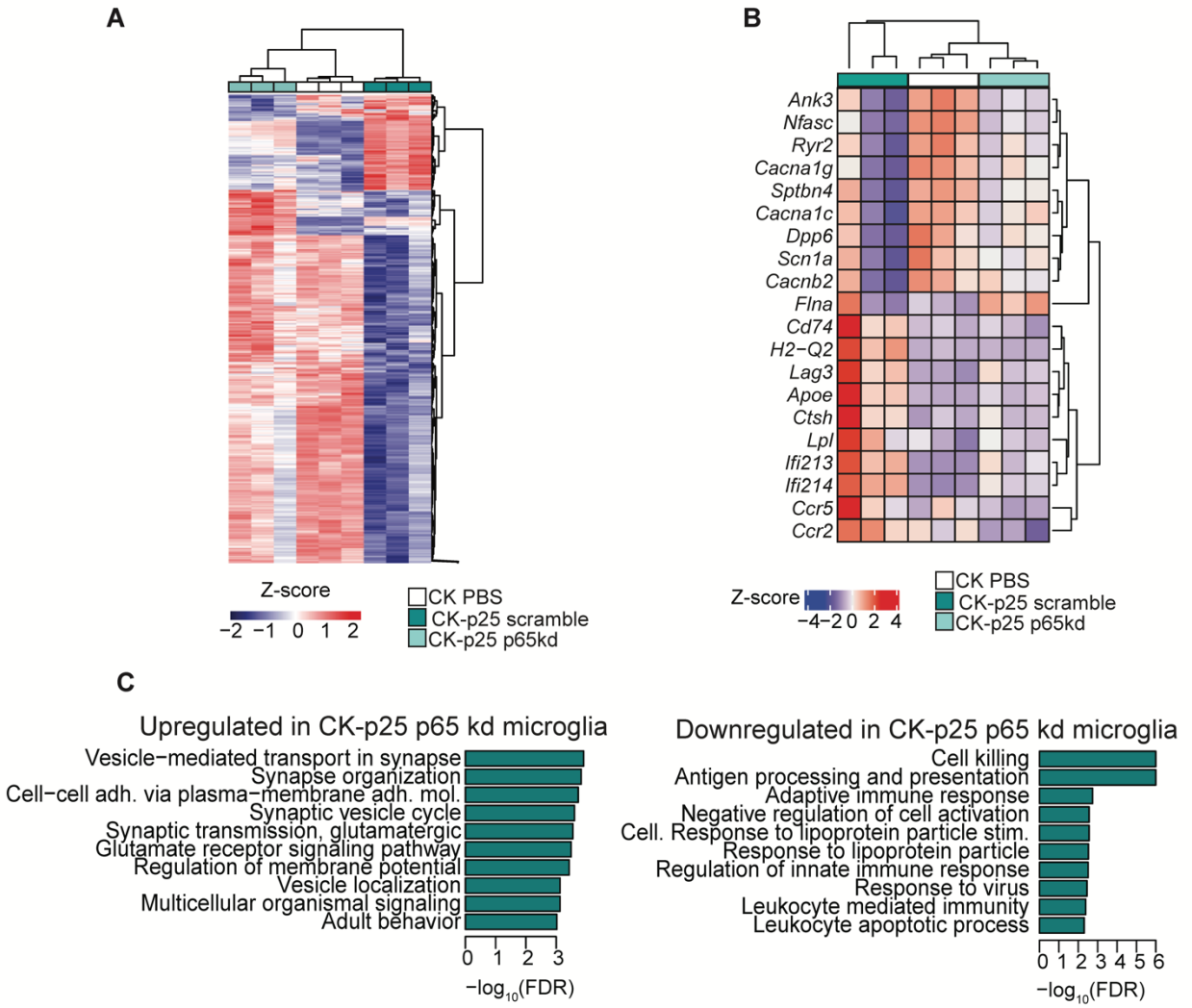

Figure 2-48 CK-p25 microglia gene expression is altered in response to p65kd in neurons. (**A**) Heat map of differentially expressed genes from p65 vs. Scramble contrast. (**B**) Heatmap of significantly upregulated and downregulated genes in Pu.1^{hi} nuclei from p65kd cortex compared to Pu.1^{hi} nuclei from Scramble cortex. (**C**) Upregulated and downregulated gene ontology (biological pathway) terms identified through GSEA of p65kd vs. Scramble contrast.

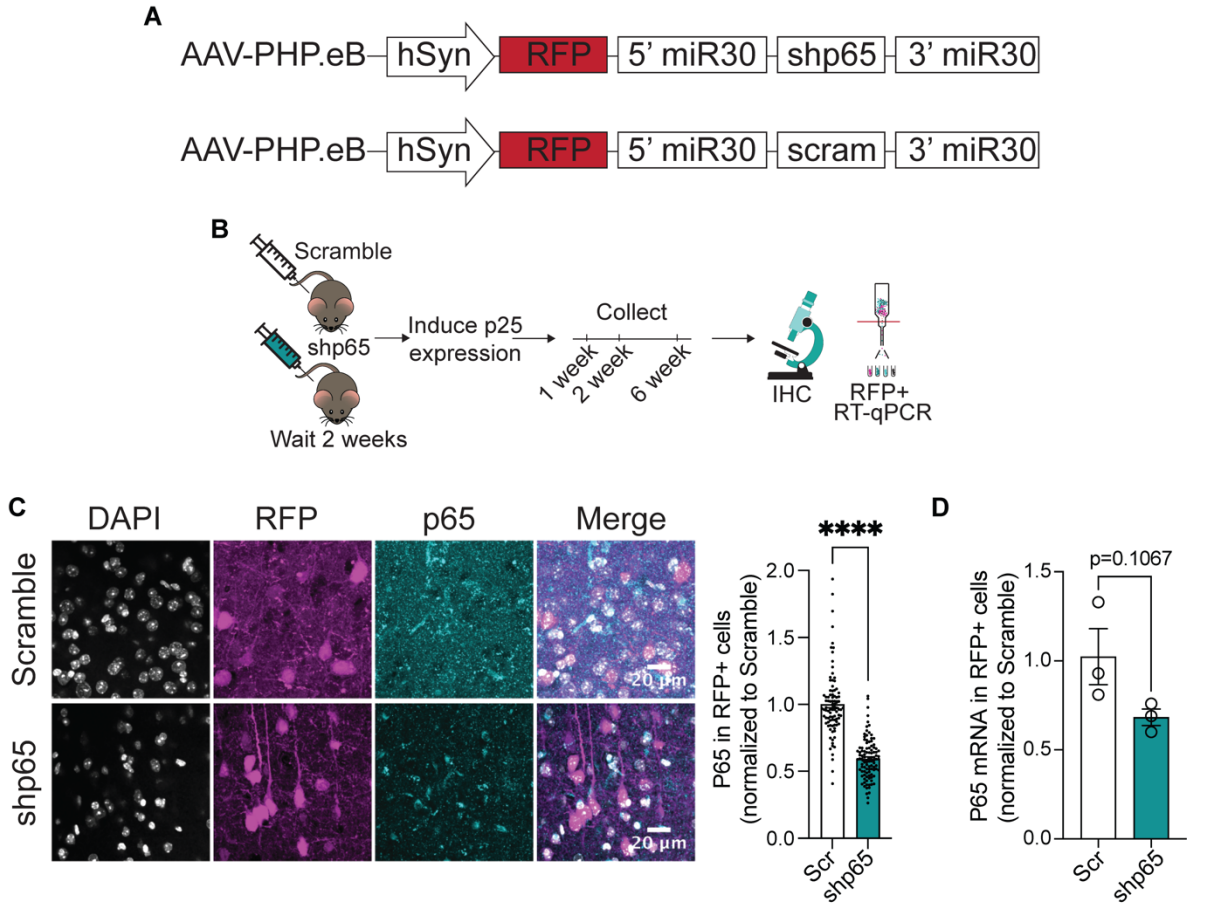

Figure 2-49 Neuron-specific p65kd. (**A**) Schematic of construct used to knock down p65 in a cell-type specific manner. (**B**) Schematic of collection timepoints after p65 knockdown. After intracranial injection of AAVPHP.eB-hSYN-RFP-mir30-shp65 or scramble, mice were allowed to recover for two weeks before being taken off a doxycycline diet. Brains were collected for analysis at 1, 2, and 6-week time points. (**C**) (left): P65 and RFP immunostaining in Scramble and p65kd CK-p25 cortex. (right): Quantification of p65 mean intensity. Analysis was performed on three animals, two sections each (Scramble n=92, shp65 n=102). (**D**) RT-qPCR of p65 in RFP+ nuclei from scramble and shp65-treated CK-p25 mice. Error bars represent standard error of mean (S.E.M.); ****P<0.0001. Student's T-test (C, D).

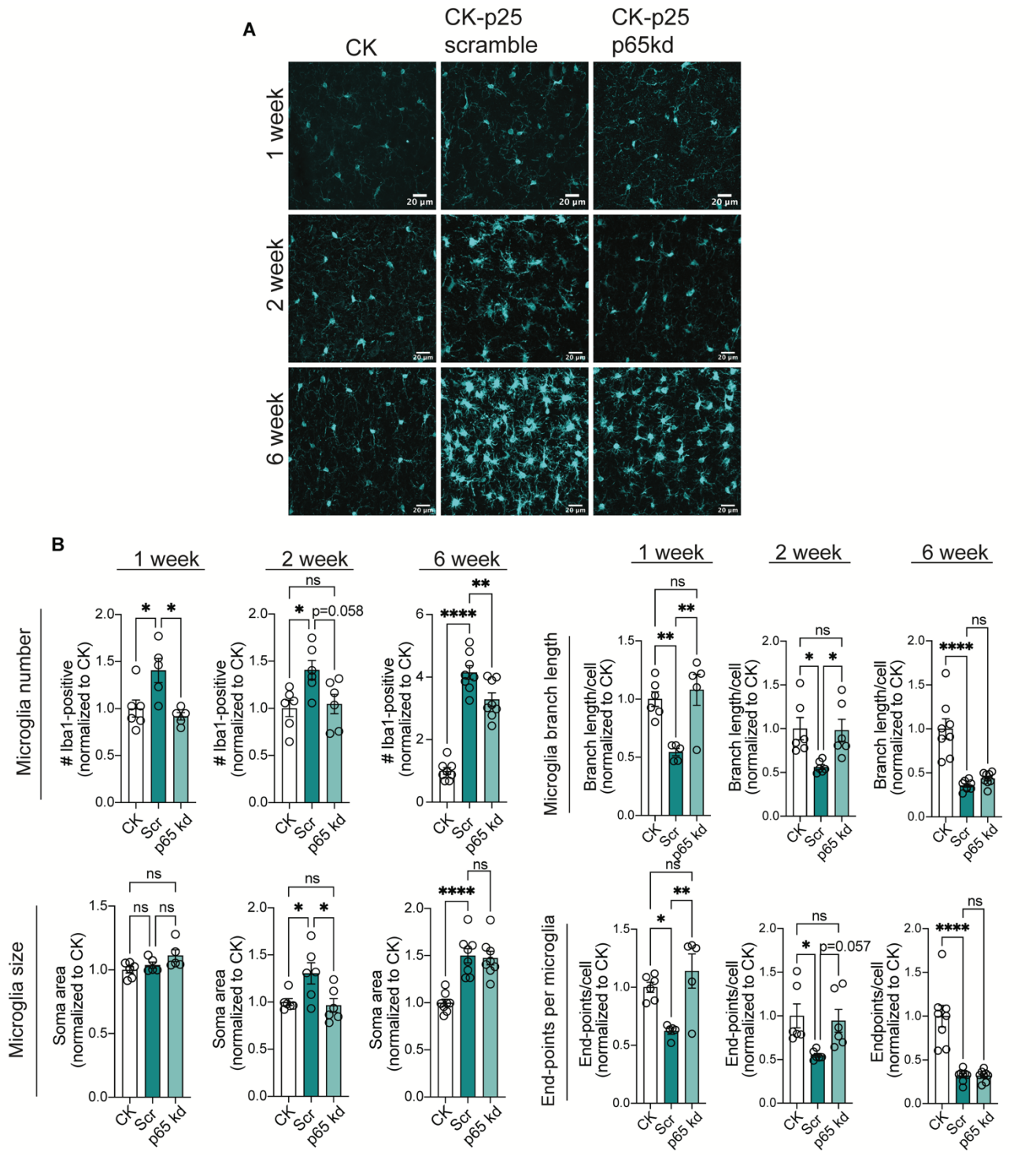

Figure 2-50 P65kd in neurons suppresses microglial proliferation. (**A**) Representative images of Iba1 immunostaining in CK, Scramble, and p65kd cortex at 1-week, 2-week, and 6-week time points. (**B**) (top): Quantification of average number Iba1+ per mouse. (bottom): Average Iba1+ soma area per mouse. Each data point represents one mouse. Two images were taken per mouse. (1-week: CK n=6, CK-p25 Scramble n=5, CK-p25 p65kd n=5; 2-week: CK n=6, CK-p25 Scramble n=6, CKp25 p65kd n=6; 6-week: CK n=8, CK-p25 Scramble n=8, CK-p25 p65kd n=8). (**C**) (top): average branch length per Iba1+ cell, and (bottom): number end-points per Iba1+ cell. Each data point represents one mouse. Two images were taken per mouse. (1-week: CK n=6, CK-p25 Scramble n=5, CK-p25 p65kd n=5; 2-week: CK n=6, CK-p25 Scramble n=6, CKp25 p65kd n=6; 6-week: CK n=8, CK-p25 scramble n=8, CK-p25 p65kd n=8). Error bars represent standard error of mean (S.E.M.); ****P<0.0001, **P<0.01, *P<0.05, n.s. not significant. One-way ANOVA followed by Tukey's test for multiple comparisons (B, C).

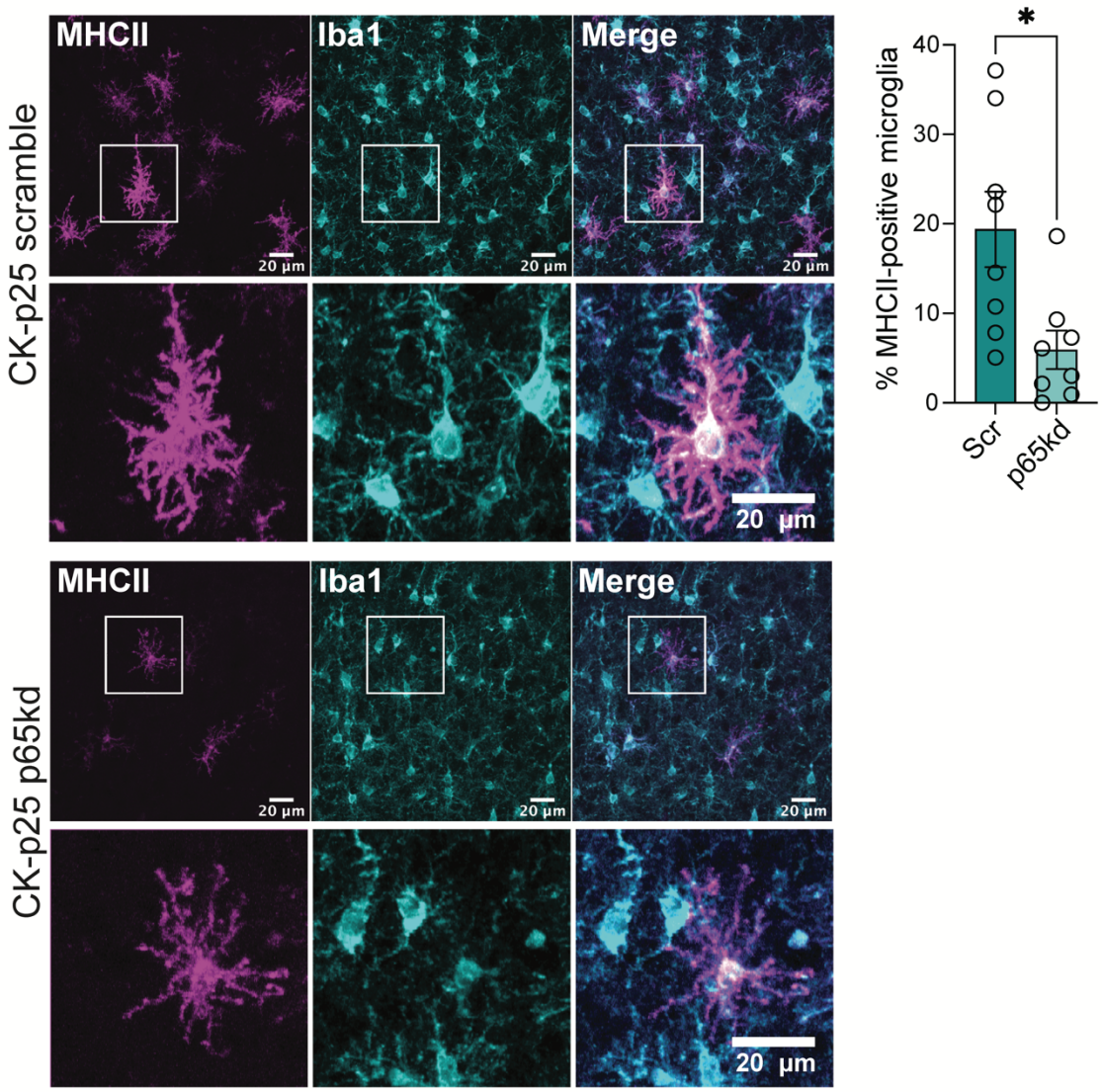

Figure 2-51 P65kd in neurons reduces MHCII+ microglia at late stages of neurodegeneration. (left): Representative images of Iba1 and MHCII in CK-p25 Scramble and CK-p25 p65kd mice 6-week time point. (right): Quantification of percent MHCII+ Iba1+ microglia in Scramble and p65kd. Each data point represents one mouse. Two images were taken per mouse. MHCII+ microglia were not observed in CK mice. CK-p25 Scramble n=8, CK-p25 p65kd n=8. Error bars represent standard error of mean (S.E.M.); *P<0.05. Student's T-test.

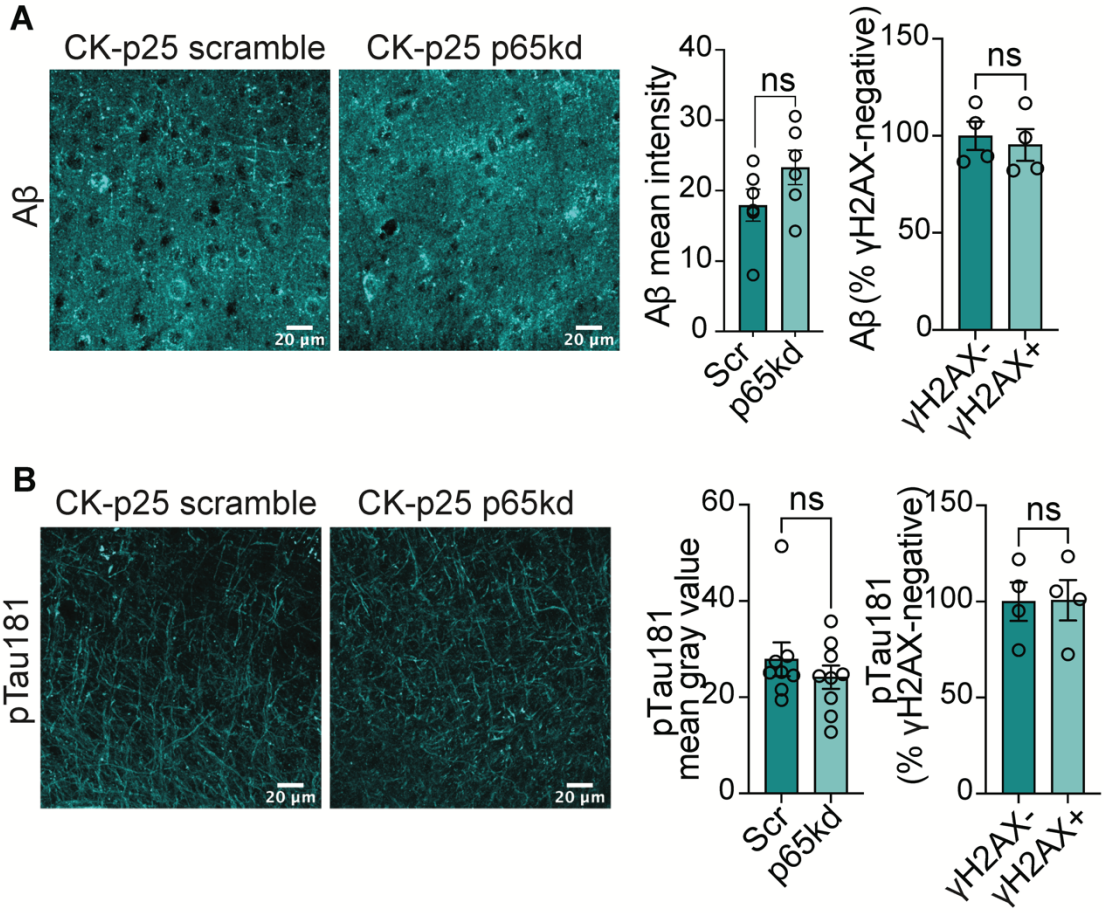

Figure 2-52 Neuron-specific p65kd does not alter amyloid or phosphorylated tau in CK-p25 cortex. (**A**) (right): Representative images of amyloid beta in 2-week CK-p25 Scramble and CK-p25 p65kd cortex. (left): Quantification of amyloid beta levels in CK-p25 Scramble and CK-p25 p65kd cortex. Quantification of amyloid beta levels in γH2AX+ vs γH2AX- neurons in CK-p25 Scramble cortex. Each data point represents one mouse. Two images were taken per mouse. (CK-p25 Scramble n=6, CK-p25 p65kd n=6). 4 animals from each condition were used for analysis of amyloid beta levels in γH2AX+ and γH2AX- neurons. (**B**) (right): Representative image of phospho-Tau181 in 6-week CK-p25 Scramble and CK-p25 p65kd cortex. (left): Quantification of phospho-Tau181 levels in CK-p25 Scramble and CK-p25 p65kd cortex. Quantification of phospho-Tau181 levels in γH2AX+ vs γH2AX- neurons in CKp25 Scramble cortex. Each data point represents one mouse. Two images were taken per mouse. (CK-p25 Scramble n=8, CK-p25 p65kd n=9). 4 animals from each condition were used for analysis of phospho-Tau181 levels in γH2AX+ and γH2AX- neurons.

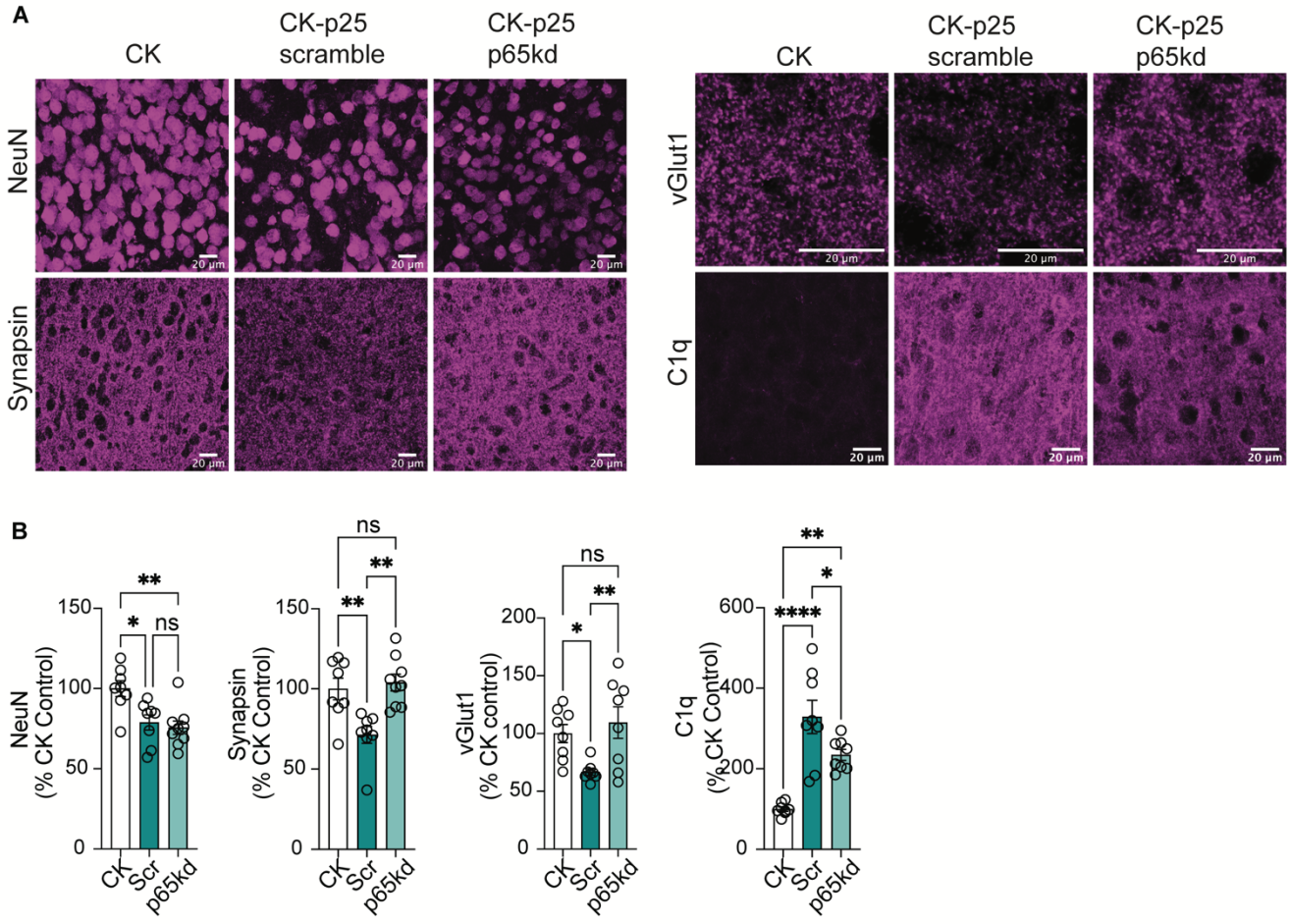

Figure 2-53 P65kd in neurons rescues synaptic density at late stages of neurodegeneration. (**A**) Representative images of (top left): NeuN, (bottom left): Synapsin, (top right): vGlut1, and (bottom right) C1q. All images were taken at the 6wk time point. (**B**) Quantification of (left to right): NeuN, Synapsin, vGlut1, and C1q in CK, CK-p25 Scramble, and CK-p25 p65kd cortex. Each datapoint represents one mouse. Two images were taken per mouse. (NeuN and Synapsin: CK n=8, CK-p25 Scramble n=8, CK-p25 p65kd n=9; vGlut1 and C1q: CK n=8, CK-p25 Scramble n=8, CK-p25 p65kd n=8). Error bars represent standard error of mean (S.E.M.); ****P<0.0001, **P<0.01, *P<0.05, n.s. not significant. One-way ANOVA followed by Tukey's test for multiple comparisons.

corresponding decrease in the complement protein C1q, which is implicated in synaptic loss in other models of neurodegeneration (211,212). Combined, these data suggest neuronal NFκB promotes microglial proliferation and synaptic degradation in the CK-p25 mouse.

To determine if specific cytokines expressed and secreted by DSB-bearing neurons play a role in microglia activation, we transitioned to our *in vitro* ETP model of DNA damage. First, we wanted to understand how conditioned media from ETP-treated neurons affect microglia morphology. To do this, we generated organotypic acute brain slice cultures from *Cx3cr1*-GFP mice, which express GFP in all microglia. After ETP treatment and washout with PBS, neurons recovered in fresh media for 24 hours. This conditioned media was then collected and applied to *Cx3cr1*-GFP brain slices for 6 hours (Figure 2-54.A). The conditioned media from ETP-treated neurons reduced microglia branch length (Figure 2-54.B, C), but did not significantly affect the number of endpoints per microglia (Figure 2-54.D). We also observed increased soma area (Figure 2-54.E). Treating primary neurons with an NFκB activation inhibitor (10μM NF-kappaB Activation Inhibitor VI) before and during ETP treatment significantly reduced the soma area of *Cx3cr1*-GFP-expressing microglia, and increased branch length and end-points (Figure 2-54.B-E). Conditioned media from ETP-treated neurons did not elicit a robust difference in the number of microglia analyzed per image (Figure 2-54.F). These data further demonstrate NFκB activity as a significant mediator of immune signaling in DSB-bearing neurons.

Notably, conditioned media from ETP-treated neurons was significantly enriched for CXCL10 and CCL2 (Figure 2-55). Furthermore, the NFκB activation inhibitor reduced the concentration of these cytokines in conditioned media (Figure 2-55). Previously, we found that DSB-bearing neurons are the first cells to express CXCL10 and CCL2 in the CK-p25 cortex (Figure 2-11). These cytokines induce the migration of macrophages and T cells to sites of viral infection and traumatic brain injury (174,200,213), suggesting that they may be primary constituents of immune signaling in DSB- bearing neurons.

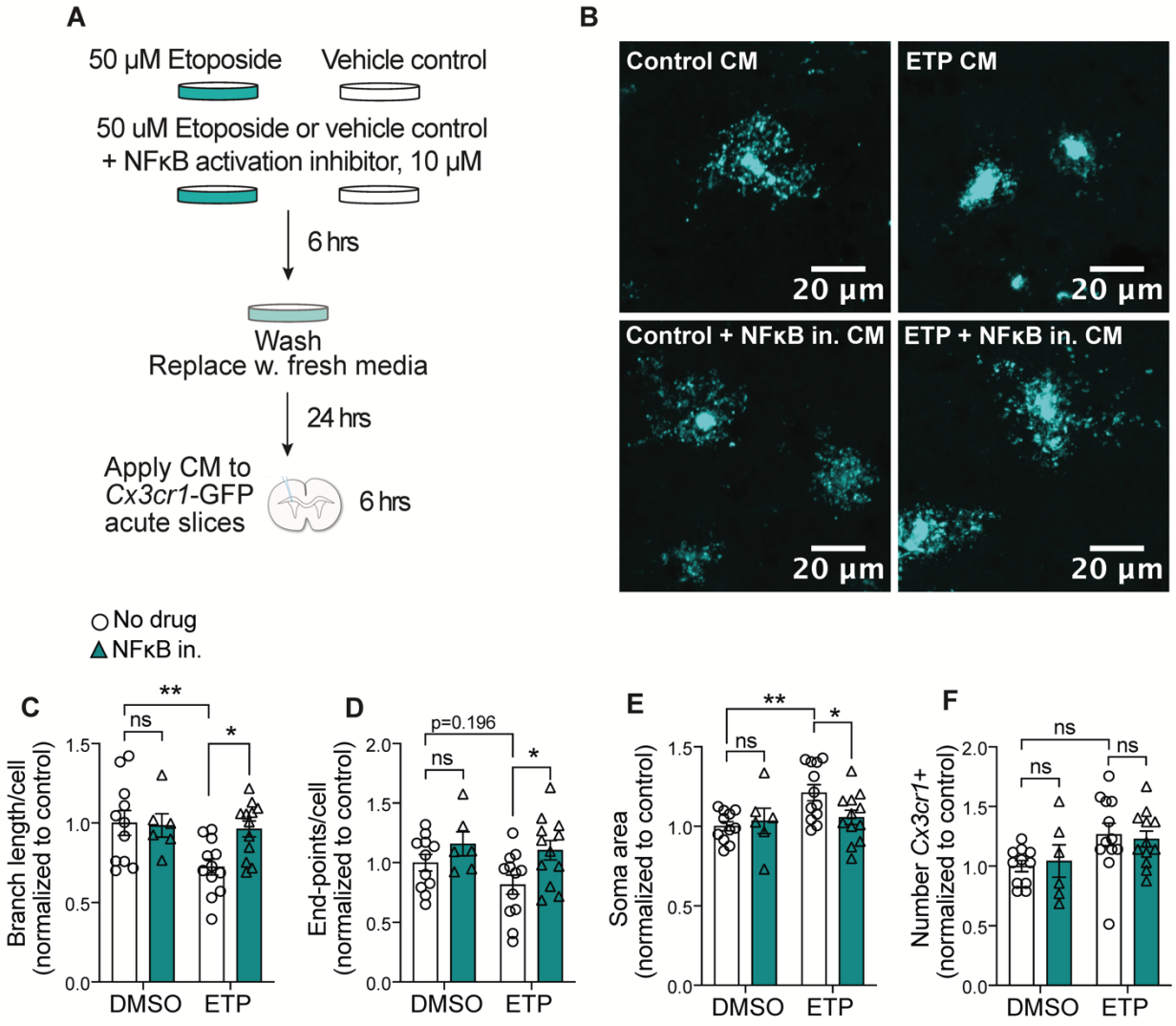

Figure 2-54 Microglia respond to conditioned media from etoposide-treated primary neurons. (**A**) Schematic for treating acute *Cx3cr1*-GFP slices with conditioned media from ETP-treated primary neurons. Cultures were treated with 50µM ETP or vehicle control (DMSO) ± 10µM NF-kappaB Activation Inhibitor VI (IKK2 inhibitor) for six hours. Cultures were washed with PBS and media was replaced. After 24 hours, media was applied to acute *Cx3cr1*-GFP slices for 6 hours. (**B**) Representative images of GFP in *Cx3cr1*-GFP acute slices treated with conditioned media. (**C-F**) Quantification of branch length (**C**), end-points (**D**), and soma area per microglia (**E**), and number of microglia per image (**F**). Each data point represents the average of two images in one acute slice. Error bars represent standard error of mean (S.E.M.); **P<0.01, *P<0.05, n.s. not significant. Two-way ANOVA followed by Sidak's test for multiple comparisons (C-F). Data are combined from two independent experiments (C-F).

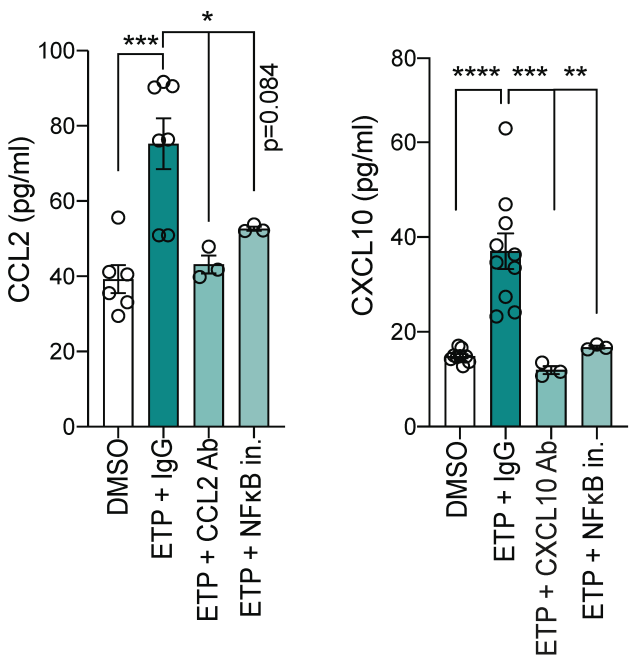

Figure 2-55 CCL2 and CXCL10 are enriched in the conditioned media of etoposide-treated primary neurons. Quantification of CCL2 (left) and CXCL10 (right) from conditioned media from control and etoposide-treated primary neurons. Each data point represents one biological replicate. Error bars represent standard error of mean (S.E.M.); ****P<0.0001, ***P<0.001, **P<0.01, *P<0.05. One-way ANOVA followed by Tukey's test for multiple comparisons. Data are combined from three independent experiments.

To determine if they played a role in DSB-mediated microglia activation, we immunodepleted CCL2 or CXCL10 from conditioned media (Figure 2-55, Figure 2-56.A). Both CCL2 and CXCL10 depletion increased branch length and end-points per microglia compared to IgG control (Figure 2-56.B-D). Interestingly, CCL2 depletion reduced microglia soma area, but CXCL10 depletion did not (Figure 2-56.E). Neither immunodepletion had an effect on microglia number (Figure 2-56.F). Combined, this suggests that while both CCL2 and CXCL10 elicit morphological changes in microglia, they may play differential roles in microglia recruitment and activation. Notably, both CCL2 and CXCL10 are upregulated in aging and AD pathogenesis (213,214), suggesting their signaling activity via DSB-

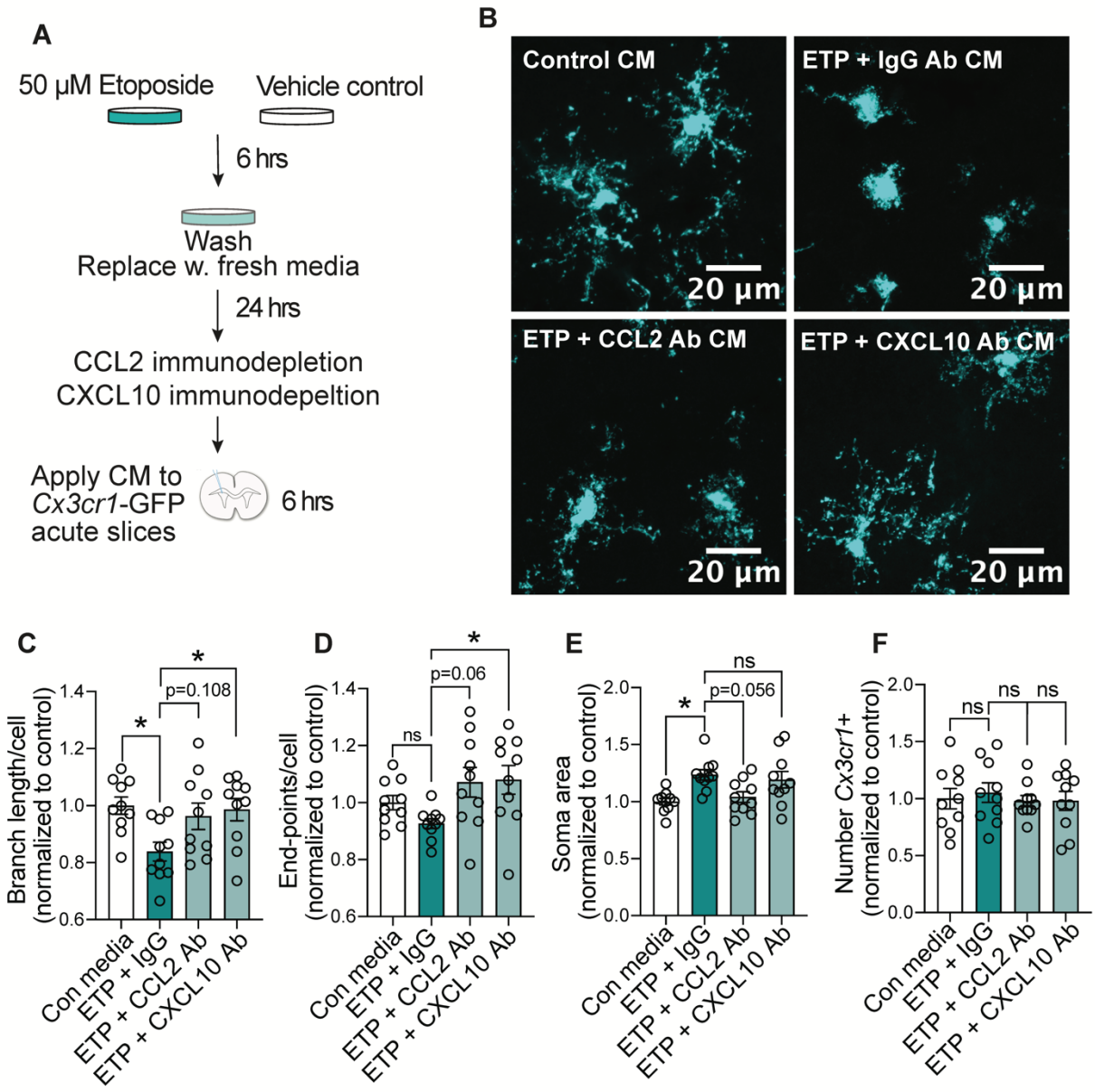

Figure 2-56 Microglia activate in response to CCL2 and CXCL10 in conditioned media from etoposide-treated primary neurons. (**A**) Schematic of ETP conditioned media experiment. Primary neurons were treated with either ETP or DMSO for 6 hours, washed with PBS, then media was replaced. Cultures recovered for 24 hours before conditioned media was collected. IgG, CCL2, or CXCL10 antibodies were used to immunodeplete conditioned media before they were applied to Cx3cr1-GFP acute slices for 6 hours. (**B**) Representative images of microglia from acute slices treated with different conditioned media. (**C-F**) Quantification of (**C**) branch length (**D**) end-points, and soma area per microglia (**E**), and number of microglia per image (**F**). Each data point represents the average of two images in one acute slice. Error bars represent standard error of mean (S.E.M.); *P<0.05, n.s. not significant. One-way ANOVA followed by Tukey's test for multiple comparisons (C-F). Data are combined from two independent experiments (C-F).

bearing neurons could play significant roles in neuroinflammation. Together, our data indicate CCL2 and CXCL10 play important roles in recruiting and activating microglia to neurons burdened with DSBs. This establishes a novel role for neuronal communication with microglia in the context of age-associated neurodegenerative disease, and uncovers a new facet of DSB toxicity in mature postmitotic neurons.

2.3 Materials and Methods

2.3.1 Fluorescence-activated nuclei sorting

Frozen cortices were disrupted with a handheld homogenizer in ice-cold PBS with protease inhibitors (cat no. 11836170001, Roche, Basel Switzerland) and RNAse inhibitors (cat no. EO0382, Thermo Fisher Scientific, Waltham MA). Samples were fixed with 1% paraformaldehyde for 10 minutes at room temperature, then quenched with 2.5M glycine for 5 minutes. Nuclei were isolated through dounce-homogenization followed by filtration with a 70μM cell strainer (cat no. 21008-952, VWR, Radnor PA). The following antibodies were used to tag nuclei: anti-H2A.X-Phosphorylated (Ser139) antibody conjugated to APC (cat no. 613416, BioLegend, San Diego CA), anti-ATM-phospho (Ser1981), antibody conjugated to PE (cat no. 651203 , BioLegend, San Diego CA), anti-NeuN antibody conjugated to Alexa Fluor 488 (cat no. MAB377X, EMD Millipore, Burlington MA), anti-PU.1 antibody conjugated to Alexa 647 (cat no. 2240S, Cell Signaling Technology, Danvers MA), anti-RFP antibody (cat no. 600-401-379, Rockland Antibodies and Assays, Gilbertsville, PA), and anti-CaMKII-α (6G9) antibody (cat no. 50049S, Cell signaling Technology, Danvers MA) . Antibodies were incubated with nuclei in 1% BSA/PBS at 4°C for one hour or overnight. For non-conjugated antibodies, samples were washed once with 1% BSA/PBS, then resuspended with 1:1000 Alexa Fluor secondary antibody (Thermo Fisher Scientific, Waltham MA) for one hour at 4ºC. Samples were passed through a 40μM filter (21008-949, VWR) and stained with DAPI (cat no. D9542, Sigma Aldrich, St. Louis MO) before sorting. Sorting was performed on a

FACSAria at the Koch Institute Flow Cytometry Core (BD Biosciences, US). At least 50,000 nuclei of each cell type was collected for RNA-sequencing. Nuclei were sorted into 1% BSA/PBS, then spun at 2kG for 15 minutes in a cooled centrifuge (cat no. 97058-916, Epindorf North America) for downstream analysis. For single-nucleus RNA-sequencing, nuclei were not fixed. Single nuclei were sorted into a 96-well plate then transported immediately to the MIT BioMicro Center for library preparation. 48 nuclei were sorted for each gated CK-p25 population per mouse, and 32 nuclei were sorted for each gated CK population per mouse. Flow cytometry analysis was performed using FlowJo software (Ashland, OR).

2.3.2 Bulk RNA sequencing

For bulk RNA-sequencing of sorted nuclei, samples were treated for 15 minutes with Proteinase K at 50°C and then for 13 minutes at 80°C. RNA was extracted using Direct-zol RNA MicroPrep kit according to manufacturer's instructions (cat no. R2062, Zymo Research, Irvine CA). Purified RNA samples underwent fragment analysis at the MIT BioMicro Center. Libraries were generated from samples passing quality control (DV200 < 50%). Library generation was performed using the SMARTer Stranded Total RNA-Seq Kit v2 - Pico Input Mammalian (cat no. 634412, Takara Bio Inc), then submitted to the MIT BioMicro Center for quality control (fragment analysis and qPCR), followed by sequencing. Paired-end sequencing was performed using the Illumina NextSeq500 platform according to standard operating procedures.

For bulk RNA-sequencing of etoposide-treated primary neurons, cultures were collected in Trizol LS (cat no. 10296028, Thermo Fisher Scientific, Waltham MA). mRNA was purified and extracted using Direct-zol RNA MicroPrep kit according to manufacturer's instructions. RNA was submitted to the MIT BioMicro Center for library preparation and sequencing. Libraries were prepared using NEBNext® Ultra™ II RNA Library Prep Kit for Illumina® (cat no. E7770, New England Biolabs, Ipswich MA). Single-end sequencing was performed using the Illumina NextSeq500 platform according to standard operating

procedures.

2.3.3 Mouse bulk RNA-seq read cleaning and bulk RNA-seq pipeline

For the paired-end fastq files, the first three nucleotides were trimmed off the second sequencing read using cutadapt version 1.16. TrimGalore version 0.4.5 was used in paired mode to trim adapters and low-quality portions of reads. Reads were aligned using Salmon version 0.12.0 to mouse genome version GRCm38.94 and human genome version GRCh38.94. For downstream analysis, TPM files from Salmon were imported into R version 3.6.1 using tximport version 1.14.0 with the option to generate estimated counts using abundance estimates scaled up to library size, and additionally scaled using the average transcript length over samples and the library size (countsFromAbundance = lengthScaledTPM).

2.3.4 Mouse bulk RNA-seq differential analysis

We performed differential analysis using R version 3.6.1 and DESeq2 version 1.26.0. For each corresponding cell type and condition, we performed differential expression using only the corresponding samples. Genes were categorized as significant if they met the cutoff threshold ($\log_2$ fold change $\geq |1.0|$, adjusted p-value < 0.05).

2.3.5 Mouse bulk RNA-seq gene set enrichment analysis

We used the complete set of RNA-Seq results for each differential analysis for downstream GSEA processing. Genes for which adjusted p-value could not be calculated were excluded. We ran GSEA version 3.0 in ranked list mode with default settings. The gene ontology biological pathways gene sets from Molecular Signatures Database v7.3 (MSigDB) were used for analysis. Genes were ranked by the sign of the fold change times the negative base 10 log of the adjusted p-value.

2.3.6 Enrichr

Significantly upregulated genes from the Stage 2 vs. Baseline contrast were filtered based on their occupation in MSigDB gene ontology biological processes containing the keyword “immune.” This

resulted in a Stage 2 immune module comprised of 940 genes. The corresponding Entrez gene symbols were then entered in to the Enrichr website: https://maayanlab.cloud/Enrichr/#. The resulting transcription factor enrichment data were downloaded as tables from the following transcription factor libraries: ChEA 2016, ENCODE and ChEA Consensus TFs from ChIP-X, TRRUST Transcription Factors 2019, Enrichr Submission TF-Gene Coocurrence, TRANSFAC and JASPAR PWMs, and ENCODE TF ChIP-seq 2015. These data are available in Table A1. More information about the Enrichr libraries can be accessed on the Enrichr website.

2.3.7 Smart-seq pipeline

SMART-seq2: Single nuclei library preparation was performed by the MIT BioMicro Center using the SMART-Seq® v4 Ultra® Low Input RNA Kit for Sequencing (Takara Bio Inc) according to manufacturer's instruction. Libraries were sequenced on a MiSeq Illumina sequencer according to standard operating procedures.

Read processing: We aligned 40-bp paired-end reads to the mm10 genome for each of 1,357 single nuclei from 12 mice (64 cells each for 6 CK controls and an average of 162 cells in each of 6 CKp25 mice) using bwa mem (options: -k 15 -M) and filtered out improperly aligned reads and secondary alignments with samtools (options: -f 3 -F 1280). We ran HTSeq-count10 on each cell's filtered bam file to compute the cell's transcriptomic coverage over each gene's exons in vM25 GENCODE gene annotation.

Transgene detection: We first aligned 40-bp single-end reads from each sequenced single nucleus separately with the STAR aligner6 against the b37 genome with decoy contigs using a two pass alignment (options: --outFilterMultimapNmax 20 --alignSJoverhangMin 8 --alignSJDBoverhangMin 1 --alignIntronMin 20 --alignIntronMax 1000000). We then used Picard tools7 to revert and merge the alignment with unaligned reads and marked duplicates on the merged bam file. We identified and removed alignments on decoy contigs, sorted and fixed NM, MD, and UQ tags with Picard tools, filtered duplicates,

unmapped, and non-primary alignment reads, and split reads by Ns in their CIGAR string.

2.3.8 Cell type annotation

Cell identities: We used SCANPY11 to process and cluster the expression profiles and infer cell identities. We kept only 21,859 protein coding genes detected in at least 3 cells and filtered out 349 cells with less than 100 expressed genes, leaving 1,008 cells over the 12 mice. We used the filtered dataset to calculate the low dimensional embedding of the cells (UMAP) from the log1p matrix PCA with k=50 and nearest neighbor graph with N=20 (UMAP default parameters, min_dist=0.2), and clustered it with Leiden clustering (resolution=2), giving 17 preliminary clusters. We then manually assigned clusters based on the following 2-3 major marker genes per class: Excitatory neurons: *Camk2a*, *Gria2*, *Syt1*; Inhibitory neurons: *Gad1*, *Gad2*; Astrocytes: *Gfap*; Microglia: *Cd33*, *Csf1r*; Oligodendrocytes: *Plp1*, *Mbp*; Oligodendrocyte progenitor cells (OPCs): *Bcan*; Stage 2: *Cdkn1a*, *Ubb*. We merged clusters sharing marker genes to obtain 7 final clusters, defining two broad neuronal subtypes (484 excitatory and 108 inhibitory cells), three glial clusters (50 microglia, 131 oligodendrocytes, and 33 OPCs), 179 Stage 2 cells, and 23 cells with both high read counts and broad, non-specific marker gene expression, likely due to doublets or other sorting artifacts. The doublet cluster was removed from downstream analyses. We also identified a cluster of cells that expressed fewer than 500 genes and had high expression of mitochondrial genes. Due to the questionable quality of these cells, this cluster was also removed from downstream analysis. We further sub-annotated neuronal subtypes from neuronal clusters with distinctive expression in the original Leiden clustering, resulting in four excitatory subclusters (314 Ex0, 91 Ex1, 32 Ex2, and 47 Ex3 neurons) and two inhibitory subclusters (71 In0 and 37 In1 neurons).

Signature analysis on single-cells: For each signature, a joint expression value was calculated as the number of reads per 10k reads in each cell coming from all of the signature's genes (genes with adjusted p-values < 0.05). Signature expression was transformed by log1p and averaged across all cells in a given

neuronal subtype and mouse to obtain average signature values for plotting. We used two-sided t-tests to compare the signature expression levels of pairs of excitatory neuronal subtypes (Figure 2-18).

2.3.9 Trajectory analysis

We performed pseudotime analysis using Monocle3 (v0.2.3.0) on the *in silico* Ex0, Ex1, Ex2, Ex3, and Stage 2 neuronal populations. We normalized total counts per cell in the read count matrix to the median number of counts, log1p transformed the matrix, and regressed out the counts per gene using Monocle. We clustered the subsetted data in a new UMAP, clustered cells, learned a trajectory graph, and ordered cells by choosing the initial node as the Ex0 end of the graph to get a pseudotime across the graph. We plotted the log1p read counts across the gene set as well as the generalized additive model (GAM) smoothed fits of each signature's per-cell expression values across pseudotime (Figure 2-6).

2.3.10 Human snRNA-seq analysis

Single-nucleus transcriptomic sequencing data from postmortem cortical samples (prefrontal cortex, Brodmann area 10) of 48 subjects with varying levels of AD pathology was obtained from Mathys et al., 2019 (208). Individual-level cell type expression profiles were computed by averaging for each individual the normalized gene-expression profiles across cells of the same cell type. Average profiles were subsequently mean-centered and scaled to compute gene-wise correlation coefficients of gene expression versus individual-level measures of global AD pathology burden reported as part of the ROSMAP cohort. Briefly, global burden of AD pathology is a quantitative summary of AD pathology derived from counts of three AD pathologies: neuritic plaques (n), diffuse plaques (d), and neurofibrillary tangles (nft), as determined by microscopic examination of silver-stained slides (208).

Global consistency between gene signatures observed in CKp25 mice and a neuronal-specific association between gene expression and AD pathology in human tissue was assessed statistically using a nonparametric resampling test. To test whether cell-type specific expression of CKp25 Stage 2 signature

genes tends to correlate with pathology in the human brain, a z-score statistic was computed to quantify the deviation of their correlation coefficient rank scores, relative to random expectation. Expected scores were estimated by randomly sampling same-sized gene sets (n = 1,000 replicates). This analysis was performed for excitatory neurons, inhibitory neurons, and microglia cells independently.

2.3.11 Stage 1 and 2 signature generation

Stage 1 and Stage 2 gene signatures were curated by performing differential expression analysis on the CK-p25 bulk RNA-seq dataset. Stage 1 vs Baseline provided the genes for the Stage 1 signature, and Stage 2 vs Baseline provided the genes for the Stage 2 signature. Only genes which met the cutoff threshold ($\log_2$ fold change $\geq |1.0|$, adjusted p-value < 0.05) were retained.

2.3.12 Visium spatial transcriptomics library generation

Mice were transcardially perfused with ice-cold saline, then brains were dissected and flash frozen in OCT. A cryostat was used to generate 10μM coronal sections of the hippocampus. These sections were applied to 10X Visium Spatial Gene Expression slides. Sections were immunostained with γH2AX and DAPI following manufacturer's instructions. Sectioning and staining was performed at the MIT Hope Babette Tang (1983) Histology Core Facility. Sections were imaged immediately after staining using a Olympus FV1200 Laser Scanning Confocal Microscope at the MIT Microscopy Core Facility. Sections were then used to generate 10X Visium Spatial Gene Expression Libraries according to manufacturer's instructions at the MIT BioMicro Center. Libraries were sequenced on a NovaSeq6000 Illumina sequencer according to standard operating procedures.

2.3.13 Visium spatial transcriptomics data processing

Samples were processed using Scanpy 1.7.2. The 7 sample data matrices were merged into one matrix which was then processed. The sample id and location of each capture area of the resulting matrix were saved and used for visualization. Counts were normalized (total count of 10,000 per capture area) and

logarithmized (using Scanpy's log1p function). The resulting counts matrix, called raw normalized was used for expression visualization and differential expression analysis. For dimension resolution purposes, the raw normalized matrix was further processed: genes that were not characterized as highly variable enough were filtered out (minimum mean of 0.0125, max mean of 3, minimum dispersion of 0.5), and linear regression was performed to eliminate the effect of covariates (total_counts, and mitochondrial genes percentage). The data was then scaled (standard scaling, max value of 10). Afterwards, PCA was performed, as well as sample-level batch correction, using Harmony. Then, a knn network was constructed for the creation of a UMAP embedding. Clusters were discovered using the Leiden algorithm.

2.3.14 Visium immunohistochemistry image processing

Immunostaining images were first processed as shades of gray pictures. The largest autofluorescence artifacts were removed manually. The signal was then amplified and cleaned using a 85% contrast increase on each image.

As the immunochemistry images of the tissue align perfectly to the pictures taken for 10X Visium purposes, calibration was performed to reconstruct the capture areas grid on the immunostaining images. In that image, for each capture area, the mean signal within a circle maximizing image coverage is calculated, and recorded as the DNA damage signal. After standard scaling of this variable, a threshold of 0.4 standard deviation was set, to assign a capture areas as positive or negative for DNA damage.

2.3.15 Visium differential expression reactive microglia signature analysis

Differential expression analysis was performed using Wilcoxon rank sum test, and the resulting p-values were corrected using Benjamini-Hochberg FDR correction. For GSEA, the package gseapy was used, with 100 permutation and the signal-to-noise method. As input, the raw normalized matrix was used, though only containing the genes considered as highly variable in the dataset.

2.3.16 RT-qPCR

RNA was extracted from primary tissue cultures using the RNeasy Plus mini kit (cat no. 74136, Qiagen, Hilden Germany). Reverse transcription was performed using Invitrogen SuperScript IV First Strand Synthesis System with Oligo dT primers according to the manufacturer's protocol (cat no. 18091050, Thermo Fisher Scientific, Waltham MA). cDNA was quantified with a NanoDrop spectrophotometer. qPCR was performed using a Bio-Rad CFX-96 quantitative thermal cycler (cat no. 1855195, Bio-Rad, Hercules CA) and SsoFast EvaGreen Supermix (cat no. 1725202, Bio-Rad, Hercules CA). Relative changes in gene expression were determined using the $2^{-\Delta\Delta Ct}$ method. Cycle numbers for the gene *Gapdh* or *Rpl11* were used for housekeeping Ct values.

2.3.17 Immunofluorescent microscopy

Mice were transcardially perfused with ice-cold PBS, then fixed with ice-cold 4% paraformaldehyde in PBS. Dissected brains were drop-fixed overnight in 4% paraformaldehyde in PBS at 4°C. Forebrains were sectioned with a vibrating microtome (Leica BioSystems, Wetzlar Germany) to generate 40µM coronal slices. Slices were blocked for two hours at room temperature in blocking buffer (10% NGS, 0.3% Triton X-100, PBS), then incubated with primary antibody overnight at 4°C. Slices were washed 3 x 10 minutes with PBS, and Alexa Fluor Secondary antibodies (Thermo Fisher Scientific) were added at a 1:1000 dilution for 1 hour at room temperature. Slices were washed again 3 x 10 minutes with PBS, then stained with DAPI (cat no. D9542, Sigma Aldrich, St. Louis MO) and mounted onto Fisherbrand™ Superfrost™ Plus Microscope Slides (cat no. 12-550-15, Thermo Fisher Scientific, Waltham MA) with Fluoromount-G™ Slide Mounting Medium (cat no. 100502-406, VWR, Radnor PA).

Primary neurons cultured on cover glass (cat no. 194310012A, VWR, Radnor PA) were washed once with PBS, then fixed with 4% paraformaldehyde/PBS for 15 minutes at room temperature. Immunostaining proceeded as described.

Free-floating 40μM sections from postmortem human brain was blocked for 1 hour at room temperature in blocking buffer before being incubated in primary antibodies for 72 hours at 4ºC with gentle rocking in blocking buffer (Anti-NeuN, Synaptic Systems cat no. 266 004, 1:500; Anti-phospho-Histone H2A.X, Millipore cat no. 05-636, 1:100; Anti-NFκB p65 Invitrogen cat no. 51-0500, 1:300). Samples were then rinsed three times in 1xPBS for 5 minutes and incubated in secondary antibodies (Alexa Fluor-488, 594 or 647, ThermoFisher Scientific; 1:1000) for 2 hours at room temperature. After 1x PBS rinse, samples were incubated in 1:10,000 Hoechst in PBS (Invitrogen cat no. H3569) followed by 2 minutes in TrueBlack Lipofuscin Autofluorescence Quencher (Biotium cat no. 23007) with 3 subsequent 1x PBS rinses before mounting and imaging.

Mounted samples were imaged with a Zeiss LSM 710 confocal microscope. Images were quantified using ImageJ (NIH Image Analysis) and Imaris (Oxford Instruments). Image analysis was blinded for images from Figures 2-19, 2-21, 2-23, and Figures A4, A10-12. Number of slices and images taken for each experiment are described in figure legends. For PHP.eb AAV shp65-RFP cell-type analysis, 40μM coronal brain sections were stained for RFP and either NeuN, Iba1, GFAP, or Olig2. First, RFP-positive cells were identified in each image. Then, the percent of RFP-positive cells that also had positive immunoreactivity for a given cell-type marker was quantified. Amyloid beta and pTau181 intensity were calculated using Imaris software (Oxford Instruments, UK).

2.3.18 Antibodies for immunofluorescent microscopy in mouse

(Antibody; Manufacturer; Catalog #; Dilution) (Anti-phospho-Histone H2A.X (Ser139) Antibody, clone JBW301; EMD Millipore; 05-636; 1:500) (NeuN; Synaptic Systems; 266 004; 1:1000) (CaMKII-α (6G9) Mouse mAb; Cell Signaling Technologies; 50049S; 1:200) (NEUROD1 Polyclonal antibody; Proteintech; 12081-1-AP; 1:200) (Anti-GFP antibody; Abcam; ab13970; 1:500) (Iba1; Synaptic Systems; 234 004; 1:1000) (Anti-GFAP antibody; Abcam; ab53554; 1:500) (Recombinant Anti-Olig2 antibody [EPR2673];

Abcam; ab109186; 1:500) (RFP Antibody Pre-adsorbed; Fisher Scientific; 600-401-379; 1:200) (NF-κB p65 (D14E12) XP® Rabbit mAb; Cell Signaling Technologies; 8242S; 1:500) (NFkB p65 Polyclonal Antibody; Invitrogen; 51-0500; 1:100) (Anti-MHC class II (I-A/I-E), clone M5/114; EMD Millipore; MABF33; 1:500) (Anti-Nestin antibody [Rat 401]; Abcam; ab6142; 1:1000) (Anti-C1q antibody [4.8]; Abcam; ab182451; 1:500) (Synapsin 2 antibody (guinea pig); Synaptic Systems; 106 004 ; 1:500) (VGlut1 (rabbit); Synaptic Systems; 135 303; 1:500) (Purified anti-mouse/rat β-Amyloid Antibody; BioLegend; 805801; 1:500) (Phospho Tau (Thr181) (D9F4G) Rabbit mAb; Cell Signaling Technologies; 12885S; 1:500)

2.3.19 Primary neuron culture

Cortices were dissected from E15 Swiss-Webster embryos in ice-cold HBSS (cat no. 14175103, Thermo Fisher Scientific, Waltham MA) and dissociated with papain (cat no. LS003126, Worthington Biochemical Corp., Lakewood NJ) and DNAse I (cat no. 10104159001, Roche, Basel Switzerland). Cells were resuspended in plating media (Neurobasal media (cat no. 21103049, Thermo Fisher Scientific, Waltham MA), 1% Penicillin/Streptomycin Solution (cat no. 400-109, Gemini Bio-Products, Sacramento CA), 10% FBS)) and filtered through a 100μM cell strainer (cat no. 21008-950, VWR, Radnor PA). Cell density was quantified using a Countess II Automated Cell Counter (cat no. AMQAX1000, Thermo Fisher Scientific, Waltham MA), then plated on poly-D-Lysine-coated 12-well culture dishes, 0.5 x 10^6. Cultures were maintained in 5% CO2 at 37 °C in a cell culture incubator. After allowing four hours for the cells to adhere to the plate, the media was replaced and maintained with neurobasal media supplemented with B-27 (cat no. 17504-044, Invitrogen, Carlsbad CA), 1% Penicillin/Streptomycin, and 1% GlutaMAX Supplement (cat no. 35050-079, Thermo Fisher Scientific, Waltham MA).

We also performed cell type immunostaining analysis to assess the cell type composition of our primary cultures. 82.87% of cells were identified as mature neurons (NeuN expression), and another

9.31% were neural precursor cells (Nestin expression) (Figure 2-24). A trace number of cells were also identified as astrocytes (GFAP expression, 2.46%) and oligodendroglia (Olig2 expression without Nestin expression, 1.35%) (Figure 2-24).

2.3.20 Primary neuron treatments

Etoposide: Primary cortical neuron cultures (DIV11-13) were treated with 50μM etoposide prepared from 20mM stock (cat no. E1383-250MG, Sigma, St. Louis MO). Cultures were treated for 6 hours before collection for downstream experiments. Quantitative reverse transcription PCR (RT-qPCR) was used to measure gene expression. We were also able to observe increased expression of nuclear p65 and immune genes in primary neuron cultures treated with 25μM etoposide.

X-ray irradiation: Primary cortical neurons (DIV11-13) were exposed to 10 Gy or 0 Gy X-ray irradiation using the X-Rad320 from Precision X-Ray. Cultures were given 24 hours to recover before proceeding with experiments.

NFκB activation inhibitor: Primary neuron cultures were treated with 10μM NFκB Activation Inhibitor VI, benzoxathiole compound from Abcam (cat no. ab145954). Cultures were pre-treated for at least 30 minutes before ETP exposure.

2.3.21 RNAScope in-situ hybridization

Fluorescent in-situ hybridization was performed using the RNAscope® Multiplex Fluorescent Reagent Kit v2 according to manufacturer's instructions (cat no. 323100, Advanced Cell Diagnostics, Newark CA). Probes targeting murine *Ccl2* (cat no. 311791), *Cxcl10* (cat no. 408921), *Aif1*-C2 (cat no. 319141-C2), *Olig2*-C3 (cat no. 447091-C3), *GFAP*-C3 (cat no. 313211-C3), and *Rbfox3*-C2 (cat no. 313311-C2) were purchased from Advanced Cell Diagnostics. Following the RNAscope protocol, slices were stained for γH2AX (cat no. 05-636, EMD Millipore, Burlington MA). Samples were imaged with a Zeiss LSM 710 confocal microscope at 40x objective. Images were analyzed with ImageJ.

2.3.22 RNAscope analysis

ImageJ version 2.1.0 thresholding was used to identify γH2AX+ nuclei and generate ROIs. Process -> "Find Maxima" was used to count mRNA puncta within ROIs. Prominence >100.00 with "Strict" setting. The number of γH2AX+ nuclei with 2≤ maxima were quantified, as well as the number of maxima per γH2AX+ nucleus. γH2AX- nuclei were identified by thresholding for individual nuclei using the DAPI channel, then excluding ROIs that overlapped with γH2AX+ ROIs. Individual nuclei were identified following the Nuclei Watershed Separation process described on the ImageJ website: https://imagej.net/imaging/watershed

2.3.23 Brain tissue samples

MADRC brain tissue samples: Fresh frozen postmortem brain samples were generously provided by the Massachusetts Alzheimer's Disease Research Center. These samples were used for bulk RNA-sequencing. Individuals were selected based on clinical diagnosis and Braak score. The three samples labeled as AD all had a clinical diagnosis of AD, and a Braak score of VI. The three samples labeled as non-AD did not have a clinical diagnosis of AD, and had Braak scores of I, II and II. Sample metadata is available in Table A3.

ROSMAP brain tissue samples: Fixed frozen postmortem brain samples were chosen from the Religious Orders Study and Memory and Aging Project cohort (ROSMAP). ROSMAP is a longitudinal cohort study of ageing and dementia in elderly nuns, brothers and priests. Sample metadata is available in Table A4. In-depth description of metadata variables are available at the Rush Alzheimer's Disease Center (RADC) website: https://www.radc.rush.edu/docs/var/variables.htm.

2.3.24 P65 knock-down

Custom p65 and scramble shRNA oligos cloned into an AAV backbone (pAV-U6-RFP) were purchased from ViGene Biosciences (Rockville, MD). P65 shRNA sequences were:

1. GATCCGGCAGGCTATCAGTCAGCGCATTGTGCTTATG
   CGCTGACTGATAGCCTGCTTTTTA
2. GATCCGCGGATTGAGGAGAAACGTAAATGTGCTTTTTA
   CGTTTCTCCTCAATCCGTTTTTA
3. GATCCGCACCATCAACTATGATGAGTTTGTGCTTAACT
   CATCATAGTTGATGGTGTTTTTA
4. GATCCGCCTGAGGCTATAACTCGCCTATGTGCTTTAGG
   CGAGTTATAGCCTCAGGTTTTTA
5. shRNA scramble: GATCCGCAACAAGATGAAGAGCACCAACTCGAGTTGG
   TGCTCTTCATCTTGTTGTTTTTA

P65 knockdown was confirmed via RT-qPCR in-house. PHP.eB AAV was generated by Janelia Viral Services. PHP.eB AAV shRNA or PBS was delivered retro-orbitally to anesthetized CK-p25 mice, 2 x 10^{11} IU/ml. For neuron-specific knockdown of p65, the plasmid SIN40C.SFFV.dTomato.miR30n (a gift from Dirk Heckl; Addgene plasmid # 169277) was modified with a hSyn, a neuron-specific promoter, then cloned into an AAV backbone for generation of PHP.eB AAV.

Mir30-based p65 shRNA:

AGCGAGCCTCATCCACATGAACTTGTTAGTGAAGCCACAGATGTAACAAGTTCATGTGGAT
GAGGCC

Mir30-based scramble:

AGCGCCCTAAGGTTAAGTCGCCCTCGTAGTGAAGCCACAGATGTACGAGGGCGACTTAACC
TTAGGA

Mice received bilateral intracranial injections (-2.00 AP, 1.5 ML, -0.5 DV) of 500nL of AAV-PHP.eb-hSyn-RFP-mir30-shp65 or AAV-PHP.eb-hSyn-RFP-mir30-scramble at a rate of 100nL per minute (both 2 x 10^{11} IU/ml). Two weeks after injection, mice were induced by removing doxycycline diet. Following induction, mice were transcardially perfused with ice-cold PBS. One hemisphere was drop-fixed overnight in 4% paraformaldehyde/PBS at 4°C for immunostaining. The other hemisphere was flash-frozen in liquid nitrogen and stored at -80°C for RNA sequencing.

2.3.25 CK-p25 mice

All mouse experiments were approved by the Committee for Animal Care of the Division of Comparative Medicine at the Massachusetts Institute of Technology (MIT), as well as the MIT Institutional Animal Care and Use Committee. All animal experiments were carried out at MIT. CK-p25 double transgenic mice were raised and maintained on a doxycycline diet. All mice were induced by removing doxycycline from their diet to drive the expression of p25-GFP in forebrain excitatory neurons. All mice were induced at 3-4 months old.

2.3.26 Conditioned media and immunodepletion

Following etoposide treatment, cultures were washed once with PBS. Cultures then recovered in fresh media for 24 hours. Media was collected and spun at 2,000g for 10 minutes to remove cellular debris. Media was stored at -80ºC for future experiments. Conditioned media from etoposide-treated neurons were incubated with IgG, Ccl2, or Cxcl10 antibodies (all 40µg/mL) for 4 hours at 4ºC. Dynabeads™ Protein G were added to pull down the antibody complex.

2.3.27 Organotypic brain slice culture

8 through 12 week-old Cx3cr1-GFP male mice were anesthetized with isoflurane and transcardially-perfused, dissected, and sliced in ice-cold NMDG-cutting solution containing (in mM): 2.5 KCl, 0.5 CaCl2, 10 MgSO4, 1.25 NaH2PO4, 20 HEPES, 2 Thiourea, 5 sodium ascorbate, 3 sodium pyruvate, 92 NMDG, 30 NaHCO3, 25 D-Glucose, pH 7.3 – 7.4 with HCl. The slicing chamber was bubbled with 95% O2/5%CO2, and coronal slices were cut at 250 µm thickness using a vibratome (Leica, VT1000s). After the last slice was collected, slices were transferred to a well-plate containing fresh aCSF and placed in an incubator set at 37°C and 95% O_2/5% CO2 for 30 minutes. The aCSF solution contained (in mM): 125 NaCl, 2.5 KCl, 1.2 NaH2PO4, 1.2 MgCl2, 2.4 CaCl2, 26 NaHCO3, 11 D-Glucose. Afterward, 100% of

aCSF was removed and a 1:1 mixture of fresh aCSF and conditioned media was added to the slices and placed back into the incubator for 6 hours. At the completion of the experiment, slices were fixed overnight at 4ºC with 4% paraformaldehyde. Slices were then incubated in 30% glucose overnight at 4ºC. Slices were sub-sectioned into 25µM slices using a cryostat, then cover-slipped for imaging.

2.3.28 ELISA

The Mouse MCP1 ELISA Kit and Mouse IP-10 ELISA Kit from Abcam (cat no. ab208979 and ab214563 respectively) were used to quantify CCL2 and CXCL10 in conditioned media from primary neurons. Assays were quantified on a plate reader and protein concentration was calculated according to manual instructions.

2.3.29 Microglia morphological analysis

Microglia morphology from CK-p25 and acute slice cultures was analyzed according to the protocol described in Young and Morrison, 2018 with minor alterations (215). Gray Scale Attribute Filtering (default settings, connectivity: 8) from the MorphoLibJ plug-in version 1.4.1 was used to reduce background noise when thresholding images for skeleton analysis. Following skeleton analysis, Morphological Filters (Operation: Opening, Element: Octagon, Radius (in pixels): 2) from MorphoLibJ was used to quantify soma area. This analysis was performed for both Iba1 and *Cx3cr1*-GFP imaging experiments.

2.3.30 Statistical methods and reproducibility

All imaging, RT-qPCR, and ELISA data was analyzed using either Student's T-test, One-Way ANOVA, Two-Way ANOVA, or Simple Linear Regression. Data was plotted and statistical tests were performed on Prism 9. Detailed statistical procedures for sequencing analysis are described in the sequencing sections of the methods.

Chapter 3

Discussion

DNA damage has long been associated with the aging brain and neurodegeneration, however the exact mechanisms by which DNA lesions drive these processes is unclear. The utilization of murine models of DNA damage and DNA break mapping techniques have allowed us to identify how DNA damage may regulate the expression of genes essential for neuronal function, and how this might lead to dysfunction later in life. While these are mechanisms specific to neurons, emerging evidence also suggests that many cell types in the brain, including astrocytes, microglia, oligodendrocytes, and neurons, may mediate the cytotoxicity of DNA damage through senescence-associated signaling. However, it remains to be seen whether DNA damage itself is the main inducer of senescence in each of these cell types. Regardless, it is clear that DNA damage can elicit neuron dysfunction broadly through two distinct mechanisms. First, the location of the lesion has a significant impact on transcriptional mechanisms required for normal cell function. Second, the downstream signaling pathways of lesion detection, whether they be through DDR or cytosolic nucleic acid sensing, can elicit apoptotic or inflammatory signaling that lead to neurotoxicity.

3.1 Summary and discussion

In this thesis, we asked if there was a the functional role for DNA damage-mediated senescence in neurons. In particular, we wanted to determine if neurons harboring DNA damage play meaningful roles in age-associated neuroinflammation and neurodegeneration. Substantial evidence supports a causal role for microglia and neuroinflammation in AD pathogenesis (197,216). For example, many AD risk genes and genomic loci are most active in microglia (122), and reactive microglia are thought to create a cytotoxic

environment for neurons and exacerbate neurodegeneration (217,218). Our results indicate that neurons participate in this inflammatory signaling as well. Specifically, upon the accumulation of DSBs, neurons are able to engage microglia through the secretion of chemotactic and pro-inflammatory factors, thus facilitating neuroinflammation and disease progression. This is a previously undefined role for neurons in the context of neurodegenerative disease, and provides a mechanistic link between genomic fragility and senescence in neurons and microglia activation (Figure 3-1).

Interestingly, the activation of inflammatory signaling in DSB-bearing neurons corresponds with a progressive erosion of cell identity. Using single-nuclei RNA-seq, we found that DSB-bearing neurons engage DNA repair and DNA synthesis pathways first (Stage 1), but transition to immune gene expression at later stages of genome toxicity (Stage 2). These Stage 2 cells are most enriched for senescent markers, such as *Cdkn1a* and *Ubb*, rather than neuronal markers. The age-dependent erosion of neuronal identity has been observed in both sporadic and familial AD patients, and coincides with the activation of a number of biological pathways identified in our study, including DNA damage response, cell-cycle re-entry, and NFκB signaling (191). Interpreted in the context of the present study, these observations suggest that the age-associated accumulation of DSBs may degrade chromatin integrity in neurons, ultimately resulting in the activation of immune signaling that engage microglia.

While we initially identified the Stage 2 gene signature in CK-p25 mice by virtue of reduced NeuN immunoreactivity in a subset of DSB-bearing neurons, we also identified Stage 2 characteristics in DSB-bearing neurons with NeuN expression, including neurons from the human postmortem brain and murine primary culture. These observations indicate that there are likely high levels of heterogeneity in the damaged neuron population, and that a simple Stage 1 vs Stage 2 dichotomy may not fully encompass all transcriptional states. However, the Stage 1 and Stage 2 populations are able to serve as proof of principle that a heterogeneous response to DSBs in neurons does exist, and that transitions between these

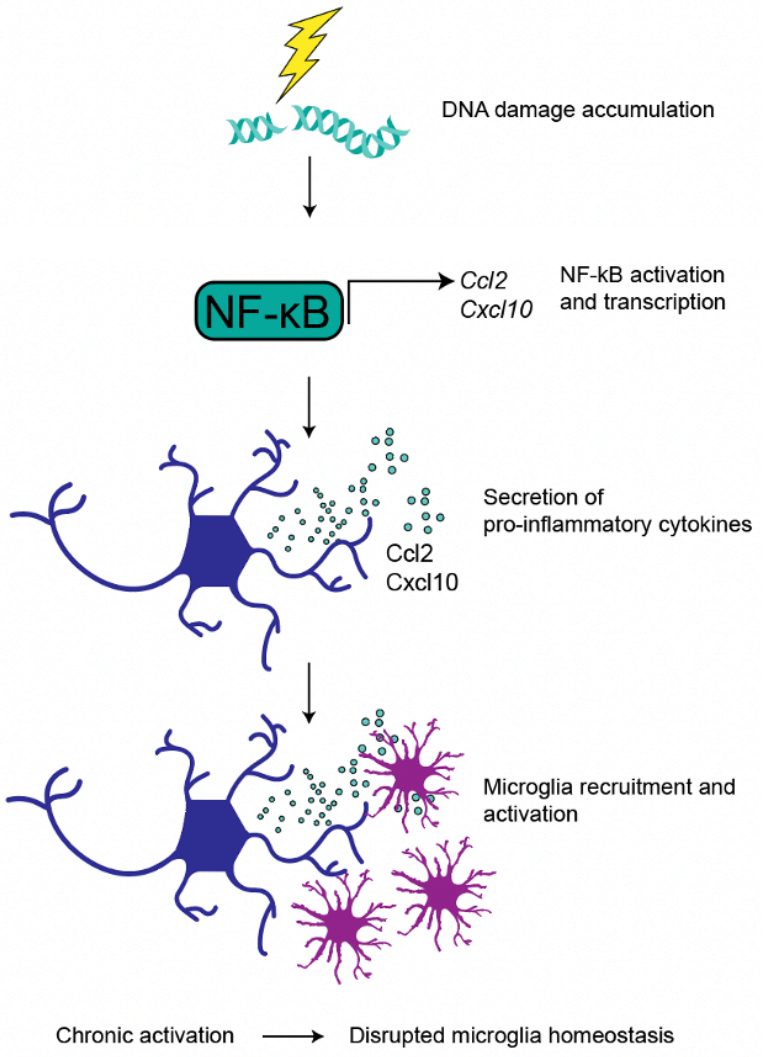

Figure 3-1 Dissertation schematic. DSB accumulation in neurons can drive the activation of NFκB, which leads to the expression of pro-inflammatory and immuno-modulatory genes. The secretion of NFκB-mediated signaling factors results in microglia recruitment, proliferation, and activation. This mechanism may important roles in neurodegenerative processes.

transcriptional states may occur during the progression of neurodegenerative disease.

The SASP and canonical antiviral response is activated through the detection of non-endogenous nucleic acids within the cytosol. Thus, it is likely that loss of nuclear and genomic integrity may lead to the release of DNA fragments in DSB-bearing neurons. In fact, we observed increased expression of nucleic acid sensors in DSB-bearing neurons, including cGAS, which plays a significant role in innate immune activation associated with senescence (142). Nevertheless, many other mechanisms may be at play, including de-repression of transposable elements (219), epigenetic drift, and ATM-mediated NFκB transcription (202). There is also evidence that nucleic acids released from mitochondria play roles in neuron immune gene expression (220). It remains to be addressed whether DSB-induced immune gene expression is a product of age-associated decline in DNA repair, or whether multiple cellular functions that are also known to decline with age engage immune signaling as a convergent mechanism of neuronal distress. Therefore, while the current thesis does not address the mechanism by which DSBs in the CK-p25 mouse activate immune gene expression, a rich foundation of evidence for DSBs activating immune gene expression through multiple pathways exists for future studies.

Our data does not exclude the possibility that other cell types in the brain are capable of initiating a SASP in response to DNA damage. Indeed, cGAS-STING-mediated senescence has also been described in ATM knockout microglia (164). Additional senescent phenotypes described in microglia (19), astrocytes (163), and OPCs (21) have also been shown to play a functional role in mouse models of neurodegenerative disease. Interestingly however, despite the fact that neurons are the brain cell type most vulnerable to DSB accumulation, few studies have examined the relationship between DNA damage and senescence in neurons. Indeed, observations of senescent neurons have been noted in other studies (168), indicating that an investigation of the effects senescent neurons in neurodegenerative disease is merited. We build upon these foundational observations by providing a detailed transcriptional analysis of such a

population of neurons, linking them to a late-stage DSB response, and mechanistically establishing their role in microglia recruitment and activation in neurodegeneration.

We identified NFκB as a major regulator of immune gene expression in DSB-bearing neurons from both CK-p25 mice, primary neurons, and postmortem human brain. In addition, we found that suppression of NFκB activity through p65 knock down or small molecule inhibition in neurons was sufficient to reduce activated microglia morphology and gene expression. NFκB has been previously identified as a therapeutic target for AD, albeit in the context of microglia and astrocytes (221). Our results now indicate that this transcription factor plays a pivotal role in DSB-bearing neurons as well. Importantly, in rodent models of learning and memory, NFκB activity in neurons is neuroprotective. Suppression of NFκB in forebrain excitatory neurons impairs spatial learning and neuronal plasticity (222), and exacerbates cell death following exposure to neurotoxic stimuli (182). Therefore, the primary role of neuronal NFκB may be to regulate synaptic processes, but it can also orchestrate immune activation in response to cell stressors. It is possible that NFκB and inflammatory activity in DSB-bearing neurons may initially function as a neuroprotective process. Indeed, while we observed a striking reduction in synaptic gene expression in Stage 1 neurons, this downregulation was virtually absent in Stage 2 neurons (Figure 2-3.A). However, we also observed a striking rescue of synaptic loss in p65kd mice at the 6-week timepoint, indicating that there is a complex relationship at play between the neuroprotective effects of NFκB and the synaptic pruning activity it may promote in microglia.

Finally, we identify CCL2 and CXCL10 as primary signaling molecules secreted from DSB-bearing neurons to recruit and activate microglia. In the CK-p25 model, DSB-bearing neurons are the first cell type to express CXCL10 and CCL2. Mainly astrocytes and microglia express these chemokines at a later time point, presumably in response to DSB-bearing neurons. Furthermore, spatial transcriptomics revealed that signatures of reactive microglia are closely associated with γH2AX+ neurons, suggesting

that DSB-bearing neurons are hubs for neuro-immune communication. Finally, immunodepletion of CCL2 or CXCL10 in conditioned media from etoposide-treated neurons was able to prevent branch shortening and end-point reduction in microglia in acute slice culture. Notably, increased levels of both of these cytokines are implicated in the pathogenesis of AD, and affect blood brain barrier permeability to aid the infiltration of peripheral monocytes (200,223). However, manipulation of either signaling axis seems to have varying effects on AD pathology. For example, CCR2 deficiency in murine models of AD aggravate amyloid pathology and cognitive decline, but CCL2 overexpression seems to also increase amyloid deposition (224–226). Another study demonstrates that deficiency of the CXCL10 receptor CXCR3 reduces amyloid deposition and behavioral deficits (227). These findings suggest that CCL2 and CXCL10 are crucial for effective microglia recruitment and activation, but imbalance in these signaling axes have detrimental effects on cognition and pathology clearance.

In summary, we leveraged bulk, single-nuclei, and spatial transcriptomic techniques in parallel with *in vitro* and *in vivo* manipulations of NFκB signaling to characterize DSB-bearing neurons and their relationship with microglia in the context of age-associated neurodegenerative disease. We demonstrate that DSB accumulation elicits senescent and antiviral-like signaling in neurons, which recruits and activates microglia in an NFκB-dependent manner. Our data posit that neurons play meaningful roles in neuroinflammation, which historically has been thought to be driven largely by glial cells. Crucially, this axis of neuron-microglia communication is mediated by DNA damage accumulation in neurons, revealing that two hallmarks of AD, genome fragility and neuroinflammation, are mechanistically linked.

3.2 Future directions

In this dissertation, we present evidence that DSB-induced immune signaling in neurons alters neuron-microglia communication. This thesis opens many doors for further investigation. First, what are the genomic loci most impacted by DSBs in Stage 1 and Stage 2 neurons? As discussed in the introduction, a

multitude of next generation sequencing techniques now exist to accurately map DNA lesions to the level of nucleotide precision (Figure 1-2). These techniques could be readily applied to mapping DSBs in Stage 1 and Stage 2 neurons. Are DSBs in damaged neurons localized to gene regulatory elements, or do they aggregate at the more macroscopic level of chromatin architecture domains? Previous work shows DSBs are generated at the promoters of immediate early genes (IEGs) in neurons following stimulation or fear learning (31,37). While these breaks were found to facilitate IEG expression, it is also known that gene expression can be subdued in response to DSBs (228,229). Would we then expect that DSBs localize to regulatory regions associated with Stage 1 and Stage 2 gene signatures (the significantly upregulated genes), or with the genes significantly downregulated in Stage 1 and Stage 2 neurons? It will be important to understand how chromatin reorganization following DSB detection alters the transcriptional landscape, and how this in turn could play a role in NFκB-mediated gene expression.

A second area ripe for further investigation is understanding the cell type vulnerability of Stage 1 and Stage 2 gene signatures. We found that γH2AX+ neurons were most dense in layers 2/3 and 6 of the CK-p25 cortex. While these densities are dictated to an extent by CamkII-directed p25 expression, it is still unclear as to why some neurons may accumulate DSBs and others may not. The wide range of activity and metabolic demands encompassed by neuronal subtypes may predispose certain populations to genomic toxicity. Notably, hyperexcitability in cortical and hippocampal circuits is a known feature of early Alzheimer's disease, bringing into question how activity-induced DSBs may drive some aspect of selective vulnerability (230). Single cell sequencing techniques are likely to play a crucial role in dissecting the differential susceptibility to lesion accumulation. For example, many neurodegenerative disease snRNA-seq datasets are now available that could be used to determine the heterogeneity of Stage 1 and Stage 2-vulnerable cell types across a wide range of disease.

In conclusion, a comprehensive map of DNA break locations in combination with a better

understanding of the subtypes of neurons subject to DSB accumulation and immune signaling will help us better pinpoint vulnerable nodes of neurodegenerative disease progression. Ultimately, this will allow us to fully realize the mechanistic role of DNA damage in age-associated neurodegenerative disease.

Appendix A: Tables

Table A1. Enrichr transcription factor analysis of Stage 2 immune genes.

Enrichr Submission TF-Gene Coocurrence

Index	Term	Overlap	P-value	Adjusted P-value	Old P-value	Old Adjusted P-value	Odds Ratio	Combined Score
1	STAT3	102/299	5.81E-87	5.00E-84	0	0	24.06179439	4777.821098
2	STAT5A	102/299	5.81E-87	5.00E-84	0	0	24.06179439	4777.821098
3	NFKB1	100/299	3.27E-84	1.87E-81	0	0	23.23849463	4467.204693
4	RELA	98/299	1.71E-81	7.37E-79	0	0	22.43716976	4172.661333
5	IRF1	96/299	8.37E-79	2.40E-76	0	0	21.65709137	3893.491958
6	TP53	96/299	8.37E-79	2.40E-76	0	0	21.65709137	3893.491958
7	STAT1	94/299	3.81E-76	8.20E-74	0	0	20.89756098	3629.028804
8	STAT6	94/299	3.81E-76	8.20E-74	0	0	20.89756098	3629.028804
9	IRF5	92/299	1.62E-73	3.09E-71	0	0	20.1579085	3378.633761
10	IRF8	91/299	3.24E-72	5.07E-70	0	0	19.79533451	3258.520096

ChEA 2016 Term

Index	Term	Overlap	P-value	Adjusted P-value	Old P-value	Old Adjusted P-value	Odds Ratio	Combined Score
1	NUCKS1 24931609 ChIP-Seq HEPATOCYTES Mouse	96/588	2.11E-49	1.36E-46	0	0	8.801807543	986.4973813
2	RELA 24523406 ChIP-Seq FIBROSARCOMA Human	120/1182	6.70E-40	2.15E-37	0	0	5.242994777	472.9277944
3	OCT4 18692474 ChIP-Seq MEFs Mouse	111/1992	3.15E-15	6.74E-13	0	0	2.558410132	85.42893836
4	TCF7 22412390 ChIP-Seq EML Mouse	108/2000	6.72E-14	1.08E-11	0	0	2.455103718	74.46663044
5	FOXO1 25302145 ChIP-Seq T-LYMPHOCYTE Mouse	106/2000	4.04E-13	4.33E-11	0	0	2.395108641	68.34868954
6	MYB 26560356 Chip-Seq TH1 Human	106/2000	4.04E-13	4.33E-11	0	0	2.395108641	68.34868954
7	NCOR 22465074 ChIP-Seq MACROPHAGES Mouse	105/2000	9.74E-13	8.93E-11	0	0	2.365371314	65.4207953
8	CLOCK 20551151 ChIP-Seq 293T Human	38/407	8.76E-12	7.03E-10	0	0	4.109351574	104.6294568
9	KDM2B 26808549 Chip-Seq SUP-B15 Human	102/2000	1.26E-11	9.01E-10	0	0	2.277184608	57.14457878
10	IRF8 27001747 Chip-Seq BMDM Mouse	101/2000	2.90E-11	1.83E-09	0	0	2.248126544	54.55038458

ENCODE and ChEA Consensus TFs from ChIP-X

Index	Term	Overlap	P-value	Adjusted P-value	Old P-value	Old Adjusted P-value	Odds Ratio	Combined Score
1	TCF3 ENCODE	61/840	2.99E-13	2.39E-11	0	0	3.211900097	92.62295084
2	RELA ENCODE	44/484	4.66E-13	2.39E-11	0	0	4.026004228	114.3209027
3	RUNX1 CHEA	79/1294	6.97E-13	2.39E-11	0	0	2.711862751	75.91212743
4	ZMIZ1 ENCODE	61/914	1.09E-11	2.80E-10	0	0	2.921654223	73.75540069
5	CEBPD ENCODE	53/734	1.52E-11	3.14E-10	0	0	3.153659679	78.54860432
6	SPI1 CHEA	66/1056	2.56E-11	4.39E-10	0	0	2.733628973	66.67267443
7	KLF4 CHEA	62/987	8.93E-11	1.31E-09	0	0	2.73381883	63.25734978
8	IRF8 CHEA	18/121	2.16E-09	2.55E-08	0	0	6.787166566	135.4321792
9	NELFE ENCODE	25/234	2.22E-09	2.55E-08	0	0	4.685980472	93.36323315
10	GATA2 CHEA	50/772	2.51E-09	2.58E-08	0	0	2.782094705	55.0988413

ARCHS4 TFs Coexpression

Index	Term	Overlap	P-value	Adjusted P-value	Old P-value	Old Adjusted P-value	Odds Ratio	Combined Score
1	PARP12 human tf ARCHS4 coexpression	58/299	5.66E-34	9.12E-31	0	0	10.08900822	772.3621127
2	IRF7 human tf ARCHS4 coexpression	56/299	5.58E-32	4.50E-29	0	0	9.61802487	692.1397043
3	STAT1 human tf ARCHS4 coexpression	55/299	5.35E-31	1.73E-28	0	0	9.386709602	654.2771359
4	IFI16 human tf ARCHS4 coexpression	55/299	5.35E-31	1.73E-28	0	0	9.386709602	654.2771359

Table A1. cont.

ARCHS4 TFs Coexpression Term

Index		Overlap	P-value	Adjusted P-value	Old P-value	Old Adjusted P-value	Odds Ratio	Combined Score
5	PLEK human tf ARCHS4 coexpression	55/299	5.35E-31	1.73E-28	0	0	9.386709602	654.2771359
6	MTF1 human tf ARCHS4 coexpression	53/299	4.57E-29	1.23E-26	0	0	8.932234721	582.8723208
7	RELB human tf ARCHS4 coexpression	51/299	3.54E-27	6.33E-25	0	0	8.488379136	516.9992714
8	ZNFX1 human tf ARCHS4 coexpression	51/299	3.54E-27	6.33E-25	0	0	8.488379136	516.9992714
9	IRF5 human tf ARCHS4 coexpression	51/299	3.54E-27	6.33E-25	0	0	8.488379136	516.9992714
10	HLX human tf ARCHS4 coexpression	50/299	2.99E-26	4.39E-24	0	0	8.270340462	486.0536426

TRRUST Transcription Factors 2019

Index	Term	Overlap	P-value	Adjusted P-value	Old P-value	Old Adjusted P-value	Odds Ratio	Combined Score
1	NFKB1 human	65/303	6.93E-41	1.68E-38	0	0	11.6282907	1075.270951
2	NFKB1 mouse	55/200	7.18E-41	1.68E-38	0	0	15.87684729	1467.574823
3	RELA human	64/301	5.22E-40	8.14E-38	0	0	11.47291847	1037.733582
4	STAT3 mouse	32/79	2.60E-30	3.04E-28	0	0	27.28457995	1858.669511
5	RELA mouse	33/121	9.10E-25	8.52E-23	0	0	15.02711777	831.8441176
6	STAT3 human	34/142	1.88E-23	1.47E-21	0	0	12.62844107	660.805807
7	SP1 human	54/472	3.14E-20	2.10E-18	0	0	5.319530418	238.8909408
8	JUN human	31/149	1.47E-19	8.62E-18	0	0	10.46793262	453.9099781
9	SP1 mouse	40/270	3.16E-19	1.64E-17	0	0	7.01959712	299.0353547
10	JUN mouse	29/131	3.64E-19	1.70E-17	0	0	11.29156622	479.4153286

TRANSFAC and JASPAR PWMs

Index	Term	Overlap	P-value	Adjusted P-value	Old P-value	Old Adjusted P-value	Odds Ratio	Combined Score
1	SND1 (human)	72/1473	1.19E-07	3.44E-05	0	0	2.088241946	33.29565742
2	NFKB1 (human)	132/3497	2.11E-06	3.05E-04	0	0	1.642250053	21.46116365
3	RELA (human)	107/2775	1.07E-05	0.001029143	0	0	1.644791933	18.82767577
4	EGR1 (human)	37/681	1.89E-05	0.001363891	0	0	2.254926889	24.52807163
5	SP1 (mouse)	90/2360	9.38E-05	0.005423768	0	0	1.598252329	14.82211744
6	ZNF281 (human)	45/986	1.64E-04	0.007895434	0	0	1.878613628	16.37425541
7	IRF8 (human)	63/1550	2.28E-04	0.009419459	0	0	1.679382845	14.08245505
8	WT1 (human)	96/2689	5.59E-04	0.020199791	0	0	1.485307144	11.12356648
9	RXRA (human)	57/1422	6.45E-04	0.020711088	0	0	1.644730053	12.08266097
10	SP1 (human)	56/1406	8.36E-04	0.022717466	0	0	1.631634932	11.56230067

TF ChIP-seq 2015

Index	Term	Overlap	P-value	Adjusted P-value	Old P-value	Old Adjusted P-value	Odds Ratio	Combined Score
1	RELA GM12892 hg19	86/1302	5.84E-16	4.75E-13	0	0	2.997469929	105.1407714
2	RELA GM19193 hg19	112/2000	1.61E-15	6.54E-13	0	0	2.577212806	87.79124916
3	STAT1 K562 hg19	38/345	5.17E-14	1.40E-11	0	0	4.955274629	151.5974794
4	STAT2 K562 hg19	31/271	4.33E-12	8.81E-10	0	0	5.114308985	133.8186108
5	EP300 CH12.LX mm9	103/2000	5.44E-12	8.86E-10	0	0	2.30641058	59.82012874
6	POLR2AphosphoS5 MEL cell line mm9	121/2661	1.86E-10	2.38E-08	0	0	2.038199913	45.6704645
7	NELFE K562 hg19	32/334	2.09E-10	2.38E-08	0	0	4.190564621	93.39730284
8	ETS1 MEL cell line mm9	95/1902	2.34E-10	2.38E-08	0	0	2.202099786	48.83317746
9	CHD1 CH12.LX mm9	98/2000	3.24E-10	2.93E-08	0	0	2.161947353	47.24237712
10	KAT2A HeLa-S3 hg19	65/1112	5.99E-10	4.88E-08	0	0	2.53218213	53.77208192

Table A2. Differentially expressed immune genes in Stage 2 neurons and their enrichment in etoposide-treated primary neurons.

gene name	stage 2 log2foldchange	stage 2 padj	etp log2FoldChange	etp padj
Cxcl12	4.68403612	3.57E-66	-1.360178292	2.57E-33
Il11	5.539044619	5.87E-50	4.294779453	4.80E-34
Lif	3.984369678	2.99E-25	2.778825942	1.12E-43
Csf1	1.7782758	2.93E-20	0.044252612	6.70E-01
Il17f	2.12121013	6.52E-15	2.606584106	0.0000321
Il21	-1.919118366	8.05E-11	5.643377765	2.41E-09
Il33	2.585358089	1.36E-09	1.329267548	5.18E-11
Tgfb2	1.80046727	4.00E-09	-0.057245884	5.80E-01
Cx3cl1	-0.746370002	4.64E-09	0.173448176	0.00000143
Cxcl10	5.38955741	6.24E-08	2.191924007	1.44E-18
Tgfb1	1.350911975	8.61E-07	0.805303536	2.06E-02
Ccl27a	-1.101204133	0.00000307	0.071237704	6.84E-01
Cxcl16	4.369063611	0.0000549	1.676601731	2.64E-14
Il18	1.663578061	0.0000606	-0.433916698	1.74E-04
Kitl	0.733572203	0.0000793	-0.873215302	4.51E-68
Cxcl14	1.155436176	0.0000866	0.110833871	5.60E-02
Il12a	2.676362206	0.000133273	0.259081058	0.61080839
Il17c	5.465079932	0.000187743	4.950177204	0.00000288
Tnfsf12	6.593030565	0.000291982	0.3696256	2.68E-01
Il17b	6.328031903	0.002544414	2.71257001	0.000101
Il1f9	-1.460268377	0.003924411	-0.118718812	0.85132262
Osm	5.785609537	0.004625064	0.88546604	0.1478131
Tnfsf13	2.575321972	0.006526708	0.264979859	0.64129084
Tnfsf10	0.97061923	0.008462517	0.55278339	0.26352284
Tnfsf13b	1.067586877	0.0094277	2.229918792	0.000000000
Ccl28	-1.233950347	0.010143161	-0.209968286	0.157918048
Il15	3.136379567	0.010226958	0.662717117	1.63E-01
Tnfsf15	-1.308990648	0.013484716	1.585164390	0.007163869
Ccl2	4.990071598	0.015749462	1.74685073	4.28E-03
Cxcl11	1.478888553	0.017414773	2.555069138	0.00117078
Il6	5.29350798	0.017594521	2.352652735	0.000001890
Ccl20	5.873979211	0.024581440	1.678629227	1.64E-02
Ifna13	5.788306959	0.030066567	0.137333164	NA

Table A2. cont.

gene name	stage 2 log2foldchange	stage 2 padj	etp log2FoldChange	etp padj
Ccl12	3.600998672	0.036632050	0.924566514	1.28E-01
Il1a	3.331461141	0.057875099	0	0.69380052
Csf3	3.605830956	0.066441243	5.349407687	0.000000000
Il7	-2.921340318	0.070323031	0	0.96205226
Tnfsf11	3.07212206	0.096094962	2.187567720	7.76E-05
Ccl6	2.036683779	1.06E-01	1.161577511	6.85E-02
Il1rn	-2.62732797	0.133611786	1.061721896	9.62E-02
Ltb	2.781935217	0.145342036	1.752666566	0.00000884
Csf2	-5.058286728	0.160080862	0.369491303	5.20E-01
Cxcl5	-1.304912409	1.76E-01	1.812004286	6.24E-08
Gm13304	3.935519843	1.84E-01	0	NA
Il34	-0.461411519	0.193828673	-0.238407198	0.16198665
Ccl21a	4.800197574	2.19E-01	0	NA
Il16	-0.47171879	2.21E-01	-0.758323152	0.0000827
Il5	2.391913905	0.233064819	4.156321133	7.59E-14
Ifna14	4.057569671	0.244043462	0	NA
Il22	3.218640253	0.312395719	3.659299876	4.51E-04
Ccl24	3.237236556	0.315896301	0.545866827	NA
Il1b	2.33821319	0.341989749	1.030095523	0.02984905
Il24	3.409567498	0.378265505	0.730630371	NA
Cxcl9	-1.005679333	0.412678143	0.245601838	0.68384528
Ccl4	1.768102866	0.436067367	2.768544935	1.77E-04
Il13	2.428533472	0.494519719	1.428289704	0.01083757
Tgfb3	0.276866326	0.511970371	-0.081411105	0.55147233
Il27	1.888924697	0.517276316	1.576098773	0.0312073
Ccl11	2.048005651	0.522837596	0.510112123	0.36312599
Ifnab	-2.311300106	0.593626188	5.666930581	1.29E-07
Il12b	-1.515285135	0.614138184	3.73423572	2.57E-04
Mydgf	0.133590817	0.6146726	-0.024227129	0.79920155
Il17d	-0.400287214	0.660025402	-0.443977197	1.72E-06
Tnf	1.079495452	0.710677531	0.609806393	NA
Ifna16	0.963735833	0.719563778	2.892717591	0.00259615
Ccl3	0.685040564	0.807129516	1.159068377	0.0445487
Ifne	-0.786722992	0.821461931	0.177619207	NA
Ccl19	0.498695238	0.833090681	0.343452401	NA
Gm13306	-0.22459991	0.856984718	0.099811543	0.84265393

Table A2. cont.

gene name	stage 2 log2foldchange	stage 2 padj	etp log2FoldChange	etp padj
Il23a	-0.161842914	0.8648379	3.568083786	1.80E-16
Ccl22	0.471472824	0.879318396	1.097678506	0.0860579
Ccl9	-0.114312162	0.884740473	0.650610507	0.15718418
Tnfsf8	0.437838533	0.90379487	1.921536624	0.0163492
Ccl17	0.212390839	0.935959159	1.940030781	5.90E-20
Ifna2	-0.077655279	0.982909126	2.159053123	0.0090488
Il4	-0.999470072	NA	-0.811049296	2.86E-11
Il31	3.758649463	NA	6.425466993	1.06E-09
Il25	2.731107014	NA	2.856145708	3.51E-08
Ifnb1	-0.999478421	NA	4.908972344	6.23E-06
Il10	3.744558999	NA	3.760946232	2.50E-04
Ccl7	1.9946451	NA	2.134669499	5.42E-04
Il3	3.005050872	NA	2.128749615	0.01137995
Cxcl13	-3.925387475	NA	1.914375578	0.01461607
Il9	NA	NA	1.060304311	0.0946694
Tnfsf18	1.995470539	NA	0.689904317	0.12933279
Lta	0.43266916	NA	0.399394732	0.34773138
Il17a	3.017243992	NA	0.516634099	0.35952186
Ppbp	-0.999434694	NA	0.525603681	0.36106858
Ifnk	-2.914627133	NA	0.271555865	0.6489383
Ccl8	3.577923423	NA	0.213370137	0.72741027
Il2	-1.462829531	NA	-0.155437738	0.80754677
Il1f8	-0.999459034	NA	-0.143198918	0.82083177
Il19	1.413787845	NA	0.087354162	0.88022032
Xcl1	-0.999465271	NA	0.595590185	NA
Ifnl3	-0.999463583	NA	0.536203479	NA
Tnfsf4	2.409552327	NA	0.466963899	NA
Il1f6	-0.999445714	NA	0.363053685	NA
Iltifb	-0.999445714	NA	0.330277203	NA
Il20	-0.999468346	NA	0.316010031	NA
Ifna9	-0.999436169	NA	0.253617623	NA
Ifna15	NA	NA	0.234379023	NA
Ifna1	NA	NA	0.134287192	NA
Cxcl17	NA	NA	0.123066252	NA
Ifng	NA	NA	0.091372743	NA

Table A2. cont.

gene name	stage 2 log2foldchange	stage 2 padj	etp log2FoldChange	etp padj
Ifna11	NA	NA	0.062003897	NA
Ifnl2	NA	NA	0	NA
Ifna4	NA	NA	0	NA
Gm21541	NA	NA	0	NA
Ifna5	NA	NA	0	NA
Ccl27b	NA	NA	0	NA
Ifna7	NA	NA	0	NA
Ifna6	NA	NA	0	NA
Ccl21b	-0.840275774	NA	0	NA
Ifna12	2.730805089	NA	-0.22044632	NA

significantly upregulated in Stage 2 neurons
significantly downregulated in Stage 2 neurons

significantly upregulated in ETP-treated neurons
significantly downregulated in ETP-treated neur

Table A3. Demographic information for ADRC brain samples.

ADRC #	Clinical Diagnosis	SEX	PMI	AGE	Braak	Demented?
2018	Control	F	24	92	II	No
2068	Control	F	9	79	II	No
2088	Control	M	24	65	I	No
2136	AD	F	24	87	VI	Yes
2166	AD	F	21	71	VI	Yes
2151	AD	M	23	81	VI	Yes

Clinical Diagnosis = Diagnosis at time of death based on Clinician and Pathology fellow's knowledge
SEX F = Female, M = Male
PMI = Post mortem interval (in hours)
AGE = Age at death (in hours)
Braak = Braak stage

Table A4. Demographic information for ROSMAP brain samples.

ID	apoe_genotype	cogdx	age_death	educ	msex	braaksc	fixation_interval	pmi	amyloid	plaq_d	plaq_n	nft	tangles
21159840	44	4	82.71	16	0	5	NA	2.17	7.37	2.35	2.12	2.33	29.17
20112377	34	4	74.77	16	0	5	19.05	5.08	8.07	0.47	4.23	3.60	61.016
10222853	34	4	85.78	20	1	5	8.23	4.5	6.38	0.90	2.35	1.88	31.03
10248033	44	4	88.47	19	1	3	57.89	17.92	3.54	2.08	0.44	0.40	2.31

apoe_genotype = Apolipoprotein E genotype
cogdx = Final consensus cognitive diagnosis
educ = Years of education
msex1=Male, 0=Female
braaksc = Braak stage fixation_interval (in hours)
PMI = Post-mortem interval (in hours)
Amyloid = Overall amyloid level - Mean of 8 brain regions
plaq_d = Diffuse plaque burden (Diffuse plaque summary based on 5 regions)
plaq_n = Neuritic plaque burden (Neuritic plaque summary based on 5 regions)
nft = Neurofibrillary tangle burden (Neurofibrillary tangle summary based on 5 regions)
tangles = Tangle density - Mean of 8 brain regions

Bibliography

1. Hoeijmakers JHJ. DNA Damage, Aging, and Cancer. N Engl J Med. 2009 Oct 8;361(15):1475–85.

2. Tubbs A, Nussenzweig A. Endogenous DNA Damage as a Source of Genomic Instability in Cancer. Cell. 2017 Feb;168(4):644–56.

3. Madabhushi R, Pan L, Tsai LH. DNA Damage and Its Links to Neurodegeneration. Neuron. 2014 Jul;83(2):266–82.

4. McKinnon PJ. Genome integrity and disease prevention in the nervous system. Genes Dev. 2017 Jun 15;31(12):1180–94.

5. Chow H man, Herrup K. Genomic integrity and the ageing brain. Nat Rev Neurosci. 2015 Nov;16(11):672–84.

6. GBD 2017 US Neurological Disorders Collaborators. Burden of Neurological Disorders Across the US From 1990-2017: A Global Burden of Disease Study. JAMA Neurol. 2021 Feb 1;78(2):165–76.

7. GBD Compare | IHME Viz Hub [Internet]. [cited 2021 Sep 23]. Available from: http://vizhub.healthdata.org/gbd-compare

8. Shanbhag NM, Evans MD, Mao W, Nana AL, Seeley WW, Adame A, et al. Early neuronal accumulation of DNA double strand breaks in Alzheimer's disease. Acta Neuropathol Commun. 2019 May 17;7(1):77.

9. Simpson JE, Ince PG, Matthews FE, Shaw PJ, Heath PR, Brayne C, et al. A neuronal DNA damage response is detected at the earliest stages of Alzheimer's neuropathology and correlates with cognitive impairment in the Medical Research Council's Cognitive Function and Ageing Study ageing brain cohort. Neuropathol Appl Neurobiol. 2015 Jun;41(4):483–96.

10. Simpson JE, Ince PG, Minett T, Matthews FE, Heath PR, Shaw PJ, et al. Neuronal DNA damage response-associated dysregulation of signalling pathways and cholesterol metabolism at the earliest stages of Alzheimer-type pathology. Neuropathol Appl Neurobiol. 2016;42(2):167–79.

11. Wu W, Hill SE, Nathan WJ, Paiano J, Callen E, Wang D, et al. Neuronal enhancers are hotspots for DNA single-strand break repair. Nature. 2021 May;593(7859):440–4.

12. Reid DA, Reed PJ, Schlachetzki JCM, Nitulescu II, Chou G, Tsui EC, et al. Incorporation of a nucleoside analog maps genome repair sites in postmitotic human neurons. Science. 2021 Apr 2;372(6537):91–4.

13. Wei PC, Chang AN, Kao J, Du Z, Meyers RM, Alt FW, et al. Long Neural Genes Harbor Recurrent DNA Break Clusters in Neural Stem/Progenitor Cells. Cell. 2016 Feb 11;164(4):644–55.

14. Rodin RE, Dou Y, Kwon M, Sherman MA, D'Gama AM, Doan RN, et al. The landscape of somatic mutation in cerebral cortex of autistic and neurotypical individuals revealed by ultra-deep whole-genome sequencing. Nat Neurosci. 2021 Feb;24(2):176–85.

15. Lodato MA, Woodworth MB, Lee S, Evrony GD, Mehta BK, Karger A, et al. Somatic mutation in single human neurons tracks developmental and transcriptional history. Science. 2015 Oct 2;350(6256):94–8.

16. McConnell MJ, Moran JV, Abyzov A, Akbarian S, Bae T, Cortes-Ciriano I, et al. Intersection of diverse neuronal genomes and neuropsychiatric disease: The Brain Somatic Mosaicism Network. Science. 2017 Apr 28;356(6336):eaal1641.

17. Lodato MA, Rodin RE, Bohrson CL, Coulter ME, Barton AR, Kwon M, et al. Aging and neurodegeneration are associated with increased mutations in single human neurons. Science. 2018 Feb 2;359(6375):555–9.

18. Musi N, Valentine JM, Sickora KR, Baeuerle E, Thompson CS, Shen Q, et al. Tau protein aggregation is associated with cellular senescence in the brain: XXXX. Aging Cell. 2018 Dec;17(6):e12840.

19. Bussian TJ, Aziz A, Meyer CF, Swenson BL, van Deursen JM, Baker DJ. Clearance of senescent glial cells prevents tau-dependent pathology and cognitive decline. Nature. 2018 Oct;562(7728):578–82.

20. Gillispie GJ, Sah E, Krishnamurthy S, Ahmidouch MY, Zhang B, Orr ME. Evidence of the Cellular Senescence Stress Response in Mitotically Active Brain Cells-Implications for Cancer and Neurodegeneration. Life Basel Switz. 2021 Feb 17;11(2):153.

21. Zhang P, Kishimoto Y, Grammatikakis I, Gottimukkala K, Cutler RG, Zhang S, et al. Senolytic therapy alleviates Aβ-associated oligodendrocyte progenitor cell senescence and cognitive deficits in an Alzheimer's disease model. Nat Neurosci. 2019 May;22(5):719–28.

22. Chow HM, Shi M, Cheng A, Gao Y, Chen G, Song X, et al. Age-related hyperinsulinemia leads to insulin resistance in neurons and cell-cycle-induced senescence. Nat Neurosci. 2019 Nov;22(11):1806–19.

23. Lindahl T, Barnes DE. Repair of Endogenous DNA Damage. Cold Spring Harb Symp Quant Biol. 2000 Jan 1;65:127–34.

24. Nakamura J, Swenberg JA. Endogenous Apurinic/Apyrimidinic Sites in Genomic DNA of Mammalian Tissues. Cancer Res. 1999 Jun 1;59(11):2522–6.

25. Attwell D, Laughlin SB. An Energy Budget for Signaling in the Grey Matter of the Brain. J Cereb Blood Flow Metab. 2001 Oct 1;21(10):1133–45.

26. El-Khamisy SF, Saifi GM, Weinfeld M, Johansson F, Helleday T, Lupski JR, et al. Defective DNA single-strand break repair in spinocerebellar ataxia with axonal neuropathy-1. Nature. 2005 Mar;434(7029):108–13.

27. Daroui P, Desai SD, Li TK, Liu AA, Liu LF. Hydrogen Peroxide Induces Topoisomerase I-mediated DNA Damage and Cell Death *. J Biol Chem. 2004 Apr 9;279(15):14587–94.

28. Takashima H, Boerkoel CF, John J, Saifi GM, Salih MAM, Armstrong D, et al. Mutation of TDP1, encoding a topoisomerase I–dependent DNA damage repair enzyme, in spinocerebellar ataxia with axonal neuropathy. Nat Genet. 2002 Oct;32(2):267–72.

29. Huang LC, Clarkin KC, Wahl GM. Sensitivity and selectivity of the DNA damage sensor responsible for activating p53-dependent G1 arrest. Proc Natl Acad Sci. 1996 May 14;93(10):4827–32.

30. Alt FW, Schwer B. DNA double-strand breaks as drivers of neural genomic change, function, and disease. DNA Repair. 2018 Nov 1;71:158–63.

31. Madabhushi R, Gao F, Pfenning AR, Pan L, Yamakawa S, Seo J, et al. Activity-Induced DNA Breaks Govern the Expression of Neuronal Early-Response Genes. Cell. 2015 Jun 18;161(7):1592–605.

32. Suberbielle E, Sanchez PE, Kravitz AV, Wang X, Ho K, Eilertson K, et al. Physiologic brain activity causes DNA double-strand breaks in neurons, with exacerbation by amyloid-β. Nat Neurosci. 2013 May;16(5):613–21.

33. Cannan WJ, Pederson DS. Mechanisms and Consequences of Double-strand DNA Break Formation in Chromatin. J Cell Physiol. 2016 Jan;231(1):3–14.

34. Zagnoli-Vieira G, Bruni F, Thompson K, He L, Walker S, de Brouwer APM, et al. Confirming TDP2 mutation in spinocerebellar ataxia autosomal recessive 23 (SCAR23). Neurol Genet. 2018 Aug 1;4(4):e262.

35. Gómez-Herreros F, Schuurs-Hoeijmakers JHM, McCormack M, Greally MT, Rulten S, Romero-Granados R, et al. TDP2 protects transcription from abortive topoisomerase activity and is required for normal neural function. Nat Genet. 2014 May;46(5):516–21.

36. Errichiello E, Zagnoli-Vieira G, Rizzi R, Garavelli L, Caldecott KW, Zuffardi O. Characterization of a novel loss-of-function variant in TDP2 in two adult patients with spinocerebellar ataxia autosomal recessive 23 (SCAR23). J Hum Genet. 2020 Dec;65(12):1135–41.

37. Stott RT, Kritsky O, Tsai LH. Profiling DNA break sites and transcriptional changes in response to contextual fear learning. PLOS ONE. 2021 Jul 1;16(7):e0249691.

38. Suberbielle E, Djukic B, Evans M, Kim DH, Taneja P, Wang X, et al. DNA repair factor BRCA1 depletion occurs in Alzheimer brains and impairs cognitive function in mice. Nat Commun. 2015 Dec;6(1):8897.

39. Rybin MJ, Ramic M, Ricciardi NR, Kapranov P, Wahlestedt C, Zeier Z. Emerging Technologies for Genome-Wide Profiling of DNA Breakage. Front Genet. 2021;11:1785.

40. Canela A, Sridharan S, Sciascia N, Tubbs A, Meltzer P, Sleckman BP, et al. DNA Breaks and End Resection Measured Genome-wide by End Sequencing. Mol Cell. 2016 Sep 1;63(5):898–911.

41. BLISS is a versatile and quantitative method for genome-wide profiling of DNA double-strand breaks | Nature Communications [Internet]. [cited 2021 Oct 15]. Available from: https://www.nature.com/articles/ncomms15058

42. Cao H, Salazar-García L, Gao F, Wahlestedt T, Wu CL, Han X, et al. Novel approach reveals genomic landscapes of single-strand DNA breaks with nucleotide resolution in human cells. Nat Commun. 2019 Dec 20;10(1):5799.

43. McConnell MJ, Lindberg MR, Brennand KJ, Piper JC, Voet T, Cowing-Zitron C, et al. Mosaic Copy Number Variation in Human Neurons. Science. 2013 Nov 1;342(6158):632–7.

44. Lodato MA, Walsh CA. Genome aging: somatic mutation in the brain links age-related decline with disease and nominates pathogenic mechanisms. Hum Mol Genet. 2019 Oct 15;28(R2):R197–206.

45. Wei PC, Lee CS, Du Z, Schwer B, Zhang Y, Kao J, et al. Three classes of recurrent DNA break clusters in brain progenitors identified by 3D proximity-based break joining assay. Proc Natl Acad Sci. 2018 Feb 20;115(8):1919–24.

46. Wang M, Wei PC, Lim CK, Gallina IS, Marshall S, Marchetto MC, et al. Increased Neural Progenitor Proliferation in a hiPSC Model of Autism Induces Replication Stress-Associated Genome Instability. Cell Stem Cell. 2020 Feb;26(2):221-233.e6.

47. Park JS, Lee J, Jung ES, Kim MH, Kim IB, Son H, et al. Brain somatic mutations observed in Alzheimer's disease associated with aging and dysregulation of tau phosphorylation. Nat Commun. 2019 Dec;10(1):3090.

48. Hoch NC, Hanzlikova H, Rulten SL, Tétreault M, Komulainen E, Ju L, et al. XRCC1 mutation is associated with PARP1 hyperactivation and cerebellar ataxia. Nature. 2017 Jan;541(7635):87–91.

49. O'Connor E, Vandrovcova J, Bugiardini E, Chelban V, Manole A, Davagnanam I, et al. Mutations in XRCC1 cause cerebellar ataxia and peripheral neuropathy. J Neurol Neurosurg Psychiatry. 2018 Nov 1;89(11):1230–2.

50. Ryan AJ, Squires S, Strutt HL, Johnson RT. Camptothecin cytotoxicity in mammalian cells is associated with the induction of persistent double strand breaks in replicating DNA. Nucleic Acids Res. 1991 Jun 25;19(12):3295–300.

51. David KK, Andrabi SA, Dawson TM, Dawson VL. Parthanatos, a messenger of death. Front Biosci-Landmark. 2009 Jan 1;14(3):1116–28.

52. Komulainen E, Badman J, Rey S, Rulten S, Ju L, Fennell K, et al. Parp1 hyperactivity couples DNA breaks to aberrant neuronal calcium signalling and lethal seizures. EMBO Rep. 2021 May 5;22(5):e51851.

53. Demin AA, Hirota K, Tsuda M, Adamowicz M, Hailstone R, Brazina J, et al. XRCC1 prevents toxic PARP1 trapping during DNA base excision repair. Mol Cell. 2021 Jul;81(14):3018-3030.e5.

54. Adamowicz M, Hailstone R, Demin AA, Komulainen E, Hanzlikova H, Brazina J, et al. XRCC1 protects transcription from toxic PARP1 activity during DNA base excision repair. Nat Cell Biol. 2021 Dec;23(12):1287–98.

55. Nouspikel T. Nucleotide excision repair and neurological diseases. DNA Repair. 2008 Jul 1;7(7):1155–67.

56. Diderich K, Alanazi M, Hoeijmakers JHJ. Premature aging and cancer in nucleotide excision repair-disorders. DNA Repair. 2011 Jul 15;10(7):772–80.

57. Nouspikel T, Hanawalt PC. Terminally Differentiated Human Neurons Repair Transcribed Genes but Display Attenuated Global DNA Repair and Modulation of Repair Gene Expression. Mol Cell Biol [Internet]. 2000 Mar 1 [cited 2022 Feb 15]; Available from: https://journals.asm.org/doi/abs/10.1128/MCB.20.5.1562-1570.2000

58. McKinnon PJ. ATM and the Molecular Pathogenesis of Ataxia Telangiectasia. Annu Rev Pathol Mech Dis. 2012 Feb 28;7(1):303–21.

59. Kuljis RO, Xu Y, Aguila MC, Baltimore D. Degeneration of neurons, synapses, and neuropil and glial activation in a murine Atm knockout model of ataxia–telangiectasia. Proc Natl Acad Sci. 1997 Nov 11;94(23):12688–93.

60. Barlow C, Hirotsune S, Paylor R, Liyanage M, Eckhaus M, Collins F, et al. Atm-Deficient Mice: A Paradigm of Ataxia Telangiectasia. Cell. 1996 Jul 12;86(1):159–71.

61. Barlow C, Ribaut-Barassin C, Zwingman TA, Pope AJ, Brown KD, Owens JW, et al. ATM is a cytoplasmic protein in mouse brain required to prevent lysosomal accumulation. Proc Natl Acad Sci. 2000 Jan 18;97(2):871–6.

62. Katyal S, Lee Y, Nitiss KC, Downing SM, Li Y, Shimada M, et al. Aberrant topoisomerase-1 DNA lesions are pathogenic in neurodegenerative genome instability syndromes. Nat Neurosci. 2014 Jun;17(6):813–21.

63. Katyal S, el-Khamisy SF, Russell HR, Li Y, Ju L, Caldecott KW, et al. TDP1 facilitates chromosomal single-strand break repair in neurons and is neuroprotective in vivo. EMBO J. 2007 Nov 14;26(22):4720–31.

64. Kanner S, Goldin M, Galron R, Ben Jacob E, Bonifazi P, Barzilai A. Astrocytes restore connectivity and synchronization in dysfunctional cerebellar networks. Proc Natl Acad Sci U S A. 2018 Jul 31;115(31):8025–30.

65. Perez H, Abdallah MF, Chavira JI, Norris AS, Egeland MT, Vo KL, et al. A novel, ataxic mouse model of ataxia telangiectasia caused by a clinically relevant nonsense mutation. Sillitoe RV, Westbrook GL, Sillitoe RV, Watt AJ, editors. eLife. 2021 Nov 1;10:e64695.

66. Tal E, Alfo M, Zha S, Barzilai A, De Zeeuw CI, Ziv Y, et al. Inactive Atm abrogates DSB repair in mouse cerebellum more than does Atm loss, without causing a neurological phenotype. DNA Repair. 2018 Dec;72:10–7.

67. Kwak YD, Shaw TI, Downing SM, Tewari A, Jin H, Li Y, et al. Chromatin architecture at susceptible gene loci in cerebellar Purkinje cells characterizes DNA damage-induced neurodegeneration. Sci Adv. 2021 Dec 17;7(51):eabg6363.

68. Mecocci P, MacGarvey U, Kaufman AE, Koontz D, Shoffner JM, Wallace DC, et al. Oxidative damage to mitochondrial DNA shows marked age-dependent increases in human brain. Ann Neurol. 1993 Oct;34(4):609–16.

69. Nunomura A, Perry G, Aliev G, Hirai K, Takeda A, Balraj EK, et al. Oxidative Damage Is the Earliest Event in Alzheimer Disease. J Neuropathol Exp Neurol. 2001 Aug 1;60(8):759–67.

70. Lovell MA, Markesbery WR. Oxidative DNA damage in mild cognitive impairment and late-stage Alzheimer's disease. Nucleic Acids Res. 2007 Nov 26;35(22):7497–504.

71. Weissman L, Jo DG, Sørensen MM, de Souza-Pinto NC, Markesbery WR, Mattson MP, et al. Defective DNA base excision repair in brain from individuals with Alzheimer's disease and amnestic mild cognitive impairment. Nucleic Acids Res. 2007;35(16):5545–55.

72. Alam ZI, Jenner A, Daniel SE, Lees AJ, Cairns N, Marsden CD, et al. Oxidative DNA Damage in the Parkinsonian Brain: An Apparent Selective Increase in 8-Hydroxyguanine Levels in Substantia Nigra. J Neurochem. 1997;69(3):1196–203.

73. Browne SE, Bowling AC, Macgarvey U, Baik MJ, Berger SC, Muquit MMK, et al. Oxidative damage and metabolic dysfunction in Huntington's disease: Selective vulnerability of the basal ganglia. Ann Neurol. 1997;41(5):646–53.

74. Bogdanov M, Brown RH, Matson W, Smart R, Hayden D, O'Donnell H, et al. Increased oxidative damage to DNA in ALS patients. Free Radic Biol Med. 2000 Oct 1;29(7):652–8.

75. Ferrante RJ, Browne SE, Shinobu LA, Bowling AC, Baik MJ, MacGarvey U, et al. Evidence of Increased Oxidative Damage in Both Sporadic and Familial Amyotrophic Lateral Sclerosis. J Neurochem. 1997;69(5):2064–74.

76. Xu G, Herzig M, Rotrekl V, Walter CA. Base excision repair, aging and health span. Mech Ageing Dev. 2008 Aug;129(7–8):366–82.

77. Sykora P, Misiak M, Wang Y, Ghosh S, Leandro GS, Liu D, et al. DNA polymerase β deficiency leads to neurodegeneration and exacerbates Alzheimer disease phenotypes. Nucleic Acids Res. 2015 Jan 30;43(2):943–59.

78. Pao PC, Patnaik D, Watson LA, Gao F, Pan L, Wang J, et al. HDAC1 modulates OGG1-initiated oxidative DNA damage repair in the aging brain and Alzheimer's disease. Nat Commun. 2020 May 18;11(1):2484.

79. Lu T, Pan Y, Kao SY, Li C, Kohane I, Chan J, et al. Gene regulation and DNA damage in the ageing human brain. Nature. 2004 Jun;429(6994):883–91.

80. Moore SPG, Kruchten J, Toomire KJ, Strauss PR. Transcription Factors and DNA Repair Enzymes Compete for Damaged Promoter Sites*. J Biol Chem. 2016 Mar 11;291(11):5452–60.

81. Ghosh R, Mitchell DL. Effect of oxidative DNA damage in promoter elements on transcription factor binding. Nucleic Acids Res. 1999 Aug 1;27(15):3213–8.

82. Wang R, Hao W, Pan L, Boldogh I, Ba X. The roles of base excision repair enzyme OGG1 in gene expression. Cell Mol Life Sci. 2018;75(20):3741–50.

83. Xia L, Huang W, Bellani M, Seidman MM, Wu K, Fan D, et al. CHD4 Has Oncogenic Functions in Initiating and Maintaining Epigenetic Suppression of Multiple Tumor Suppressor Genes. Cancer Cell. 2017 May 8;31(5):653-668.e7.

84. Kovtun IV, Liu Y, Bjoras M, Klungland A, Wilson SH, McMurray CT. OGG1 initiates age-dependent CAG trinucleotide expansion in somatic cells. Nature. 2007 May;447(7143):447–52.

85. Bettencourt C, Hensman-Moss D, Flower M, Wiethoff S, Brice A, Goizet C, et al. DNA repair pathways underlie a common genetic mechanism modulating onset in polyglutamine diseases. Ann Neurol. 2016 Jun;79(6):983–90.

86. Pinto RM, Dragileva E, Kirby A, Lloret A, Lopez E, St Claire J, et al. Mismatch repair genes Mlh1 and Mlh3 modify CAG instability in Huntington's disease mice: genome-wide and candidate approaches. PLoS Genet. 2013 Oct;9(10):e1003930.

87. Manley K, Shirley TL, Flaherty L, Messer A. Msh2 deficiency prevents in vivo somatic instability of the CAG repeat in Huntington disease transgenic mice. Nat Genet. 1999 Dec;23(4):471–3.

88. Lee JM, Chao MJ, Harold D, Abu Elneel K, Gillis T, Holmans P, et al. A modifier of Huntington's disease onset at the MLH1 locus. Hum Mol Genet. 2017 Oct 1;26(19):3859–67.

89. Lee JM, Wheeler VC, Chao MJ, Vonsattel JPG, Pinto RM, Lucente D, et al. Identification of Genetic Factors that Modify Clinical Onset of Huntington's Disease. Cell. 2015 Jul 30;162(3):516–26.

90. Moss DJH, Pardiñas AF, Langbehn D, Lo K, Leavitt BR, Roos R, et al. Identification of genetic variants associated with Huntington's disease progression: a genome-wide association study. Lancet Neurol. 2017 Sep 1;16(9):701–11.

91. Hao W, Qi T, Pan L, Wang R, Zhu B, Aguilera-Aguirre L, et al. Effects of the stimuli-dependent enrichment of 8-oxoguanine DNA glycosylase1 on chromatinized DNA. Redox Biol. 2018 Sep;18:43–53.

92. Ding Y, Fleming AM, Burrows CJ. Sequencing the Mouse Genome for the Oxidatively Modified Base 8-Oxo-7,8-dihydroguanine by OG-Seq. J Am Chem Soc. 2017 Feb 22;139(7):2569–72.

93. Amente S, Di Palo G, Scala G, Castrignanò T, Gorini F, Cocozza S, et al. Genome-wide mapping of 8-oxo-7,8-dihydro-2'-deoxyguanosine reveals accumulation of oxidatively-generated damage at DNA replication origins within transcribed long genes of mammalian cells. Nucleic Acids Res. 2019 Jan 10;47(1):221–36.

94. Wu J, McKeague M, Sturla SJ. Nucleotide-Resolution Genome-Wide Mapping of Oxidative DNA Damage by Click-Code-Seq. J Am Chem Soc. 2018 Aug 8;140(31):9783–7.

95. Cao B, Wu X, Zhou J, Wu H, Liu L, Zhang Q, et al. Nick-seq for single-nucleotide resolution genomic maps of DNA modifications and damage. Nucleic Acids Res. 2020 Jul 9;48(12):6715–25.

96. Adamec E, Vonsattel JP, Nixon RA. DNA strand breaks in Alzheimer's disease. Brain Res. 1999 Dec;849(1–2):67–77.

97. Mullaart E, Boerrigter METI, Ravid R, Swaab DF, Vijg J. Increased levels of DNA breaks in cerebral cortex of Alzheimer's disease patients. Neurobiol Aging. 1990 May 1;11(3):169–73.

98. Thadathil N, Delotterie DF, Xiao J, Hori R, McDonald MP, Khan MM. DNA Double-Strand Break Accumulation in Alzheimer's Disease: Evidence from Experimental Models and Postmortem Human Brains. Mol Neurobiol. 2021 Jan 1;58(1):118–31.

99. McKinnon PJ. Maintaining Genome Stability in the Nervous System. Nat Neurosci. 2013 Nov;16(11):1523–9.

100. Mertens J, Herdy JR, Traxler L, Schafer ST, Schlachetzki JCM, Böhnke L, et al. Age-dependent instability of mature neuronal fate in induced neurons from Alzheimer's patients. Cell Stem Cell. 2021 Sep;28(9):1533-1548.e6.

101. Mao K, Zhang G. The role of PARP1 in neurodegenerative diseases and aging. FEBS J [Internet]. [cited 2022 Mar 3];n/a(n/a). Available from: https://onlinelibrary.wiley.com/doi/abs/10.1111/febs.15716

102. Thapa K, Khan H, Sharma U, Grewal AK, Singh TG. Poly (ADP-ribose) polymerase-1 as a promising drug target for neurodegenerative diseases. Life Sci. 2021 Feb 15;267:118975.

103. Kam TI, Mao X, Park H, Chou SC, Karuppagounder SS, Umanah GE, et al. Poly(ADP-ribose) drives pathologic α-synuclein neurodegeneration in Parkinson's disease. Science. 2018 Nov 2;362(6414):eaat8407.

104. McGurk L, Gomes E, Guo L, Mojsilovic-Petrovic J, Tran V, Kalb RG, et al. Poly(ADP-Ribose) Prevents Pathological Phase Separation of TDP-43 by Promoting Liquid Demixing and Stress Granule Localization. Mol Cell. 2018 Sep 6;71(5):703-717.e9.

105. McGurk L, Mojsilovic-Petrovic J, Van Deerlin VM, Shorter J, Kalb RG, Lee VM, et al. Nuclear poly(ADP-ribose) activity is a therapeutic target in amyotrophic lateral sclerosis. Acta Neuropathol Commun. 2018 Aug 29;6(1):84.

106. Kauppinen TM, Suh SW, Higashi Y, Berman AE, Escartin C, Won SJ, et al. Poly(ADP-ribose)polymerase-1 modulates microglial responses to amyloid β. J Neuroinflammation. 2011 Nov 3;8(1):152.

107. Wy W, L P, Sc S, Ej Q, M S, Jc J, et al. Interaction of FUS and HDAC1 regulates DNA damage response and repair in neurons. Nat Neurosci [Internet]. 2013 Oct [cited 2022 Mar 4];16(10). Available from: https://pubmed.ncbi.nlm.nih.gov/24036913/

108. Deng Q, Holler CJ, Taylor G, Hudson KF, Watkins W, Gearing M, et al. FUS is Phosphorylated by DNA-PK and Accumulates in the Cytoplasm after DNA Damage. J Neurosci. 2014 Jun 4;34(23):7802–13.

109. Gardiner M, Toth R, Vandermoere F, Morrice NA, Rouse J. Identification and characterization of FUS/TLS as a new target of ATM. Biochem J. 2008 Sep 25;415(2):297–307.

110. Wang H, Guo W, Mitra J, Hegde PM, Vandoorne T, Eckelmann BJ, et al. Mutant FUS causes DNA ligation defects to inhibit oxidative damage repair in Amyotrophic Lateral Sclerosis. Nat Commun. 2018 Sep 11;9(1):3683.

111. Naumann M, Pal A, Goswami A, Lojewski X, Japtok J, Vehlow A, et al. Impaired DNA damage response signaling by FUS-NLS mutations leads to neurodegeneration and FUS aggregate formation. Nat Commun. 2018 Jan 23;9(1):335.

112. Guerrero EN, Mitra J, Wang H, Rangaswamy S, Hegde PM, Basu P, et al. Amyotrophic lateral sclerosis-associated TDP-43 mutation Q331K prevents nuclear translocation of XRCC4-DNA ligase 4 complex and is linked to genome damage-mediated neuronal apoptosis. Hum Mol Genet. 2019 Aug 1;28(15):2459–76.

113. Mitra J, Guerrero EN, Hegde PM, Liachko NF, Wang H, Vasquez V, et al. Motor neuron disease-associated loss of nuclear TDP-43 is linked to DNA double-strand break repair defects. Proc Natl Acad Sci. 2019 Mar 5;116(10):4696–705.

114. Maiuri T, Mocle AJ, Hung CL, Xia J, van Roon-Mom WMC, Truant R. Huntingtin is a scaffolding protein in the ATM oxidative DNA damage response complex. Hum Mol Genet. 2017 Jan 15;26(2):395–406.

115. Gao R, Chakraborty A, Geater C, Pradhan S, Gordon KL, Snowden J, et al. Mutant huntingtin impairs PNKP and ATXN3, disrupting DNA repair and transcription. Orr HT, Zoghbi HY, Orr HT, McLoughlin H, editors. eLife. 2019 Apr 17;8:e42988.

116. Schaser AJ, Osterberg VR, Dent SE, Stackhouse TL, Wakeham CM, Boutros SW, et al. Alpha-synuclein is a DNA binding protein that modulates DNA repair with implications for Lewy body disorders. Sci Rep. 2019 Jul 29;9(1):10919.

117. Milanese C, Cerri S, Ulusoy A, Gornati SV, Plat A, Gabriels S, et al. Activation of the DNA damage response in vivo in synucleinopathy models of Parkinson's disease. Cell Death Dis. 2018 Jul 26;9(8):1–12.

118. Vasquez V, Mitra J, Hegde PM, Pandey A, Sengupta S, Mitra S, et al. Chromatin-Bound Oxidized α-Synuclein Causes Strand Breaks in Neuronal Genomes in in vitro Models of Parkinson's Disease. J Alzheimers Dis JAD. 2017;60(s1):S133–50.

119. Mansuroglu Z, Benhelli-Mokrani H, Marcato V, Sultan A, Violet M, Chauderlier A, et al. Loss of Tau protein affects the structure, transcription and repair of neuronal pericentromeric heterochromatin. Sci Rep. 2016 Sep 8;6(1):33047.

120. Violet M, Delattre L, Tardivel M, Sultan A, Chauderlier A, Caillierez R, et al. A major role for Tau in neuronal DNA and RNA protection in vivo under physiological and hyperthermic conditions. Front Cell Neurosci. 2014;8:84.

121. Glass CK, Saijo K, Winner B, Marchetto MC, Gage FH. Mechanisms Underlying Inflammation in Neurodegeneration. Cell. 2010 Mar;140(6):918–34.

122. Nott A, Holtman IR, Coufal NG, Schlachetzki JCM, Yu M, Hu R, et al. Brain cell type–specific enhancer–promoter interactome maps and disease - risk association. Science. 2019 Nov 29;366(6469):1134–9.

123. Heneka MT, Carson MJ, Khoury JE, Landreth GE, Brosseron F, Feinstein DL, et al. Neuroinflammation in Alzheimer's disease. Lancet Neurol. 2015 Apr 1;14(4):388–405.

124. Ogrodnik M, Evans SA, Fielder E, Victorelli S, Kruger P, Salmonowicz H, et al. Whole-body senescent cell clearance alleviates age-related brain inflammation and cognitive impairment in mice. Aging Cell. 2021 Feb;20(2):e13296.

125. d'Adda di Fagagna F. Living on a break: cellular senescence as a DNA-damage response. Nat Rev Cancer. 2008 Jul;8(7):512–22.

126. Li T, Chen ZJ. The cGAS–cGAMP–STING pathway connects DNA damage to inflammation, senescence, and cancer. J Exp Med. 2018 Apr 5;215(5):1287–99.

127. Miyamoto S. Nuclear initiated NF-κB signaling: NEMO and ATM take center stage. Cell Res. 2011 Jan;21(1):116–30.

128. Rodier F, Coppé JP, Patil CK, Hoeijmakers WAM, Muñoz DP, Raza SR, et al. Persistent DNA damage signalling triggers senescence-associated inflammatory cytokine secretion. Nat Cell Biol. 2009 Aug;11(8):973–9.

129. Coppé JP, Patil CK, Rodier F, Sun Y, Muñoz DP, Goldstein J, et al. Senescence-Associated Secretory Phenotypes Reveal Cell-Nonautonomous Functions of Oncogenic RAS and the p53 Tumor Suppressor. PLOS Biol. 2008 Dec 2;6(12):e301.

130. Brzostek-Racine S, Gordon C, Scoy SV, Reich NC. The DNA Damage Response Induces IFN. J Immunol. 2011 Nov 15;187(10):5336–45.

131. Härtlova A, Erttmann SF, Raffi FA, Schmalz AM, Resch U, Anugula S, et al. DNA Damage Primes the Type I Interferon System via the Cytosolic DNA Sensor STING to Promote Anti-Microbial Innate Immunity. Immunity. 2015 Feb 17;42(2):332–43.

132. Di Micco R, Krizhanovsky V, Baker D, d'Adda di Fagagna F. Cellular senescence in ageing: from mechanisms to therapeutic opportunities. Nat Rev Mol Cell Biol. 2021 Feb;22(2):75–95.

133. Childs BG, Durik M, Baker DJ, van Deursen JM. Cellular senescence in aging and age-related disease: from mechanisms to therapy. Nat Med. 2015 Dec;21(12):1424–35.

134. Baker DJ, Childs BG, Durik M, Wijers ME, Sieben CJ, Zhong J, et al. Naturally occurring p16Ink4a-positive cells shorten healthy lifespan. Nature. 2016 Feb;530(7589):184–9.

135. Tilstra JS, Robinson AR, Wang J, Gregg SQ, Clauson CL, Reay DP, et al. NF-κB inhibition delays DNA damage–induced senescence and aging in mice. J Clin Invest. 2012 Jul 2;122(7):2601–12.

136. Piret B, Schoonbroodt S, Piette J. The ATM protein is required for sustained activation of NF-κB following DNA damage. Oncogene. 1999 Apr;18(13):2261–71.

137. Lee SJ, Dimtchev A, Lavin MF, Dritschilo A, Jung M. A novel ionizing radiation-induced signaling pathway that activates the transcription factor NF-κB. Oncogene. 1998 Oct;17(14):1821–6.

138. Li N, Banin S, Ouyang H, Li GC, Courtois G, Shiloh Y, et al. ATM Is Required for IκB Kinase (IKK) Activation in Response to DNA Double Strand Breaks *. J Biol Chem. 2001 Mar 23;276(12):8898–903.

139. Hinz M, Stilmann M, Arslan SÇ, Khanna KK, Dittmar G, Scheidereit C. A Cytoplasmic ATM-TRAF6-cIAP1 Module Links Nuclear DNA Damage Signaling to Ubiquitin-Mediated NF-κB Activation. Mol Cell. 2010 Oct 8;40(1):63–74.

140. Wu ZH, Wong ET, Shi Y, Niu J, Chen Z, Miyamoto S, et al. ATM and NEMO-dependent ELKS ubiquitination coordinates TAK1-mediated IKK activation in response to genotoxic stress. Mol Cell. 2010 Oct 8;40(1):75–86.

141. Karin M, Lin A. NF-κB at the crossroads of life and death. Nat Immunol. 2002 Mar;3(3):221–7.

142. Dou Z, Ghosh K, Vizioli MG, Zhu J, Sen P, Wangensteen KJ, et al. Cytoplasmic chromatin triggers inflammation in senescence and cancer. Nature. 2017 Oct;550(7676):402–6.

143. Erdal E, Haider S, Rehwinkel J, Harris AL, McHugh PJ. A prosurvival DNA damage-induced cytoplasmic interferon response is mediated by end resection factors and is limited by Trex1. Genes Dev. 2017 Feb 15;31(4):353–69.

144. Yang H, Wang H, Ren J, Chen Q, Chen ZJ. cGAS is essential for cellular senescence. Proc Natl Acad Sci. 2017 Jun 6;114(23):E4612–20.

145. Glück S, Guey B, Gulen MF, Wolter K, Kang TW, Schmacke NA, et al. Innate immune sensing of cytosolic chromatin fragments through cGAS promotes senescence. Nat Cell Biol. 2017 Sep;19(9):1061–70.

146. Harding SM, Benci JL, Irianto J, Discher DE, Minn AJ, Greenberg RA. Mitotic progression following DNA damage enables pattern recognition within micronuclei. Nature. 2017 Aug;548(7668):466–70.

147. Mackenzie KJ, Carroll P, Martin CA, Murina O, Fluteau A, Simpson DJ, et al. cGAS surveillance of micronuclei links genome instability to innate immunity. Nature. 2017 Aug;548(7668):461–5.

148. Ahn J, Gutman D, Saijo S, Barber GN. STING manifests self DNA-dependent inflammatory disease. Proc Natl Acad Sci. 2012 Nov 20;109(47):19386–91.

149. Gao D, Li T, Li XD, Chen X, Li QZ, Wight-Carter M, et al. Activation of cyclic GMP-AMP synthase by self-DNA causes autoimmune diseases. Proc Natl Acad Sci. 2015 Oct 20;112(42):E5699–705.

150. De Cecco M, Ito T, Petrashen AP, Elias AE, Skvir NJ, Criscione SW, et al. L1 drives IFN in senescent cells and promotes age-associated inflammation. Nature. 2019 Feb;566(7742):73–8.

151. Luna-Sánchez M, Bianchi P, Quintana A. Mitochondria-Induced Immune Response as a Trigger for Neurodegeneration: A Pathogen from Within. Int J Mol Sci. 2021 Aug 7;22(16):8523.

152. Lin M miao, Liu N, Qin Z hong, Wang Y. Mitochondrial-derived damage-associated molecular patterns amplify neuroinflammation in neurodegenerative diseases. Acta Pharmacol Sin [Internet]. 2022 Mar 1 [cited 2022 Mar 5]; Available from: https://www.nature.com/articles/s41401-022-00879-6

153. Dunphy G, Flannery SM, Almine JF, Connolly DJ, Paulus C, Jønsson KL, et al. Non-canonical Activation of the DNA Sensing Adaptor STING by ATM and IFI16 Mediates NF-κB Signaling after Nuclear DNA Damage. Mol Cell. 2018 Sep 6;71(5):745-760.e5.

154. Abe T, Barber GN. Cytosolic-DNA-Mediated, STING-Dependent Proinflammatory Gene Induction Necessitates Canonical NF-κB Activation through TBK1. J Virol. 2014 May;88(10):5328–41.

155. Miller KN, Victorelli SG, Salmonowicz H, Dasgupta N, Liu T, Passos JF, et al. Cytoplasmic DNA: sources, sensing, and role in aging and disease. Cell. 2021 Oct 28;184(22):5506–26.

156. Venegas C, Kumar S, Franklin BS, Dierkes T, Brinkschulte R, Tejera D, et al. Microglia-derived ASC specks cross-seed amyloid-β in Alzheimer's disease. Nature. 2017 Dec;552(7685):355–61.

157. Ising C, Venegas C, Zhang S, Scheiblich H, Schmidt SV, Vieira-Saecker A, et al. NLRP3 inflammasome activation drives tau pathology. Nature. 2019 Nov;575(7784):669–73.

158. Halle A, Hornung V, Petzold GC, Stewart CR, Monks BG, Reinheckel T, et al. The NALP3 inflammasome is involved in the innate immune response to amyloid-β. Nat Immunol. 2008 Aug;9(8):857–65.

159. Crow YJ, Manel N. Aicardi–Goutières syndrome and the type I interferonopathies. Nat Rev Immunol. 2015 Jul;15(7):429–40.

160. Mackenzie KJ, Carroll P, Lettice L, Tarnauskaitė Ž, Reddy K, Dix F, et al. Ribonuclease H2 mutations induce a cGAS/STING-dependent innate immune response. EMBO J. 2016 Apr 15;35(8):831–44.

161. Pokatayev V, Hasin N, Chon H, Cerritelli SM, Sakhuja K, Ward JM, et al. RNase H2 catalytic core Aicardi-Goutières syndrome-related mutant invokes cGAS-STING innate immune-sensing pathway in mice. J Exp Med. 2016 Mar 7;213(3):329–36.

162. Aditi null, Downing SM, Schreiner PA, Kwak YD, Li Y, Shaw TI, et al. Genome instability independent of type I interferon signaling drives neuropathology caused by impaired ribonucleotide excision repair. Neuron. 2021 Dec 15;109(24):3962-3979.e6.

163. Chinta SJ, Woods G, Demaria M, Rane A, Zou Y, McQuade A, et al. Cellular Senescence Is Induced by the Environmental Neurotoxin Paraquat and Contributes to Neuropathology Linked to Parkinson's Disease. Cell Rep. 2018 Jan;22(4):930–40.

164. Song X, Ma F, Herrup K. Accumulation of Cytoplasmic DNA Due to ATM Deficiency Activates the Microglial Viral Response System with Neurotoxic Consequences. J Neurosci. 2019 Aug 7;39(32):6378–94.

165. Quek H, Luff J, Cheung K, Kozlov S, Gatei M, Lee CS, et al. A rat model of ataxia-telangiectasia: evidence for a neurodegenerative phenotype. Hum Mol Genet. 2017 Jan 1;26(1):109–23.

166. Song X, Aw JTM, Ma F, Cheung MF, Leung D, Herrup K. DNA Repair Inhibition Leads to Active Export of Repetitive Sequences to the Cytoplasm Triggering an Inflammatory Response. J Neurosci. 2021 Nov 10;41(45):9286–307.

167. Lai J, Kim J, Jeffries AM, Tolles A, Chittenden TW, Buckley PG, et al. Single-nucleus transcriptomic analyses reveal microglial activation underlying cerebellar degeneration in Ataxia Telangiectasia [Internet]. bioRxiv; 2021 [cited 2022 Feb 21]. p. 2021.09.09.459619. Available from: https://www.biorxiv.org/content/10.1101/2021.09.09.459619v1

168. Sah E, Krishnamurthy S, Ahmidouch MY, Gillispie GJ, Milligan C, Orr ME. The Cellular Senescence Stress Response in Post-Mitotic Brain Cells: Cell Survival at the Expense of Tissue Degeneration. Life. 2021 Mar 11;11(3):229.

169. Jurk D, Wang C, Miwa S, Maddick M, Korolchuk V, Tsolou A, et al. Postmitotic neurons develop a p21-dependent senescence-like phenotype driven by a DNA damage response. Aging Cell. 2012 Dec;11(6):996–1004.

170. Dunckley T, Beach TG, Ramsey KE, Grover A, Mastroeni D, Walker DG, et al. Gene expression correlates of neurofibrillary tangles in Alzheimer's disease. Neurobiol Aging. 2006 Oct;27(10):1359–71.

171. Moreno-Blas D, Gorostieta-Salas E, Pommer-Alba A, Muciño-Hernández G, Gerónimo-Olvera C, Maciel-Barón LA, et al. Cortical neurons develop a senescence-like phenotype promoted by dysfunctional autophagy. Aging. 2019 Aug 30;11(16):6175–98.

172. Mathur V, Burai R, Vest RT, Bonanno LN, Lehallier B, Zardeneta ME, et al. Activation of the STING-Dependent Type I Interferon Response Reduces Microglial Reactivity and Neuroinflammation. Neuron. 2017 Dec 20;96(6):1290-1302.e6.

173. Chakraborty S, Nazmi A, Dutta K, Basu A. Neurons under viral attack: Victims or warriors? Neurochem Int. 2010;56(6):727–35.

174. Klein RS, Lin E, Zhang B, Luster AD, Tollett J, Samuel MA, et al. Neuronal CXCL10 Directs CD8+ T-Cell Recruitment and Control of West Nile Virus Encephalitis. J Virol. 2005 Sep 1;79(17):11457–66.

175. Di Liberto G, Pantelyushin S, Kreutzfeldt M, Page N, Musardo S, Coras R, et al. Neurons under T Cell Attack Coordinate Phagocyte-Mediated Synaptic Stripping. Cell. 2018 Oct;175(2):458-471.e19.

176. Dutta K, Thammisetty SS, Boutej H, Bareil C, Julien JP. Mitigation of ALS Pathology by Neuron-Specific Inhibition of Nuclear Factor Kappa B Signaling. J Neurosci. 2020 Jun 24;40(26):5137–54.

177. Welikovitch LA, Carmo SD, Maglóczky Z, Malcolm JC, Lőke J, Klein WL, et al. Early intraneuronal amyloid triggers neuron-derived inflammatory signaling in APP transgenic rats and human brain. Proc Natl Acad Sci. 2020 Mar 24;117(12):6844–54.

178. Yu CH, Davidson S, Harapas CR, Hilton JB, Mlodzianoski MJ, Laohamonthonkul P, et al. TDP-43 Triggers Mitochondrial DNA Release via mPTP to Activate cGAS/STING in ALS. Cell. 2020 Oct 29;183(3):636-649.e18.

179. Sharma M, Rajendrarao S, Shahani N, Ramírez-Jarquín UN, Subramaniam S. Cyclic GMP-AMP synthase promotes the inflammatory and autophagy responses in Huntington disease. Proc Natl Acad Sci. 2020 Jul 7;117(27):15989–99.

180. O'Mahony A, Raber J, Montano M, Foehr E, Han V, Lu S ming, et al. NF-κB/Rel Regulates Inhibitory and Excitatory Neuronal Function and Synaptic Plasticity. Mol Cell Biol. 2006 Oct 1;26(19):7283–98.

181. Boersma MCH, Dresselhaus EC, Biase LMD, Mihalas AB, Bergles DE, Meffert MK. A Requirement for Nuclear Factor-κB in Developmental and Plasticity-Associated Synaptogenesis. J Neurosci. 2011 Apr 6;31(14):5414–25.

182. Fridmacher V, Kaltschmidt B, Goudeau B, Ndiaye D, Rossi FM, Pfeiffer J, et al. Forebrain-Specific Neuronal Inhibition of Nuclear Factor-κB Activity Leads to Loss of Neuroprotection. J Neurosci. 2003 Oct 15;23(28):9403–8.

183. Kaltschmidt B, Kaltschmidt C. NF-κB in the Nervous System. Cold Spring Harb Perspect Biol. 2009 Sep;1(3):a001271.

184. Welch G, Tsai L. Mechanisms of DNA damage-mediated neurotoxicity in neurodegenerative disease. EMBO Rep [Internet]. 2022 Jun 7 [cited 2022 Jun 15];23(6). Available from: https://onlinelibrary.wiley.com/doi/10.15252/embr.202154217

185. Jacobsen E, Beach T, Shen Y, Li R, Chang Y. Deficiency of the Mre11 DNA repair complex in Alzheimer's disease brains. Mol Brain Res. 2004 Sep;128(1):1–7.

186. Kim D, Frank CL, Dobbin MM, Tsunemoto RK, Tu W, Peng PL, et al. Deregulation of HDAC1 by p25/Cdk5 in Neurotoxicity. Neuron. 2008 Dec;60(5):803–17.

187. Cruz JC, Tseng HC, Goldman JA, Shih H, Tsai LH. Aberrant Cdk5 Activation by p25 Triggers Pathological Events Leading to Neurodegeneration and Neurofibrillary Tangles. Neuron. 2003 Oct;40(3):471–83.

188. Mathys H, Adaikkan C, Gao F, Young JZ, Manet E, Hemberg M, et al. Temporal Tracking of Microglia Activation in Neurodegeneration at Single-Cell Resolution. Cell Rep. 2017 Oct;21(2):366–80.

189. Cruz JC, Kim D, Moy LY, Dobbin MM, Sun X, Bronson RT, et al. p25/Cyclin-Dependent Kinase 5 Induces Production and Intraneuronal Accumulation of Amyloid beta In Vivo. J Neurosci. 2006 Oct 11;26(41):10536–41.

190. Fischer A, Sananbenesi F, Pang PT, Lu B, Tsai LH. Opposing Roles of Transient and Prolonged Expression of p25 in Synaptic Plasticity and Hippocampus-Dependent Memory. Neuron. 2005 Dec;48(5):825–38.

191. Mertens J, Herdy JR, Traxler L, Schafer ST, Schlachetzki JCM, Böhnke L, et al. Age-dependent instability of mature neuronal fate in induced neurons from Alzheimer's patients. Cell Stem Cell [Internet]. 2021 Apr 27 [cited 2021 Aug 1]; Available from: https://www.sciencedirect.com/science/article/pii/S1934590921001612

192. Yousef A, Robinson JL, Irwin DJ, Byrne MD, Kwong LK, Lee EB, et al. Neuron loss and degeneration in the progression of TDP-43 in frontotemporal lobar degeneration. Acta Neuropathol Commun. 2017 Sep 6;5(1):68.

193. Ünal-Çevik I, Kılınç M, Gürsoy-Özdemir Y, Gurer G, Dalkara T. Loss of NeuN immunoreactivity after cerebral ischemia does not indicate neuronal cell loss: a cautionary note. Brain Res. 2004 Jul;1015(1–2):169–74.

194. McPhail LT, McBride CB, McGraw J, Steeves JD, Tetzlaff W. Axotomy abolishes NeuN expression in facial but not rubrospinal neurons. Exp Neurol. 2004 Jan;185(1):182–90.

195. Wu KL, Li YQ, Tabassum A, Lu WY, Aubert I, Wong CS. Loss of Neuronal Protein Expression in Mouse Hippocampus After Irradiation. J Neuropathol Exp Neurol. 2010 Mar 1;69(3):272–80.

196. Subramanian A, Tamayo P, Mootha VK, Mukherjee S, Ebert BL, Gillette MA, et al. Gene set enrichment analysis: A knowledge-based approach for interpreting genome-wide expression profiles. Proc Natl Acad Sci. 2005 Oct 25;102(43):15545–50.

197. Gjoneska E, Pfenning AR, Mathys H, Quon G, Kundaje A, Tsai LH, et al. Conserved epigenomic signals in mice and humans reveal immune basis of Alzheimer's disease. Nature. 2015 Feb 19;518(7539):365–9.

198. Préhaud C, Mégret F, Lafage M, Lafon M. Virus Infection Switches TLR-3-Positive Human Neurons To Become Strong Producers of Beta Interferon. J Virol. 2005 Oct 15;79(20):12893–904.

199. Sokolova A, Hill MD, Rahimi F, Warden LA, Halliday GM, Shepherd CE. Monocyte Chemoattractant Protein-1 Plays a Dominant Role in the Chronic Inflammation Observed in Alzheimer's Disease. Brain Pathol. 2009 Jul;19(3):392–8.

200. Chai Q, She R, Huang Y, Fu ZF. Expression of Neuronal CXCL10 Induced by Rabies Virus Infection Initiates Infiltration of Inflammatory Cells, Production of Chemokines and Cytokines, and Enhancement of Blood-Brain Barrier Permeability. J Virol. 2014 Dec 16;89(1):870–6.

201. Xie Z, Bailey A, Kuleshov MV, Clarke DJB, Evangelista JE, Jenkins SL, et al. Gene Set Knowledge Discovery with Enrichr. Curr Protoc. 2021;1(3):e90.

202. McCool KW, Miyamoto S. DNA damage-dependent NF-κB activation: NEMO turns nuclear signaling inside out. Immunol Rev. 2012;246(1):311–26.

203. Chien Y, Scuoppo C, Wang X, Fang X, Balgley B, Bolden JE, et al. Control of the senescence-associated secretory phenotype by NF- B promotes senescence and enhances chemosensitivity. Genes Dev. 2011 Oct 15;25(20):2125–36.

204. van Leeuwen LAG, Hoozemans JJM. Physiological and pathophysiological functions of cell cycle proteins in post-mitotic neurons: implications for Alzheimer's disease. Acta Neuropathol (Berl). 2015 Apr;129(4):511–25.

205. Cao J, Spielmann M, Qiu X, Huang X, Ibrahim DM, Hill AJ, et al. The single-cell transcriptional landscape of mammalian organogenesis. Nature. 2019 Feb;566(7745):496–502.

206. Wang C, Najm R, Xu Q, Jeong D eun, Walker D, Balestra ME, et al. Gain of toxic apolipoprotein E4 effects in human iPSC-derived neurons is ameliorated by a small-molecule structure corrector. Nat Med. 2018 May;24(5):647–57.

207. Sriram G, Milling LE, Chen JK, Kong YW, Joughin BA, Abraham W, et al. The injury response to DNA damage in live tumor cells promotes antitumor immunity. Sci Signal. 14(705):eabc4764.

208. Mathys H, Davila-Velderrain J, Peng Z, Gao F, Mohammadi S, Young JZ, et al. Single-cell transcriptomic analysis of Alzheimer's disease. Nature. 2019 Jun;570(7761):332–7.

209. Variable Details | RADC [Internet]. [cited 2021 Apr 13]. Available from: https://www.radc.rush.edu/docs/var/detail.htm?category=Pathology&subcategory=Alzheimer%27s+disease&variable=gpath

210. Chan KY, Jang MJ, Yoo BB, Greenbaum A, Ravi N, Wu WL, et al. Engineered AAVs for efficient noninvasive gene delivery to the central and peripheral nervous systems. Nat Neurosci. 2017 Aug 1;20(8):1172–9.

211. Hong S, Beja-Glasser VF, Nfonoyim BM, Frouin A, Li S, Ramakrishnan S, et al. Complement and microglia mediate early synapse loss in Alzheimer mouse models. Science. 2016 May 6;352(6286):712–6.

212. Dejanovic B, Huntley MA, De Mazière A, Meilandt WJ, Wu T, Srinivasan K, et al. Changes in the Synaptic Proteome in Tauopathy and Rescue of Tau-Induced Synapse Loss by C1q Antibodies. Neuron. 2018 Dec 19;100(6):1322-1336.e7.

213. Conductier G, Blondeau N, Guyon A, Nahon JL, Rovère C. The role of monocyte chemoattractant protein MCP1/CCL2 in neuroinflammatory diseases. J Neuroimmunol. 2010 Jul 27;224(1):93–100.

214. Bradburn S, McPhee J, Bagley L, Carroll M, Slevin M, Al-Shanti N, et al. Dysregulation of C-X-C motif ligand 10 during aging and association with cognitive performance. Neurobiol Aging. 2018 Mar;63:54–64.

215. Young K, Morrison H. Quantifying Microglia Morphology from Photomicrographs of Immunohistochemistry Prepared Tissue Using ImageJ. J Vis Exp. 2018 Jun 4;(136):57648.

216. Keren-Shaul H, Spinrad A, Weiner A, Matcovitch-Natan O, Dvir-Szternfeld R, Ulland TK, et al. A Unique Microglia Type Associated with Restricting Development of Alzheimer's Disease. Cell. 2017 Jun 15;169(7):1276-1290.e17.

217. Spangenberg EE, Lee RJ, Najafi AR, Rice RA, Elmore MRP, Blurton-Jones M, et al. Eliminating microglia in Alzheimer's mice prevents neuronal loss without modulating amyloid-β pathology. Brain. 2016 Apr 1;139(4):1265–81.

218. Song WM, Colonna M. The identity and function of microglia in neurodegeneration. Nat Immunol. 2018 Oct;19(10):1048–58.

219. Simon M, Van Meter M, Ablaeva J, Ke Z, Gonzalez RS, Taguchi T, et al. LINE1 Derepression in Aged Wild-Type and SIRT6-Deficient Mice Drives Inflammation. Cell Metab. 2019 Apr;29(4):871-885.e5.

220. Lee H, Fenster RJ, Pineda SS, Gibbs WS, Mohammadi S, Davila-Velderrain J, et al. Cell Type-Specific Transcriptomics Reveals that Mutant Huntingtin Leads to Mitochondrial RNA Release and Neuronal Innate Immune Activation. Neuron. 2020 Sep 9;107(5):891-908.e8.

221. Wyss-Coray T, Rogers J. Inflammation in Alzheimer Disease—A Brief Review of the Basic Science and Clinical Literature. Cold Spring Harb Perspect Med [Internet]. 2012 Jan [cited 2021 Apr 26];2(1). Available from: https://www.ncbi.nlm.nih.gov/pmc/articles/PMC3253025/

222. Kaltschmidt B, Ndiaye D, Korte M, Pothion S, Arbibe L, Prüllage M, et al. NF-kappaB regulates spatial memory formation and synaptic plasticity through protein kinase A/CREB signaling. Mol Cell Biol. 2006 Apr;26(8):2936–46.

223. Dimitrijevic OB, Stamatovic SM, Keep RF, Andjelkovic AV. Effects of the Chemokine CCL2 on Blood–Brain Barrier Permeability during Ischemia–Reperfusion Injury. J Cereb Blood Flow Metab. 2006 Jun 1;26(6):797–810.

224. El Khoury J, Toft M, Hickman SE, Means TK, Terada K, Geula C, et al. Ccr2 deficiency impairs microglial accumulation and accelerates progression of Alzheimer-like disease. Nat Med. 2007 Apr;13(4):432–8.

225. Naert G, Rivest S. CC Chemokine Receptor 2 Deficiency Aggravates Cognitive Impairments and Amyloid Pathology in a Transgenic Mouse Model of Alzheimer's Disease. J Neurosci. 2011 Apr 20;31(16):6208–20.

226. Yamamoto M, Horiba M, Buescher JL, Huang D, Gendelman HE, Ransohoff RM, et al. Overexpression of Monocyte Chemotactic Protein-1/CCL2 in β-Amyloid Precursor Protein Transgenic Mice Show Accelerated Diffuse β-Amyloid Deposition. Am J Pathol. 2005 May;166(5):1475–85.

227. Krauthausen M, Kummer MP, Zimmermann J, Reyes-Irisarri E, Terwel D, Bulic B, et al. CXCR3 promotes plaque formation and behavioral deficits in an Alzheimer's disease model. J Clin Invest. 2015 Jan;125(1):365–78.

228. Shanbhag NM, Rafalska-Metcalf IU, Balane-Bolivar C, Janicki SM, Greenberg RA. ATM-dependent chromatin changes silence transcription in cis to DNA double-strand breaks. Cell. 2010 Jun 11;141(6):970–81.

229. Iannelli F, Galbiati A, Capozzo I, Nguyen Q, Magnuson B, Michelini F, et al. A damaged genome's transcriptional landscape through multilayered expression profiling around in situ-mapped DNA double-strand breaks. Nat Commun. 2017 May 31;8:15656.

230. Targa Dias Anastacio H, Matosin N, Ooi L. Neuronal hyperexcitability in Alzheimer's disease: what are the drivers behind this aberrant phenotype? Transl Psychiatry. 2022 Jun 22;12(1):1–14.